

EFFECT OF CATHODE MICROSTRUCTURE ON CATHODE POLARIZATION IN
SINTERED STRONTIUM-DOPED LANTHANUM MANGANITE/YTTRIA STABILIZED
ZIRCONIA SOLID OXIDE FUEL CELLS

By

AIJIE CHEN

A DISSERTATION PRESENTED TO THE GRADUATE SCHOOL
OF THE UNIVERSITY OF FLORIDA IN PARTIAL FULFILLMENT
OF THE REQUIREMENTS FOR THE DEGREE OF
DOCTOR OF PHILOSOPHY

UNIVERSITY OF FLORIDA

2008

© 2008 Aijie Chen

To my father, the single most influential person in my life. He has come to mean more to me than I ever thought possible. No one will ever begin to compare to him.

ACKNOWLEDGMENTS

I acknowledge the Alliance for Graduate Education and the Professoriate, the Alumni of the College of Engineering, and the Department of Energy for all financial support associated with the completion of this work. I also would like to thank my committee members, Profs. Robert DeHoff, Eric Wachsman, Mark Orazem, and Dr. Gerald Bourne, for their support.

I extend gratitude to Prof. Kevin S. Jones, my supervising committee chair, for his encouragement and support, for ongoing professional and personal discussions, and for guiding me through this challenging yet rewarding learning experience at UF. I am also very grateful to Prof. Robert T. DeHoff, who provided a great deal of insight regarding this research. Very few graduate students have the opportunity to have a committee member who truly treats them as one of their own students. I will always regret not fully exploiting the luxury of having a professor as devoted to the intellectual growth of students as he. I am also very grateful to Prof. Eric Wachsman, for providing intellectual ideas and financial support for this research. Without his help on demand, I would not have completed this work. I would like to acknowledge Dr. Gerald Bourne for his assistance in developing the TEM sample preparation technique.

Furthermore, I recognize, and am grateful to, several people in the Major Analytical Instrumentation Center (MAIC) who contributed to the success of this work. Specifically, I thank Kerry Siebein for the effective crash course in TEM analysis; Dr. Luisa Dempere for valuable advice and discussions on instrument use.

I am thankful to the members of the UF-DOE HiTEC and Software and Analysis of Advanced Materials Processing (SWAMP) groups, for providing an atmosphere of camaraderie and friendship. In particular, I would like to thank Dr. Jeremiah R. Smith for discussions on the fundamentals of impedance spectroscopy; I would also like to thank Danijel Gostovic, Diane Hickey, Sam Moore, and Nicholas Rudawski for invaluable discussions on FIB operation; Lucia

Romano, David Jaeger, and Sherry Huo for advice on writing my PhD dissertation; and Sean Bishop and Martin Van Assche for discussions on electrochemical principles.

Last but not least, I would like to acknowledge my family who has supported me in all my endeavors. I will forever be indebted to my mother for her endless support and encouragement. I would like to extend my deepest gratitude and love to my husband and best friend, Yuming Niu, for supporting me, for taking care of our son, and for brightening my life. Without his support and encouragement, I would not have completed this work.

TABLE OF CONTENTS

<u>Figure</u>	<u>page</u>
ACKNOWLEDGMENTS	4
LIST OF TABLES	9
LIST OF FIGURES	10
ABSTRACT	13
CHAPTER	
1 INTRODUCTION	15
1.1 Motivation	15
1.1.1 Importance of Solid Oxide Fuel Cells (SOFCs)	15
1.1.2 Open Questions	15
1.2 Literature Review	17
1.2.1 Fundamentals of SOFCs	17
1.2.2 Cathode Polarization	19
1.2.4 Lanthanum Strontium Manganite/Yttria Stabilized Zirconia Materials Property	27
1.2.4.1 Lanthanum strontium manganite (LSM)	27
1.2.4.2 Yttria stabilized zirconia (YSZ)	29
1.2.4.3 Chemical reactivity with the YSZ	30
1.2.4.4 SOFCs processing	31
1.2.5 Microstructure Properties	32
1.2.5.1 Topological properties	32
1.2.5.2 Metric properties	33
1.2.5.3 Materials characterization techniques	34
1.2.6 Three-Link Paradigm	36
1.3 Hypothesis	38
1.4 Summary of Focused Topics	39
2 ANALYTICAL TECHNIQUES	45
2.1 Focused Ion Beam/ Scanning Electron Microscopy (FIB/SEM)	45
2.2 Stereology	48
2.2.1 Classical Quantitative Stereology	48
2.2.2 New Quantitative Stereology	52
2.2.2.1 Serial-section probe	52
2.2.2.2 Disector probe	54
2.3 Transmission Electron Microscopy (TEM)	54
2.4 Electrochemical Impedance Spectroscopy (EIS)	57
2.4.1 Fundamentals of EIS	57
2.4.2 Error Analysis of EIS	59

3	FIB/SEM TECHNIQUE DEVELOPMENT	64
3.1	Metric Property Analysis of the Composite Electrode	64
3.1.1	Introduction to the Composite Cathode	64
3.1.2	Quantification of V_v, S_v and Pore Size	65
3.1.3	Experimental Design	65
3.1.4	Results and Discussions	67
3.1.5	Conclusions	68
3.2	Interfacial Analysis of the Lanthanum Calcium Manganite (LCM)/YSZ Composite Electrode	68
3.2.1	Objective	68
3.2.2	Experimental Design	68
3.2.3	Results and Discussions	70
3.2.4	Conclusions	71
3.3	Homogeneity Analysis	71
3.3.1	Objective	71
3.3.2	Disector Analysis	72
3.3.3	Experimental Design	73
3.3.4	Results and Discussions	74
3.3.5	Conclusions	76
4	ISOCHRONAL SINTERING STUDY	87
4.1	Effect of Metric Properties on Activation Polarization	87
4.1.1	Literature Review	87
4.1.2	Quantification of L_{TPB} and S_v	88
4.1.3	Experimental Design	89
4.1.4	Results and Discussions	90
4.1.4.1	Effect of sintering on the cathode microstructure	90
4.1.4.2	Effect of metric properties on the reaction impedance	90
4.1.5	Conclusions	93
4.2	Tertiary Phase Formation Mechanism	94
4.2.1	Literature Review	94
4.2.1.1	Lanthanum zirconate (LZO) formation mechanism	95
4.2.1.2	Open questions	97
4.2.2	Experimental Design	97
4.2.3	Results	98
4.2.3.1	LZO composition profile	98
4.2.3.2	Epitaxial relationships	99
4.2.3.3	Kinetics of the tertiary phase formation	101
4.2.4	Discussion	101
4.2.4.1	Tertiary phase formation mechanism	101
4.2.4.2	Delay of the tertiary phase formation	103
4.2.4.3	Change in the interfacial resistance	104
4.2.5	Conclusions	106

5	ISOTHERMAL SINTERING STUDY	115
5.1	Effect of Metric Properties on Activation Polarization.....	115
5.1.1	Literature Review.....	115
5.1.2	Experimental Design.....	118
5.1.3	Results and Discussion.....	119
5.1.4	Conclusions.....	125
5.2	Tertiary Phase Growth Kinetics.....	127
5.2.1	Literature Review.....	127
5.2.2	Experimental Design.....	131
5.2.3	Results and Discussion.....	132
5.2.3.1	Epitaxial relationship.....	132
5.2.3.2	LZO growth kinetics.....	133
5.2.3.3	Contributions of LZO formation to activation polarization	134
5.2.3.4	Effect of LZO phase formation on ohmic polarization	138
5.2.4	Conclusions.....	141
5.3	Effect of the Topology Properties on Concentration Polarization.....	142
5.3.1	Literature Review.....	142
5.3.1.1	Skeletonization model	143
5.3.1.2	Pore-network models.....	144
5.3.1.3	Impact of gas transport on concentration polarization	148
5.3.2	Experimental Design.....	148
5.3.3	Results and Discussion.....	150
5.3.4	Conclusions.....	155
6	SUMMARY AND FUTURE WORK.....	169
6.1	Summary.....	169
6.1.1	FIB Technique Developments.....	169
6.1.2	Dependence of the Activation Polarization on the Metric Properties.....	170
6.1.3	Tertiary Phase	173
6.1.4	Dependence of the Concentration Polarization on Topological Properties ...	175
6.2	Future Work.....	176
APPENDIX		
A	FIB MANUAL.....	180
B	ELECTROCHEMICAL PROPERTIES AND SCANNING TRANSMISSION ELECTRON MICROSCOPY-ENERGY-DISPERSIVE X-RAY SPECTROMETRY (STEM-EDS) CONCENTRATION PROFILES.....	188
C	GEOMETRIC PROPERTIES OF THE ISOTHERMAL SINTERED SAMPLES	194
LIST OF REFERENCES.....		195
BIOGRAPHICAL SKETCH.....		205

LIST OF TABLES

<u>Table</u>		<u>page</u>
3-1	Summary of porosity and pore size measurement	86
3-2	The R and d spacing of LCM and YSZ on TEM diffraction patterns	86
5-1	Calculation of the LZO ohmic polarization (resistance).....	168
C-1	Geometric properties of the isothermal sintered samples.....	194

LIST OF FIGURES

<u>Figure</u>	<u>page</u>
1-1 Projected energy consumption (1980~2030).....	42
1-2 Schematic of SOFC.....	42
1-3 I-V curve of SOFC.....	42
1-4 Perovskite structure.....	43
1-5 Fluorite structure.....	43
1-6 Three-link paradigm.....	44
2-1 FIB geometry.....	61
2-2 Sampling a curve with a line probe.....	61
2-3 The calculation of net spherical image.....	62
2-4 Interaction of a high-energy electron beam with a sample.....	62
2-5 Individual resistance measurement using a modified Voigt equivalent circuit.....	63
3-1 FIB flexible geometries.....	78
3-2 FIB/SEM cross section of cathode supported SOFC sample imaged with ion beam.....	78
3-3 Pore migration on the dense electrolyte.....	79
3-4 Pore size and porosity of the cross-section sample.....	80
3-5 Schematic of Omniprobe-made TEM cross-section sample.....	80
3-6 High magnification bright field image of LCM/YSZ and the corresponding diffraction patterns.....	81
3-7 Comparison of diffraction patterns.....	82
3-8 High resolution phase contrast image at the LCM/YSZ interface.....	83
3-9 Homogeneity test of the isothermally sintered samples.....	84
3-10 Homogeneity test within a sample.....	84
3-11 Open porosity gradient of one isothermally sintered sample.....	85

4-1	Top view of the LSM/YSZ interface.....	107
4-2	Cross-section images of the isochronal sintered samples.....	107
4-3	LZO formation by Mitterdorfer et al.	108
4-4	Metric properties of the isochronal sintered samples.	109
4-5	Dependence of the charge transfer resistance on the triple-phase-boundary length.....	109
4-6	Dependence of the dissociative adsorption resistance on pore surface area of the isochronal one hour sintered samples.....	110
4-7	LSM/YSZ interface after 1200°C one hour sintering.....	110
4-8	YSZ/LZO interface and LZO/LSM interface.	111
4-9	LSM/YSZ interface after 1100°C one hour sintering.	112
4-10	YSZ/ /LSM interface for 1100°C one hour sintering.....	113
4-11	LZO thickness of one hour sintering at different temperatures.....	114
4-12	Comparison of rate constants of the LZO formation.....	114
5-1	Three paths of oxygen reduction.....	156
5-2	Cross-section images of the isothermal sintered samples.....	157
5-3	Effect of the L_{TPB} on the activation polarization.....	159
5-4	Effect of the S_V on the activation polarization of the isothermal sintered samples.....	160
5-5	Nyquist plot of the interfacial resistance.....	160
5-6	Epitaxial relationship between the LZO and the polycrystalline YSZ.....	161
5-7	Effect of the LZO on the activation polarization.....	162
5-8	Effect of metric properties on Ohmic polarization of the isothermal sintered samples...164	
5-9	Skeleton of pore networks for the isothermal sintered samples.	165
5-10	Microstructure properties for the isothermal sintered samples.....	166
5-11	Effect of microstructure properties on concentration polarization by Kim's model.....	166
5-12	Effect of microstructure properties on concentration polarization by Koponen's model.....	167

B-1	Charge transfer resistance of the isochronal sintered samples.....	188
B-2	Dissociative adsorption resistance of the isochronal sintered samples.....	188
B-3	Nyquist plot of the isothermal sintered sample.....	189
B-4	Bode plot of the isothermal sintered sample.....	189
B-5	Interfacial resistance of the isothermal sintered samples.....	189
B-6	Charge transfer resistance of the isothermal sintered samples	190
B-7	Dissociative adsorption resistance of the isothermal sintered samples	190
B-8	STEM-EDS of 12002h.....	191
B-9	STEM-EDS of 12004h.....	191
B-10	STEM-EDS of 12008h.....	192
B-11	STEM-EDS of 120015h.....	192
B-12	STEM-EDS of 120020h.....	193

Abstract of Dissertation Presented to the Graduate School
of the University of Florida in Partial Fulfillment of the
Requirements for the Degree of Doctor of Philosophy

EFFECT OF CATHODE MICROSTRUCTURE ON CATHODE POLARIZATION IN
SINTERED STRONTIUM-DOPED LANTHANUM MANGANITE/YTTRIA STABILIZED
ZIRCONIA SOLID OXIDE FUEL CELLS

By

Aijie Chen

May 2008

Chair: Kevin S. Jones

Major: Materials Science and Engineering

Cathode polarization in strontium-doped lanthanum manganite (LSM)/ yttria stabilized zirconia (YSZ) Solid Oxide Fuel Cells (SOFCs) was compared to cathode microstructure under 1h isochronal sintering between 950 and 1400°C, and under isothermal sintering at 1200°C for 2-25h. My study investigated comprehensively the effects of two-dimensional (metric), three-dimensional (topological) microstructure properties on cathode activation, ohmic, and concentration polarizations.

In the study of the activation polarization, the developed focused ion beam/ scanning electron microscopy (FIB/SEM) serial-sectioning techniques were combined with the disector homogeneity analysis. Investigation of the topological homogeneity ensured unbiased quantification of metric properties by applying classical stereology. A new method of preparing transmission electron microscopy (TEM) cross-sectional sample of the LSM/YSZ interface using a FIB and a micromanipulator was applied to the TEM study of the initial stages of $\text{La}_2\text{Zr}_2\text{O}_7$ (LZO) formation at the A-site deficient LSM/YSZ interface. The effect of LZO formation on activation polarization was underlined with respect of previous works that attached no relevance to it. It was found that LZO phase modifies the metric properties and rapidly degrades the

activation polarization, thus makes difference in the relationship between the metric properties and the activation polarization, suggested in previous SOFC models.

During the investigation of the ohmic polarization, Ohm's law was applied to relate LZO thickness (one of the geometric factors) with high-frequency impedance (ohmic resistance). It was found that LZO phase dominated ohmic polarization by modifying geometry factors and physics of the oxygen reduction mechanism.

During analysis of the concentration polarization, a new way of quantification of the geometric tortuosity of the porous cathode was performed using an elementary skeletonization model. In conjunction with two pore-network models under different flux domains, the elementary skeletonization model was effective to study transport properties of the oxygen. It was found that the faster kinetics of the gas transport through the porous cathode, the less resistance to the gas transport, thus the smaller concentration polarization.

CHAPTER 1 INTRODUCTION

1.1 Motivation

1.1.1 Importance of Solid Oxide Fuel Cells (SOFCs)

Department of Energy projected that the primary energy use (including electricity generation losses) will increase by 31 percent over next 25 years. Figure 1-1 shows that energy consumption in the commercial sector grows much more rapidly than in other sectors [1]. The desire for high-efficient, fuel-versatile and clean energy has led to the development of Solid Oxide Fuel Cells (SOFC) programs in both stationary and mobile power generation systems. Basically, SOFC consists of cathode, anode and electrolyte, and it directly converts hydrogen and air by chemical reactions into electrical energy, heat, and water without the intermediate of thermal energy, its conversion efficiency can be up to 70% for some pressurized SOFC/gas-turbine power systems [2, 3]. In addition, SOFCs can be directly operated on a full range of practical hydrocarbon fuels such as natural gas, methanol, waste biogas, diesel, and gasoline, etc. due to its high operating temperatures and tolerance to CO [2]. Furthermore, SOFCs reduce high levels of NO_x and SO_x emission associated with traditional energy-conversion systems [2].

1.1.2 Open Questions

Because of potentials of SOFC, many people have worked on elucidating microstructure-chemical reaction-performance relationship to understand how and why SOFC performance changes with time and temperature under different sintering processes, especially for the cathode, which actually contributes to the major performance of the SOFCs. Many advances in electrochemical performance measurements and microstructure characterization have allowed a deep understanding of this important relationship. Some groups focused on how 2D metric properties of the cathode microstructure affect the chemical reaction rate at the

cathode/electrolyte interface and subsequently, change in cathode polarization (the loss in voltage on the cathode side) [4, 5]. Later, kinetics of the tertiary phases formation as a result of the chemical reaction at the cathode/electrolyte interface was further studied to explain degradation of the cathode performance at high thermal budget [6-8].

However, various conclusions on the relationship between the cathode microstructure and its performance are ascribed to the complex microstructure of the cathode and the complex chemical reaction mechanism. In addition, there is a lack of statistical quantification of the metric properties and effective sample preparation techniques for performing advanced microstructure characterization. Furthermore, few researches have been focused on the effect of the topology of the cathode microstructure on the kinetics of chemical reaction within the cathode bulk, although this critical microstructure property dominates the major performance of the cathode. An effective technique to quantify 3D internal microstructure needs to be developed. Therefore, an important remaining issue is to obtain unbiased quantification of 2D and 3D microstructure properties in order to interpret the effect of the cathode microstructure on the performance. The cathode performance is controlled by effectiveness of chemical reaction mechanisms that happen at specific geometry locations of the microstructure.

In this work, a new technique that gives rise to statistical quantification of 2D microstructure properties using FIB/SEM has been developed and applied together with the classical stereology analysis. A method of building 3D cathode microstructure and a strategy of conducting the stereology analysis as well as 3D skeletonization model have been performed for the quantification of the 3D topological features. Moreover, a sample preparation technique of the cross-section TEM has been developed using a dual-beam FIB and an in-situ Omniprobe manipulator. These experimental techniques that have been originally developed in this work

will be described in details. HRTEM-EDS characterization of the cathode/electrolyte interface will be related to growth and kinetics of the tertiary phase formation. Critical microstructure properties will be associated with cathode polarization. Understanding of how microstructure properties affect cathode polarization will engineer design and fabrication of SOFCs.

1.2 Literature Review

Because this research is focused on interpretation of the relationship between the cathode microstructure and the SOFC performance, the fundamentals of SOFCs and chemical reaction mechanism are first reviewed in this chapter. The general aspects of critical microstructure properties and the cathode performance are described. The three-link paradigm among microstructure properties, chemical reaction mechanisms, and cathode polarization are fully addressed. This three-link paradigm indicates how microstructure properties affect the effectiveness of the chemical reactions, how chemical reactions control cathode polarization, and subsequently, how microstructure properties dominate cathode polarization.

1.2.1 Fundamentals of SOFCs

The first Solid Oxide Fuel Cell (SOFC) was operated by Baur and Preis in 1937 at 1000°C [9] after Nernst discovered solid-oxide electrolytes in 1899 [10]. Since then it has been considered to be a potential candidate for environmentally friendly, fuel-flexible, and efficient energy. The environmental benefits of SOFCs fit better with the energy market trend towards combined heat and power generation than fossil power plants; mobile applications are predicted in ships, locomotives, and auxiliary power units for automobiles, trucks and recreational vehicles due to its fuel flexibility; high conversion efficiency makes SOFCs a potential candidate for the fuel cell/turbine hybrid systems compared to the conventional combustion systems. The SOFC has many advantages over conventional fuel cells due to the high operating temperature of around 1000 °C. On the other hand, high operating temperature causes a slow start-up time and

degradation of SOFCs' performance. The latter can be controlled by engineering microstructure evolution or retarding isolating phases formed by thermal reactions. In order to understand chemical reaction mechanism, general information of SOFCs is introduced.

The SOFCs mainly consists of an anode, a cathode, an electrolyte and interconnect. There are four types of SOFCs designs: sealless tubular design, segmented-cell-in-series design, monolithic design and flat-plate design. Of them, the most advanced one out of the four is based on an oxygen-ion-conducting stabilized zirconia electrolyte [3]. Figure 1-2 [11] gives a schematic of a single unit of the purely electronic conductive SOFCs: a porous electronic conductive ceramic behaves as the electrode, for example, LSM, and a dense ionic conducting ceramic behaves as the electrolyte, for instance, YSZ. Both interfaces between the cathode and the electrolyte and between the anode and the electrolyte are exposed to oxygen or hydrogen gas. Two chemical reactions occur. The oxygen gas travels through porous cathode and reacts with electrons to form oxygen ions. This oxygen reduction happens at the cathode/electrolyte interface. The oxygen ions are conducted through the electrolyte toward the electrolyte/anode interface. These ions react with hydrogen gas and produce electrons, water and heat. This reaction is hydrogen oxidation. The cathodic half-cell reaction and the anodic half-cell reaction are $2e^- + \frac{1}{2}O_2 \rightarrow O^{2-}$ and $H_2 + O^{2-} \rightarrow H_2O + 2e^-$, respectively. The produced free electrons on the anode side will travel to the cathode along the external circuit. The free electrons and oxygen gas will start the cathodic reaction for the next cycle. In this manner, the SOFC converts electrochemical energy into electrical power. The conversion efficiency is determined by these chemical reactions, whose primary limiting factor is the oxygen reduction mechanism [1]. The energy loss (polarization) on the cathode side is a major contribution to polarization loss of the whole SOFC.

1.2.2 Cathode Polarization

Polarization is overpotential or voltage loss as a function of current density in SOFCs.

Three major polarizations are: 1) ohmic polarization; 2) concentration polarization; 3) activation polarization. The I-V curve [12] in Figure 1-3 shows that cathode concentration polarization and activation polarization are dominant at high current density and low current density, respectively. At high current density, the chemical reactions are limited by the diffusion of the oxidizer or the reducer from the bulk, at low current density, the reaction process is activation-controlled.

Ohmic polarization includes voltage loss from electrolyte, electrode, and electrode/electrolyte interface. Electrolyte ohmic polarization and electrode ohmic polarization are associated with the conduction of oxygen ions through the electrolyte and the conduction of electrons through the purely electronic conductive electrode, respectively. Interfacial ohmic polarization is contributed to interruption of conduction mechanism and/or reaction mechanism at contacts between electrodes and the electrolyte. Microstructure defects including tertiary phase affect conduction mechanism and/or reaction mechanism at the electrodes and the electrolyte interfaces. For electrolyte-supported SOFC, ohmic polarization mainly results from the electrolyte. In order to decrease it, the thickness of the electrolyte is reduced and an alternative electrolyte with higher ion conductivity is selected during SOFCs fabrication. Cathode ohmic polarization can be reduced by using thin cathode layer and materials with high electronic conductivity. The physical resistance to the transport of gaseous species through the anode and cathode at a given current density is treated as an electrical voltage loss. Therefore, it is called concentration polarization. Cathode concentration polarization is the major component of the SOFC concentration polarization due to lower binary diffusivity of O_2-N_2 , $D_{O_2-N_2}$, on the cathode side than that of H_2-H_2O on the anode side and smaller partial oxygen pressure (P_{O_2}) than partial

hydrogen pressure (P_{H_2}). In order to reduce cathode concentration polarization, η_{conc}^c , the cathode limiting current density, i_{cs} , must be increased by increasing effective cathode diffusivity, $D_{c(eff)}$, and reducing cathode thickness, l_c [13]. Loss in voltage due to thermally activated reactions contributes to activation polarization. Cathode activation polarization is controlled by the slowest surface chemical reaction of the oxygen reduction. In order to decrease activation polarization, both possible rate-limiting steps of the surface reaction need to be identified. If the whole oxygen reduction mechanism including individual reaction step is understood, then cathode polarization can be reduced by adjusting kinetics of the individual reaction step under operating conditions [1-3].

1.2.3 Oxygen Reduction Mechanism

Kröger-Vink notation of the oxygen reduction is written as $\frac{1}{2}O_{2(g)} + 2e' + V_o^{\bullet\bullet} \rightarrow O_o^x$. The oxygen reduction mechanism is complicated. Several variables affect processes occurring in and on the various geometric components of the microstructure. These involve three different species: ions, electrons and gas molecules. The proposed generic steps for the oxygen reduction are as following [2]:

1. Oxygen gas transport through pores within the cathode
2. Surface adsorption of oxygen molecules on the porous electrode
3. Dissociation of adsorbed oxygen molecules (O_{ads}) on the porous electrode or dense electrolyte
4. Surface diffusion of adsorbed oxygen atom to the Triple-Phase-Boundary (TPB)
5. Charge transfer between O_{ads} and e^- at the TPB

These steps can be interpreted in terms of conservation of oxygen reactant species in serial reactions. Several assumptions include: 1) In gas transport step, oxygen gas transports through

pores within the cathode under a steady-state and constant oxygen pressure gradient. Here, oxygen pressure gradient is independent of where oxygen molecules are in contact with the LSM surface. In addition, oxygen gas transport is assumed to be the rate-controlling step in the oxygen reduction in the low current density region; 2) Oxygen being absorbed on the LSM/Pore surface area is concerned in surface adsorption step. The area of the YSZ/Pore surface is a smaller interfacial area compared to the LSM/Pore surface; 3) In dissociative adsorption step, only LSM/Pore surface is considered to be the place in which the dissociative adsorption occurs. The reason is the same as in surface adsorption step; 4) In surface diffusion step, the position of the surface diffusion is located as close as possible to the TPB; 5) In charge transfer step, charge transfer reaction is not limited by the amount of electrons.

For purely electronic conducting electrodes, interfacial chemical reactions at the TPB dominate polarization loss of the cathode [14], therefore, a description of how the kinetics of these serial steps is related to cathode polarization losses starts from the charge transfer reaction in the last charge transfer step. The amount of reactants: electrons and dissociative adsorbed oxygen, O_{ads} , affects the kinetics of the charge transfer reaction at the TPB. Based on the relationship between the exchange current and the number of electrons, in the low current density regime, the amount of active electrons involved in the charge transfer reaction, $n_{e, TPB}$ can be calculated as [15, 16]

$$n_{e,TPB} = \frac{RT}{FR_{CT}I_0} \quad [1-1]$$

Provided that charge transfer resistance R_{CT} in a unit of Ωm^2 and exchange current density I_0 in a unit of A/m^2 can be measured. R , F and T are gas constant, Faraday's constant, and temperature, respectively. Here, the number of electrons involved in the charge transfer reaction, $n_{e,TPB}$, per unit time, is another term of a rate constant of the charge transfer reaction according to

Faraday's law. On the other hand, exchange current density, I_0 , and charge transfer resistance, R_{CT} , determine energy barriers that this reaction has to overcome in order to occur at the TPB.

This relationship is defined by

$$R_{CT}I_0 = \frac{\eta_{act}^c}{A_{L_{TPB}}} \quad [1-2]$$

In the low current-density region, η_{act}^c is one component of activation polarization of the cathode (charge transfer resistance), and $A_{L_{TPB}}$ is the contact area for three phases: LSM, YSZ and gas phases. It means that the kinetics of the charge transfer reaction ($\propto n_{e,TPB}$) will be affected by the metric properties of the microstructure ($A_{L_{TPB}}$) and subsequently contributes to a component of the activation polarization.

Since surface adsorption and dissociative adsorption steps happen in a series with the charge transfer reaction, their kinetics and contributions to components of the activation polarization can be explained by the amount of active electrons in the charge transfer reaction, $n_{e,TPB}$. The minimum amount of O_{ads} at the TPB, $n_{O_{ad},TPB}$, is one half of the number of

electrons, $n_{O_{ad},TPB} = \frac{RT}{2FR_{CT}I_0}$, which is the integration of the flux of O_{ads} , J_s^O , going into the TPB sites within a fixed time along a length of the TPB, L_{TPB} . In other words, the total number of O atoms needs to be

$$n_{O_{ad},TPB} = \int_0^t \int_0^{L_{TPB}} J_s^O dL_{TPB} dt = \frac{RT}{2FR_{CT}I_0} \quad [1-3]$$

After the dissociative adsorbed oxygen, $n_{O_{ad},DA}$ is diffused along some distance, L_{DA} , either on YSZ/pore surface or LSM/pore surface. In this case, the magnitude of the L_{DA} is comparable

to L_{TPB} . Therefore, the number of the Oads diffused into TPB sites, $n_{O_{ad},TPB}$, is equal to the amount of the dissociatively adsorbed oxygen being diffused either on YSZ/pore surface or on LSM/pore surface $n_{O_{ad},DA}$, thus

$$n_{O_{ad},DA} = \int_0^t \int_0^{L_{DA}} J_s^O dL_{DA} dt = n_{O_{ad},TPB} \quad [1-4]$$

where $n_{O_{ad},DA}$ is formed by dissociation of the surface adsorption of oxygen molecules, $n_{O_2,SA}$, and is a half of amount of $n_{O_{ad},DA}$. Therefore,

$$n_{O_2,SA} = 2n_{O_{ad},DA} = \frac{RT}{FR_{CT}I_0} \quad [1-5]$$

where $n_{O_2,SA}$ is calculated by the integration of the flux of O_2 , $J_{s_{cp}}^{O_2}$, being adsorbed on a unit area of the LSM/Pore surface, S_{CP} , within a finite time, t ,

$$n_{O_2,SA} = \int_0^t \int_0^{S_{CP}} J_{s_{cp}}^{O_2} dS_{CP} dt \quad [1-6]$$

Equation 1-2 ($R_{CT}I_0 = \frac{\eta_{act}^c}{A_{L_{TPB}}}$, the relationship between the activation polarization and the exchange current density at the TPB), is related to the amount of the dissociation of the adsorbed oxygen ($n_{O_{ad},DA}$) by $I_0 \propto r_{O_{ad},DA} \propto n_{O_{ad},DA}$ (Faraday's relationship between the rate constant and the dissociation of the adsorbed oxygen, $r_{O_{ad},DA}$, to the amount of its reactant, $n_{O_{ad},DA}$). The same equation is associated with the amount of the surface adsorption of oxygen molecules ($n_{O_2,SA}$) by $I_0 \propto r_{O_2,SA} \propto n_{O_2,SA}$ (Faraday's relationship between the rate constant and the surface adsorption of O_2 , $r_{O_2,SA}$, to the amount of the surface adsorption of oxygen molecules $n_{O_2,SA}$). Both kinetics of the dissociative adsorption (in dissociative adsorption) and the kinetics of the surface adsorption

of oxygen molecules (in surface adsorption) are associated with one metric property of the microstructure (area of the LSM/Pore surface) and thus are related to one kind of the activation polarization loss (dissociative adsorption resistance). Note that flux of O₂ being adsorbed on a unit area of the YSZ/pore surface is also possible in surface adsorption and dissociative adsorption. Because gas transport in gas transport step is strongly affected by the morphology of the LSM bulk, which dominates the amount of O₂ transporting through connected pores within the LSM bulk. LSM/pore surface is emphasized for simplification.

Here $J_{s_{cp}}^{O_2} = J_{O_2,CP}^V$, $J_{O_2,CP}^V$ is the maximum flux of O₂ being supplied by forcing oxygen molecules to penetrate from outside of atmosphere to the LSM/Pore surface. Since Darcy's law states that this flux is proportional to the gradient of the phase averaged oxygen pressure

$$(\nabla P_{O_2} = \frac{P_o - P_{cp}}{l_c}) \text{ by}$$

$$J_{O_2,CP}^V = -\frac{K}{\eta} \nabla P_{O_2} \quad [1-7]$$

where ∇P_{O_2} is proportional to the difference in partial oxygen pressure between the top surface of the cathode, P_o , and the LSM/Pore interface, P_{cp} , which is close to the TPB sites. In addition, η (the averaged dynamic viscosity) and K (the averaged permeability of oxygen flux through the LSM layer) are constant. In surface adsorption step, the total number of O₂ being adsorbed on a unit area of the LSM/Pore surface, $n_{O_2,CP}$, is equal to that of O₂ penetrating into the LSM bulk under the oxygen pressure, and subsequently, is the twice the amount of O_{ad} participating in charge transfer reactions at the TPB sites.

$$n_{O_2,CP} = \int_0^t \int_0^{S_{CP}} -\frac{K}{\eta} \nabla P_{O_2} dS_{CP} dt = 2n_{O_{ad},TPB} = \frac{RT}{FR_{CT}I_0} \quad [1-8]$$

Of the interest is the permeability, K . It states the effect of the microstructure terms on the flow rate of O_2 into connected pores within the cathode bulk. The relationship between the permeability and the geometry of pores within LSM bulk (tortuosity, open porosity and pore surface area) is discussed within a simple capillary theory by Kozeny [45] and further developed by Koponen [18] (see section 5.3). According to this theory, the materials topology is closely related to the activation polarization of the cathode by

$$\int_0^t \int_0^{S_{CP}} -\frac{K}{\eta} \nabla P_{O_2} dS_{CP} dt = \frac{RTA_{LTPB}}{F\eta_{act}^c} \quad [1-9]$$

Additionally, since $J_{O_2,CP}^V$, a term of the rate of gas transport, is associated with the interfacial reaction rate in order to obey mass conservation of the oxygen, which is defined as

$$r_{n_{O_{ad},TPB}} = \frac{1}{2} \int_0^{S_{CP}} -\frac{K}{\eta} \nabla P_{O_2} dS_{CP} = \frac{RTA_{LTPB}}{2F\eta_{act}^c t} \quad [1-10]$$

It is clear that cathode activation polarization can be controlled by gas transport kinetics and material properties.

In order to describe the effect of the gas transport kinetics on the cathode polarization, Kim has established a model [13] by assuming that the binary diffusion mechanism, the only factor of the maximum flux, $J_{O_2,CP}^V$, is under a constant concentration gradient (see section 2.2). The flux $J_{O_2,CP}^V$ is related to the current density, i , by

$$J_{O_2,CP}^V = \frac{iN_A}{4F} \quad [1-11]$$

The tie between gas transport kinetics and concentration polarization is as following:

$$\eta_{conc}^c = -\frac{RT}{4F} \ln\left(1 - \frac{i}{i_{cs}}\right) \quad [1-12]$$

where the cathode limiting current density, $i_{cs} = \frac{D_{c(eff)}}{l_c} \times f(p_{O_2}^c, T, p)$ [13], is a function of oxygen partial pressure on the cathode side, $p_{O_2}^c$, operation temperatures, T, and the topology of the cathode defined by $D_{c(eff)}$ (see section 5.3). An alternative model developed by Koponen et al. assumes the viscous flow as the major contribution of the $J_{O_2,CP}^V$ [18]. This model can cooperate with the Kim's model to explain how concentration polarization is attributed to kinetics of the gas transport under a constant oxygen pressure gradient. Kim's model exhibits that the total number of O₂ being adsorbed on a unit area of the LSM/pore surface with a finite time, $J_{O_2,CP}^V$, can be related to a exchange current density, i , as a function of η_{conc}^c . In this case, geometric microstructure properties control exchange current density by introducing permeability to the gas transport flux:

$$J_{O_2,CP}^V = -\frac{K}{\eta} \nabla P_{O_2} = \frac{iN_A}{4F} \quad [1-13]$$

Additionally, the cathode limiting current density, i_{cs} can be affected by the permeability, since it is proportional to the effective binary diffusivity of an mixture gas, in this case, $D_{O_2-N_2}$ according to the Ideal gas law. It is clear that three-link tie remains among the kinetics of the gas transport, the topology of the microstructure and the concentration polarization, η_{conc}^c (gas transport resistance).

In order to reduce energy loss in the SOFC system, each component of SOFCs must meet certain requirements. From the long-term stability point of view, each component not only needs to have chemical compatibility and similar thermal expansion coefficients with other

components during cell operation and fabrication, but also, individual chemical stability, phase stability, and morphological stability in both reducing and/or oxidizing environments. From the chemical reaction point of view, the electrolyte and interconnect must be dense enough to prevent gas mixing, and the cathode and the anode must be porous enough to allow gas transport to the reaction sites instead [3]. Because this research mainly focuses on the symmetric and purely electronic conductive SOFCs, materials properties of the strontium doped lanthanum manganite cathode and the yttria stabilized zirconia electrolyte are described in details.

1.2.4 Lanthanum Strontium Manganite / Yttria Stabilized Zirconia Materials Property

LSM and YSZ are state-of-art cathode material and electrolyte material, respectively.

1.2.4.1 Lanthanum strontium manganite (LSM)

LSM meets critical requirements such as 1) high electronic conductivity to offer sufficient electrons for oxygen reduction by facilitating kinetics of electrons conduction, 2) sufficient porosity to enhance kinetics of oxygen transport to the cathode/electrolyte interface for better oxygen reduction, 3) minimum reactivity and interdiffusion between the electrolyte and the interconnections to reduce degradation of the cathode performance by retarding or avoiding isolating tertiary phase formation, 4) compatibility with other cell components and so on. These advantages of the LSM over other cathode materials are attributed to materials properties of the lanthanum manganite (LMO).

LMO is a p-type perovskite oxide with a space group of $Pm\bar{3}m$, with twelve-coordinate cations for A-site of La^{3+} , six-coordinate cations for B-site of Mn^{3+} and six-coordinate anions for C-site of O^{2-} as shown in Figure 1-4. In the unit cell, A-site (La^{3+}) and B-site cations (Mn^{3+}) occupy corners of the lattice sites and the body-center of the lattice sites, respectively. Oxygen anions are located at C-site, the face-center lattice sites. LMO shows reversible oxidation-

reduction behavior, therefore changes in the Mn valence in LMO, which contributes to intrinsic p-type conductivity, must be controlled. At high temperature, LMO experiences the oxygen nonstoichiometry depending on oxygen partial pressure and La nonstoichiometry. In order to increase electronic conductivity and reduce reactivity with the YSZ, these variations in chemical composition need to be noted.

Substituting with lower valence states of cations such as Sr or Ca in A-site will enhance electrical conductivity of the LMO by increasing the Mn⁴⁺ content [3] according to the following Kröger-Vink notation:



Sr-doped LMO is the preferred cathode material because of its high electronic conductivity in the oxidizing environment [19-21]. Electronic conductivity is affected by the concentration of Sr, partial oxygen pressure, and operating temperatures, which modifies defect chemistry in the materials. Changes in Sr level alter the electronic conductivity of LSM at different temperatures [19]. It appears that 20mol% Sr causes the maximum electronic conductivity. This dependence will vary with different sample fabrication methods, processing conditions, and measuring techniques. In addition, electronic conductivity of the LSM is strongly affected by oxygen partial pressure at different operating temperatures. It has a stronger dependence of the partial oxygen pressure at lower P_{O_2} than the critical value than high P_{O_2} . At low P_{O_2} (oxygen-deficient), mobility of the major carriers (holes) is reduced due to low concentration. The electronic conductivity is reduced by decreasing operating temperatures, and the extent of reduction in electronic conductivity is varied at different operation atmospheres.

1.2.4.2 Yttria stabilized zirconia (YSZ)

SOFCS are defined by types of the electrolyte, through which oxygen ions migrate from the air cathode side to the fuel anode side. Of those electrolyte materials such as rare-earth-doped ceria, bismuth oxide, and doped lanthanum gallates, YSZ is the most commonly used electrolyte. It meets similar criteria as the cathode except :1) high ion conductivity to increase kinetics of oxygen ion transport to the anode side; 2) negligible electronic conductivity to prevent short-circuiting of the reactive gases; 3) reasonable geometry to reduce Ohmic loss. Yttria-stabilized zirconia is formed by doping ZrO_2 with Y_2O_3 .

Zirconia has the fluorite structure with a space group of $Fm\bar{3}m$ at high temperatures, with eight-coordinate cations for A-site of Zr^{4+} and 4-coordinate anions for B-site of O^{2-} . In the unit cell as shown in Figure 1-5 the cations occupy the face-center lattice sites, while oxygen atoms are located at eight tetrahedral sites. Zirconia is not a competitive electrolyte candidate due to low ion conductivity and low phase stability under operating conditions.

Substituting Y^{3+} for the A-site of Zr^{4+} , not only increases ionic conductivity but also stability of zirconia in oxidizing and reducing atmospheres. The ionic conductivity is increased by creating a large concentration of oxygen vacancies due to charge balance as shown in the following Kröger-Vink notation:



Mobility of oxygen ion is increased and subsequently increases oxygen ion conductivity. Oxygen ion conductivity varies as dopant concentration changes. It initially is increased and then decreased at higher dopant concentration due to defect ordering or electrostatic interaction [3]. The maximum ion conductivity corresponds to the minimum amount of dopant needed to fully stabilize zirconia, which will be addressed later. For yttria, the dopant is around 10mol% [22,

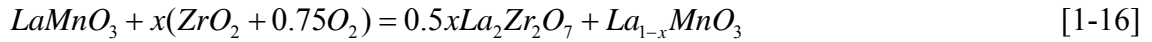
23]. Operating temperature is attributed to ion conductivity of the YSZ as well, which follows Arrhenius-type relationship. Oxygen partial pressure does not have the effect as strong on ion conductivity of YSZ as on electronic conductivity of LSM due to small change in oxygen vacancy concentration at the practical partial oxygen pressure range (0.21 atm– 10^{-25} atm) [24, 25]. If YSZ is compared to zirconia, YSZ is stabilized over a larger range of P_{O_2} . In other words, zirconia is stabilized by doping yttria. The pure zirconia has monoclinic crystal structure under the operating conditions. Zr^{4+} cations have seven coordinates of oxygen anions and one more coordinate of oxygen vacancy after doping with Y^{3+} , because the formed oxygen vacancy preferentially sits around the Zr^{4+} cations [26]. Therefore, cubic yttria-stabilized-zirconia is stable. This stability is determined by temperature and pressure conditions. Within this temperature range (room temperature to its melting point), cubic yttria-stabilized-zirconia is stable [3]. This is one of the advantages of using YSZ as the electrolyte.

1.2.4.3 Chemical reactivity with the yttria stabilized zirconia electrolyte

YSZ has good chemical compatibility with LSM, however, some interfacial reactions between YSZ and LSM still remain when the fabricating temperatures above 1200°C. Reaction products, including $La_2Zr_2O_7$ (LZO) and $SrZrO_3$, depend on composition of Sr in the LSM, the latter will be avoided with a Sr composition less than 30 mol% [27, 28]. LZO will be focused in this research due to the use of $(La_{0.8}Sr_{0.2})_{0.98}MnO_{3.8}$ as the cathode. The concern of LZO formation at the LSM/YSZ interface results from the degradation of the cathode performance, because LZO has two and a half order of magnitude lower ion conductivity than the YSZ [29-33].

Interfacial reactions can be predicted using the chemical potential diagram for the La-Mn-Zr-O system [26, 34] with different compositions of reactants. It shows that stoichiometric LMO

reacts with ZrO_2 to form the three-phase combination among ZrO_2 , $La_2Zr_2O_7$, and A-site-deficient $La_{1-x}MnO_3$ as shown in the following equation:



This equation indicates that Mn cation changes its valence state by oxidizing and has important impacts on LZO formation. Much effort has been made to study interdiffusion between LSM and YSZ in order to understand the chemical nature of the LZO formation during high-temperature treatment. It is found that manganese is the most mobile species [7], its high mobility increases the probability of LZO formation and needs to be reduced due to its effect on electrical characteristics and the structure of the cathode [3]. Furthermore, $La_{1-x}MnO_3$ does not react with YSZ showed in above equation. Many groups have investigated that the effect of A-site-deficient LSM on LZO formation and cathode performance [7, 27, 28, 35, 36]. LZO formation is minimized or retarded by decreasing the ratio of A-site to B-site in LSM cathode, thus reducing activity of La. The corresponding cathode performance is improved after a heat treatment below $1200^\circ C$ [26]. Finally, above equation indicates that LZO formed at the LSM/YSZ interface will disappear from the TPB due to the shift of the oxidizing to the reducing atmosphere [36-38].

In order to minimize interfacial reactions between the LSM cathode and the YSZ electrolyte and subsequently reduce cathode polarization, other efforts including fabrication of a composite cathode of LSM and YSZ layer at the LSM/YSZ interface [39, 40] and different dopants such as Ca and Co and low fabrication temperatures have been made.

1.2.4.4 SOFC processing

How SOFCs components are fabricated determines the microstructure properties of the electrolyte and the electrodes. Singhal summarizes different fabrication processes for three

designs of SOFCs [2]. Here, fabrication processes of the most common tubular SOFC are described. In the tubular design, thin layers of the cell components are deposited on the porous tubular support. It is formed by an extrusion of a mixture of CaO-stabilized-ZrO₂ powder, followed by sintering at 1550°C in air. The cathode, mainly doped LMO, is fabricated by depositing slurry of the doped LMO on the support tube and sintering in air at about 1400°C. The interconnect, LaCrO₃, and the electrolyte, YSZ, are made by the electrochemical vapor deposition (EVD) process. The electrolyte is deposited over the entire active area of the cell on all sides of the interconnect before the interconnect is protected by a masking material and after the interconnect is electrical contacted [3]. The last part, anode, applied by dipping the cell in nickel slurry covers the entire electrolyte surface and fixed by EVD of doped ZrO₂ in the nickel matrix, which functions as a sintering inhibitor and maintains a porous and stable anode. The procedures in fabrication step are tailored to produce sintered cathode layer having the desired properties such as microstructure properties [3] discussed in next.

1.2.5 Microstructure Properties

Microstructure parameters characterize topology of the LSM bulk and metric properties of the LSM bulk and the LSM/YSZ interface. These will be discussed in the following section.

1.2.5.1 Topological properties

To understand transport of oxygen molecules through open pores within the LSM bulk up to the LSM/YSZ interface, the topology of pore networks, including porosity V_V , tortuosity τ , and connectivity C_V have to be characterized. Furthermore, connectivity of LSM grains is helpful to study the ease of electrons conducting through the LSM bulk to the LSM/YSZ interface.

Porosity, volume fraction of open pores within the volume of the LSM bulk, is a parameter related to the amount of oxygen molecule being offered for oxygen reduction. Tortuosity of

connected pores in the LSM bulk, τ , is a key topological parameter of a pore network, which is essential in terms of transport in porous media [41], since it is related to the distance that oxygen molecules must travel within the cathode bulk. It has two physical meanings: 1) averaged flow length distribution over a given length, a weighted averaging flux in a flow field [18, 42, 43]. Tortuosity is numerically equal to the average of the relative lengths of the flow lines of all fluid elements within a fixed volume, V , passing through a given cross section, A , during a given period of time; 2) a anticosine relationship between the normal of a flow field and the flow direction. Tortuosity is the relative flow length ratio of the path that oxygen gas travels through connected pores to the thickness of the cathode. In this work, the first alternative is used for quantifying tortuosity in a porous media. Connectivity, C_V , measures how branched the structure is, or more specifically, the number of connections per unit volume or possible paths that are present between connections. Connectivity is closely related to tortuosity in terms of gas transport through the pore network. It represents possibility for the gas transport through the porous cathode. In another word, gas transport prefers to follow the less tortuous path through interconnected channels if the connectivity is high. All parameters will affect kinetics of gas transport within the LSM bulk.

1.2.5.2 Metric properties

Metric properties will affect the rest of steps after gas is filled into pore space within the LSM bulk. It consists of pore surface area, S_V (S_{CP}), the diffusion distance at the LSM/pore interface, L_{DA} , and triple-phase-boundary length, L_{TPB} .

Pore surface area, S_V , is defined as the exposed area at the LSM/Pore interface, and is associated with the amount of oxygen entering into porous cathode that can be adsorbed at the surface of the electrode. Diffusion distance along the LSM/Pore interface, L_{DA} , is closely related to how fast adsorbed oxygen arrives at the TPB site. The triple-phase-boundary length is

calculated as the perimeter of LSM electrode in contact with both gas and the YSZ electrolyte, and is a crucial microstructure parameter to characterize the LSM/YSZ interface. It affects the completeness of the charge transfer reaction and the degradation of the cathode performance [4, 28].

1.2.5.3 Materials characterization techniques

Different experimental methods have been used to measure metric properties of pore structure [44, 45]. The method of mercury injection determines open porosity, V_v , and pore surface area, S_v . The pore radii can be calculated by the Washburn equation [46]. The cumulative pore volume can be measured by forcing mercury into interconnected pores under high pressure [47]. Mercury, however, never perfectly fills all the edges and corners of the pores, and high pressure may cause damage to the pore structure. Archimedes' method measures open porosity in a safe way. In this method, the difference in weight between the dried sample and the completely saturated sample imbibed into a wetting fluid is divided by the density of the fluid. The volume of open pores is then calculated. This method also calculates the bulk volume by measuring the difference in weight between the completely saturated sample exposed to air and the saturated sample suspended in water. Compared to other measurements used to obtain open porosity, Archimedes' method will be the most accurate measurement with the proper care [47]. One limitation of this method is that it cannot calculate pore surface area and pore size. Brunauer-Emmett-Teller (BET) method can be used to measure these parameters. This technique measures pore surface area based on adsorption isotherms [48], however, BET has limited useage because sample preparation is challenging for a porous and fragile ceramic with a distribution in pore size. The optic method (combining with classical quantitative stereology) is not affected by sample preparation techniques and it quantifies areal porosity, pore size and pore surface area based on two-dimensional polished sections of the sample. Applying three

fundamental relationships in the classical stereology analysis, 3D microstructural features and two dimensional microstructural features can be simply quantified by a one dimensional line probe technique. However, this quantification technique must be applied to count open pores. More specifically, the optical images must differentiate closed pores from open pores before applying classical stereology analysis [47, 49]. Ruud et.al., (2004) and Song et.al., (2005) have calculated areal porosity [50,51] and pore size by applying classical stereology analysis based on field emission scanning auger autoprobe images [50] and SEM images [50, 51], however, they have not mentioned how to discount closed porosity which could affect the accuracy of their results.

To get accurate measurement of the TPB length, correctly applying classical quantitative stereology is as crucial as identifying open pores. Although Mizusaki et al (1991), Fukunaga et al. (1996) and Kuznecov et al. (2003) peeled off or etched away electrodes from electrolyte to expose the electrode/electrolyte interface, and they calculated normalized TPB (length of the particle multiplying by number of particles per area) as shown in SEM images [52]. Their estimations may be biased because regions of study are not random-selected.

Both quantifications of TPB length and pores need identification of open pores and require a new technique to meet the conditions of the classical stereology analysis (isotropic microstructure, uniform spacing and random orientation) (IUR) [49, 53, 54].

3D geometric properties can be obtained from a well-established method using serial-section tomography experiments [55]. It includes physical sections, optical sections and sequential sections [56-58]. One old way of making physical sections is to polish flat planes of an impregnated sample. In an impregnated sample, Wood's metal, epoxy or wax, is used to fill in interconnected pores. The first layer of the material is polished and then SEM images are taken,

then the second layer of the materials is polished and SEM images are taken and so on. Another physical sectioning approach is to use diamond knife to cut thin sections of an impregnated sample (Microtome), and use light microscopy to take the corresponding images. Both techniques offer information of the pore evolution, however, it is hard to reproduce the same spacing for each section. What's more, these techniques might cause distortion of volume of interest, therefore, these types of serial sections may not be suitable for 3D reconstruction [53]. The popular optical sectioning technique uses a confocal scanning light microscope. It avoids physical distortion of the sample due to compression. However, it is not suitable for opaque media. In addition, change in resolution increases difficulties of the 3D image processing. Since the dual beam systems-FIB/SEM has a deeper depth of field than the confocal scanning light microscope does, it is a new developed technique to fulfill collecting volume of several microns of the internal microstructure layer by layer for 3-D reconstructions [60-62, 86]. FIB tomographic experiments have been used to study 3D feature morphology of nickel base superalloys [63], fuel cells [59], ceramics [61], biological materials [64] and 3D X-ray spectral analysis of precipitates and corrosive products in metallic alloys [65].

1.2.6 Three-Link Paradigm

It is clear that fabrication processes that optimize microstructure properties can improve cathode performance by affecting kinetics of the oxygen reduction mechanism occurred on the cathode side. Since cathode ohmic polarization is a minor part of the cathode overpotential, concentration polarization and activation polarization are emphasized in this research. There are three possible rate limiting steps in series emphasized in the oxygen reduction in the purely electronic conductive cathode [66]. Each is associated with components of cathode polarization. The magnitude of the cathode polarization is determined by voltage losses due to the slowest reaction step. The first one affects concentration polarization, and is related to topology of the

microstructure (see section 1.2.5.1). The second and third contribute to activation polarization and are affected by metric properties of the cathode (see section 1.2.5.2).

The first step is gas transport through the porous cathode (Figure 1-6). It influences the limiting current density by impacting gas transport properties including effective cathode diffusivity, $D_{c(eff)}$. The cathode thickness, l_c , is fixed. The effective cathode diffusivity, $D_{c(eff)}$, is a function of the binary diffusivity of O₂-N₂, $D_{O_2-N_2}$, volume fraction of O₂ entering the cathode bulk, V_V' , tortuosity of pore channels, τ , connectivity, C_V , and the pore surface area, ($S_{CP}=S_V$). These geometric properties control the kinetics of gas transport by affecting effective diffusivity and then the exchange current density. Because the exchange current density is associated with the concentration polarization, concentration polarization can be optimized by controlling geometric properties of the cathode microstructure.

The second step is dissociative adsorption reaction (Figure 1-6). How big the area between the open pore and the cathode, S_V , and open porosity, V_V , determines the amount of oxygen molecule can be dissociated to oxygen atoms at the electrode/pore interface after oxygen molecules are adsorbed at the electrode/pore interface. V_V represents the probability of the actual amount of oxygen molecules in the reaction.

The third step is charge transfer reaction. For the purely electronic conductive cathode under normal operational situations, charge transfer reaction only happens on the triple-phase-boundary, where oxygen, cathode and electrolyte meet together. The perimeter of the electrode in contact with gas and the electrolyte, L_{TPB} , affects the number of active sites there will be for the charge transfer reaction between O_{ads} and e^- . The corresponding component of the activation polarization (charge transfer resistance and dissociative adsorption resistance) and specific

microstructure properties (L_{TPB} , V_V , and S_V) were discussed in section 1.2.6 by bridging kinetics of each serial step with the charge transfer reaction.

However, ties among them are only effective for the charge transfer reaction in an ideal case. If the microstructure changes affect gas transport and dissociative adsorption; if the tertiary phase is formed at the cathode/electrolyte interface due to high sintering temperatures; if the connection between cathode grains as well as between the cathode and the electrolyte is not complete enough, then conduction of e^- and V_O^{2-} is interrupted from the source (electrode for electrons and electrolyte for oxygen ions) to the sink (TPB sites). These conduction barriers of the reactant species cause insufficient amount of reactants for the charge transfer reaction, and L_{TPB} will not represent active sites for charge transfer between LSM and YSZ.

In summary, the concentration polarization due to gas transport resistance depends on cathode effective diffusivity, specifically, a combination of the open porosity, V_V , tortuosity, τ and pore surface area, S_V . The activation polarization consists of the dissociative adsorption resistance and the charge transfer resistance. Two resistances are associated with the energy barrier that needs to be overcome for the thermal active reactions to occur, and they are mainly affected by metric properties of the porous cathode such as pore surface area, S_V , and L_{TPB} , as shown in Figure 1-6. Cathode polarization can be influenced by a combination of changes in these geometry parameters of the cathode. Changes in these geometry properties are ascribed to kinetics of the three possible rate-limiting steps in the oxygen reduction mechanism.

1.3 Hypothesis

Under two different sintering conditions: isochronal sintering and isothermal sintering, concentration polarization (gas transport resistance) will be reduced by less tortuous path, high open porosity and fully connected pores. Additionally, dissociative adsorption resistance, one

component of the activation polarization, will be increased by small pore surface area, S_V .

Furthermore, another component of the activation polarization, charge transfer resistance, will be decreased by long L_{TPB} provided that the amount of reactants is sufficient and conduction of reactants is not inhibited. In order to analyze the impact of microstructure properties on the cathode polarization, analytical techniques are developed as followings:

1. Plane-serial sectioning techniques using FIB/SEM and 3D skeletonization model are applied to quantify topology of the pore space.
2. Cross-serial sectioning techniques using FIB/SEM and classical stereology model are used to statistically quantify metric properties of the porous cathode and the cathode/electrolyte interface.
3. Cross-section TEM sample preparation technique using FIB/SEM, an in-situ micromanipulator, and HRTEM are fulfilled to study tertiary phase formation at the cathode/electrolyte interface.

1.4 Summary of Focused Topics

As explained in the introduction, characterization of the metric and topologic properties of the cathode microstructure is an important area of study to improve the understanding of the three-link paradigm among the cathode microstructure, oxygen reduction mechanism, and the cathode polarization. This research will seek to understand this important three-link paradigm first under isochronal sintering study (one hour sintering in the temperature range between 950 and 1400°C) and then focus on degradation of the cathode performance under the isothermal sintering (1200°C in the time range between 2 and 25hrs).

After a brief description of the main characterization techniques (FIB, Stereology, and TEM-EDS) used in this work (see Chapter 2), the original experimental topic of this research consists of three parts: 1) Chapter 3 explores new applications of FIB/SEM coupled with other advanced analyses. In particular, the combination of FIB/SEM and stereology limit the disadvantages of FIB/SEM technique. Statistical quantification of the metric properties of the

Siemens-Westinghouse cathode-supported solid oxide fuel cell (SOFC) sample becomes feasible using FIB/SEM and classical stereology. The homogeneity study of the topology of the state-of-art SOFC samples is likely to combine FIB/SEM with advanced stereology. Interfacial characterization of the Siemens-Westinghouse cathode-supported SOFC sample is accomplished by using HRTEM, since a new methodology of preparing TEM cross-section sample has been developed. These new applications of the FIB/SEM are successfully applied to several materials system (see Chapter 4 and 5). 2) The impact of the metric properties of the state-of-art SOFC samples on the cathode activation polarization is described under the isochronal sintering in Chapter 4. The isochronal sintering study provides a big picture of the evolution of the microstructure as well as the electrochemical properties. The individual reaction is affected by the specific metric property thus the corresponding activation polarization is changed. The tertiary phase formation mechanism is discussed as well. The formation of the tertiary phase is affected by changing the stoichiometry of the cathode. The tertiary phase formation mechanism contributes to dramatic changes in the microstructure and electrochemical properties under the isochronal sintering condition. 3) Chapter5 focuses on a systematic study of the effects of geometric properties on the cathode polarization (concentration polarization, activation polarization and ohmic polarization). How topology of the cathode microstructure affects the concentration polarization is addressed at the two flux dominant domains. The isothermal sintering study provides the first picture of how tertiary phase formation interrupts the chemical reaction and physical conduction mechanism, thus electrochemical properties are degraded. Kinetics of the tertiary phase formation in this stoichiometry of LSM has been systematically studied for the first time. The study of the tertiary phase formation brings a new angle to the

understanding of the dependence of the cathode activation polarization and cathode ohmic polarization on the metric properties of the cathode.

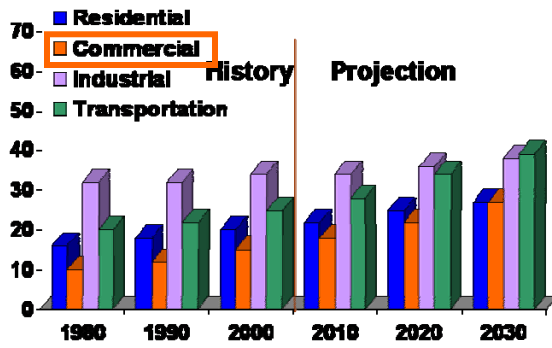


Figure 1-1. Projected energy consumption (1980~2030)[1]

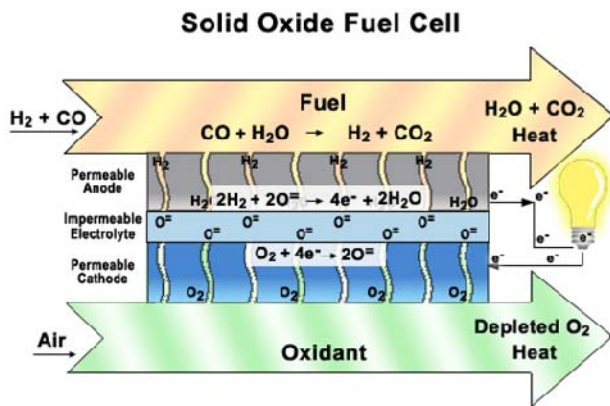


Figure 1-2. Schematic of SOFC[11]

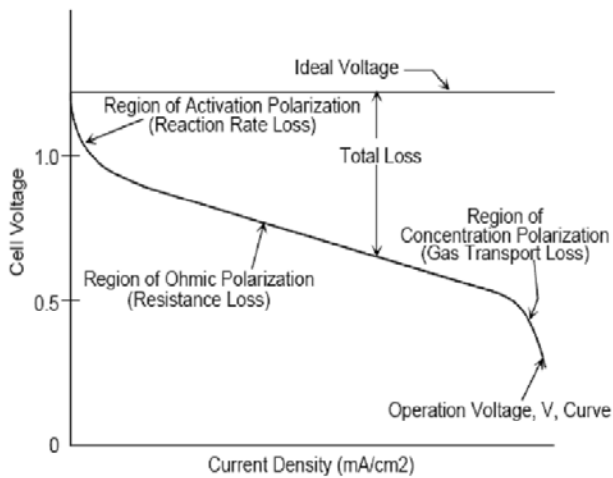


Figure 1-3. I-V curve of SOFC [12]

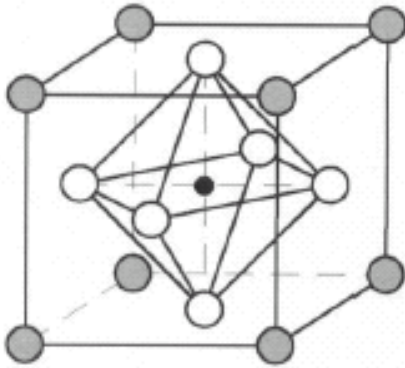


Figure 1-4. Perovskite structure: La³⁺ sits in A-site (gray circles); O²⁻ sits in C-site (white circles); Mn³⁺ sits in B-site (black circles).

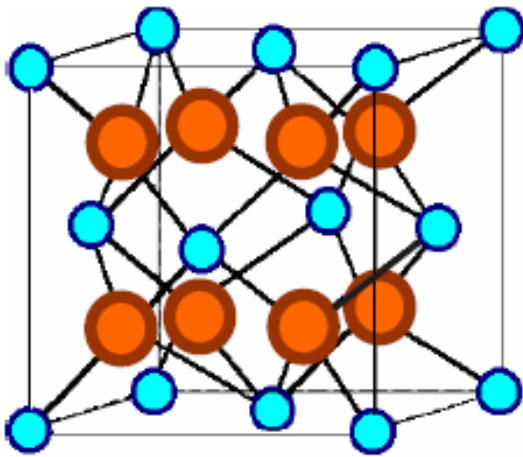


Figure 1-5. Fluorite structure: Zr⁴⁺-site in blue circles; O²⁻-site in red circles.

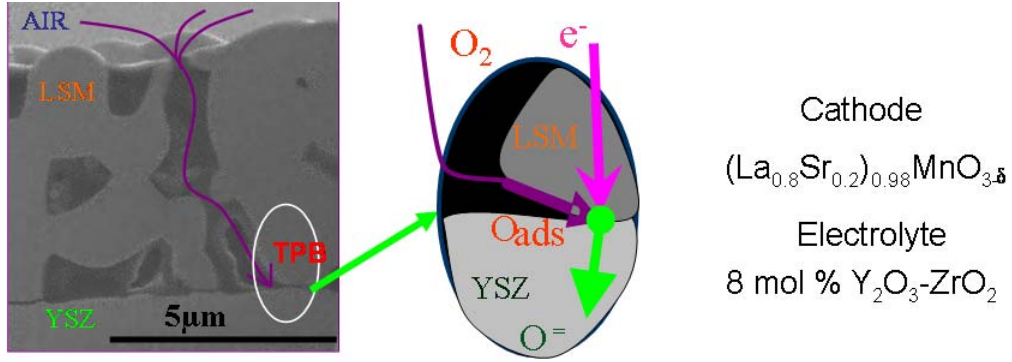


Figure 1-6. Three-link paradigm: oxygen reduction kinetics; microstructure properties (topological and metric properties); electrochemical properties (activation and concentration polarizations). Picture on the left shows that gas transports through the porous cathode, picture on the right shows occurrence of three possible rate-determining-step in details.

CHAPTER 2 ANALYTICAL TECHNIQUES

This chapter will describe four analytical methods, which have been used in this work: Focused Ion Beam/ Scanning Electron Microscopy (FIB/SEM), Stereology, Transmission Electron Microscopy (TEM) and Electrochemical Impedance Spectroscopy (EIS). The goal is to help readers better understand the results and discussions presented in the subsequent chapters.

2.1 Focused Ion Beam/ Scanning Electron Microscopy (FIB/SEM)

A dual-beam FIB/SEM system combines a focused ion beam with a scanning electron beam, E-beam. FIB has experienced an intensive period of maturation over past 20 years. It is rather a tool of preparing samples for numerous other analytical techniques than an expensive TEM sample preparation tool, which is used in the semiconductor industry. In addition, new applications of FIB are being developed for 3D materials characterization and nanotechnology, for applications in ceramics [61], metallurgy [65, 67], polymer and biology [64]. Its contribution to this work is that it allows for characterization of the metric properties of microstructure (two dimensional) and topology of microstructure (three dimensional) for porous SOFC ceramics via automated serial sectioning.

A dual-beam FIB/SEM system consists of a vacuum system, liquid metal ion source (LMIS), electron and ion-column systems, stage, computer systems and detectors. The LMIS allows for the finely focused ion beam milling with high lateral resolution. Ga⁺ is the most common liquid source due to its materials properties described in [68]. Usage of Ga⁺ leads to high resolution milling because of following reasons. Its emission characteristics enable high angular intensity with a small energy spread, and its super-cooling properties allow for formation of a “Taylor cone” shape of a point source with a 2-5nm diameter, after the tungsten tip is applied to an electrical field. Therefore, this LMIS provides an ample amount of the evaporated

ions by applying low voltage. What's more, the low energy spread of the beam yields a stable beam under low emission currents. These advantages are attractive for high-resolution electron-beam imaging. In order to achieve this, the problem of charging for low conductivity ceramic materials needs solving.

As the SEM characterizes a poorly conducting specimen, the specimen becomes electrically charged when the number of electrons received is off balance with the number of emitted electrons [68]. As a consequence, the negative charge built up on the surface of the specimen generates a negative electrical field [69, 70]. This electrical field will interfere with the collection of secondary electrons and, even worse, deflect the incident beam and damage the specimen [70-72]. In low voltage SEM, although surface potential was reduced by decreasing the number of incident electrons on the surface, a high conductivity coating should be applied on the specimen. High quality images are achieved by increasing secondary electron yield. The regular C and Au-Pd coatings will not meet these stringent requirements and may introduce image artifacts [70, 71]. In the recently developed variable pressure SEM, charge at surface is neutralized by positive ions introduced by gas. This gas, however, reduces the efficiency of collecting secondary electrons [70, 73].

In the FIB/SEM, Ga ions introduced by the scanning ion beam (SI) neutralize the negative charge on the surface or within the bulk and reduces the charging effect [70]. The electrical field between the surface and the subsurface becomes less negative than the corresponding field at normal incidence. Because the specimen is tilted with respect to the incident electron beam in the FIB/SEM, the number of electrons which are escaped from the bulk of the specimen is increased. In addition, several options of FIB operation such as low beam current, small scanned region and quick scanning rate and SI imaging will suppress charging.

The integration of the FIB/SEM system is capable of performing serial sectioning due to the relatively low damage to the sample; this is compared to mechanical serial sectioning. Both beams can operate independently, and they can be coincided at the same focused point of the specimen. The angle between the ion beam and the electron beam is 52° (Figure 2-1). In FIB/SEM, the Ga^+ scanning ion beam gradually mills material through the bulk of the interested region. The non-destructive secondary electron beam (SE) takes high quality images with the atomic resolution. Like the traditional single ion beam, channeling contrast allows to study microstructure features, which have different crystal orientations. One main advantage of the ion beam in FIB/SEM over the traditional single ion beam is that SI, reduces the damage to the sample and decreases the alteration of the crystal structure [47]. Furthermore, the cooperation of the ion beam assisted chemical vapor deposition with the gas sources system produces Pt layers, deposited on the specific sites, these layers protect the region of interest from further ion milling. Therefore, compared to physical sectioning, ion beam serial-sectioning minimizes the distortion of the interested feature [62]. In addition, shape of pore-network is not changed because ion beam current can be adjusted to control the damage extent for pores as low as possible.

Microstructure characterization of 3D requires that evolution of the microstructure feature of interest is recorded with resolution from 1 to 10 microns. Like traditional SEM, the secondary electron beam in FIB/SEM has a large depth of field. Using a small spot size increases the depth of focus in the secondary electron mode in FIB/SEM. The large depth of field gives FIB/SEM the capability of imaging deep structural formation through several microns [74, 75]. In addition, the secondary electron beam in FIB/SEM takes high resolution images with a large depth of field. Therefore, the difficulty of image processing due to the change in resolution as seen in the

confocal scanning light microscope is avoided. Furthermore, FIB has a relatively large working distance of ~2cm, it is capable of imaging topology of the sample without varying fields.

Image alignment of the serial sectioning must be performed before image processing. To properly align several microns of materials, reproducible spacing, fiduciary mark and high resolution image must be adequate [76, 77]. The ion beam slices materials with the spacing of several tens of nanometers, additionally, fiduciary marks are produced as reference points of the image alignment, and the sectioned image taken by the e-beam has a submicron scale of lateral spatial resolution [78, 62]. Therefore, the integration of electron and ion beams provides a useful tool for 3D inspection of pore structure, buried defects or metrology [79, 80], whereas, the conventional SEM is restricted to 2D surface analysis.

Position-flexibility of the FIB/SEM system permits statistic characterization of microstructure features in 2-D (metric properties) combined with stereology. Five-axis movement and automatic precise-positioning are also offered in the FIB/SEM system.

In summary, the FIB/SEM system provides focused ion-beam milling with a high lateral resolution of a few nanometers, low damage to the specific sites on the sample and large depth of field (~ ten microns). These are important criteria to quantify complete microstructure properties like pore surface area, triple-phase-boundary length, volume fraction of pores, how pores connected with each other, connectivity and how straight pore channel is, tortuosity, for porous SOFC materials.

2.2 Stereology

2.2.1 Classical Quantitative Stereology

Classical stereology provides a set of tools to quantify properties of the 3D microstructure by analyzing two-dimensional optical images. It is effective not only because it solves the problems of quantification of microstructures when information on 3D microstructure features

can not be achieved by experiment, but also because it simplifies the quantification process when the microstructure is complicated. It requires an unbiased sampling strategy, systematic sampling probe, and statistical analysis to get accurate estimates [53, 54]. It appears important when the microstructure is not uniform and not isotropic in terms of the distribution of microstructural features. Classical stereology requires three fundamental relationships for the quantification of metric properties of pores [53].

The traditional rule in stereology is that the volume fraction of a phase within the structure can be measured by the area fraction of this phase on the image, that is, volumetric porosity (V_v) can be simplified by calculating areal porosity (A_A), $V_v = A_A$ [81]. The length of lines per unit area can be measured by counting the number of intersections at the line probe and the pore solid interface per unit length (L_A). Line probes are required to be parallel to each other, uniformly distributed and randomly oriented. In this work, TPB length density (L_{TPB}) is numerically equal to L_A as discussed in the following paragraph, and can be calculated by counting number of intersections (P_L) of line probes that sweep through the interface. The surface area per unit volume can be quantified in a similar way of calculating L_{TPB} . The difference is that for the pore network in ceramics, pore surface area density (S_v) can be calculated by counting the number of intersections that line probes sweep through the spherical image. All metric properties above are estimated by two dimensional or one dimension probes [49, 82, 83]. This is one of the main attractions of classical quantitative stereology analysis.

The perimeter of the triple-phase-boundary per unit area, a two dimensional feature, can be calculated by integrating the number of intersections formed per unit length of the test line, which is randomly orientated in two dimensions. Positional probability and orientational probability are taken into account for quantification. Imagining a randomly oriented curve is

contained in a square of length L as shown in Figure 2-2, the position probability (X) of a pair of line probes shown in Figure 2-2a, parallel to y axis, intersecting the curve is numerically equal to the ratio between the projection length($dx(\theta)$) and the length (L) of the square: $\frac{dx(\theta)}{L}$. The projection length represents the distance between two intersections being projected on the x dimension. The number of intersected points by N line probes intersecting the curve is the product of N and X . In addition, the orientation probability of intersections (Y) by a pair of randomly oriented line probes is shown in Figure 2-2b. Y can be calculated by angle fraction of the curve ($d\theta/2\pi$). The total number of intersections by the randomly oriented line probe per unit length (P_L) is defined by

$$P_L = \frac{N \int_0^\lambda \int_0^{2\pi} XY}{NL} = \frac{N \int_0^\lambda \int_0^{2\pi} \frac{dx(\theta)}{L} \frac{d\theta}{2\pi}}{NL} \quad [2-1]$$

where λ is the length of the curve, $dx(\theta)$ is the projection length of a finite element component of λ ($d\lambda$), therefore, $dx(\theta) = d\lambda \cos \theta$. θ is defined as the angle between the tangent line of $d\lambda$ and the x axis, and $d\theta$ is the angle between two line probes. The right side in equation 2-1 is equal to $\frac{2}{\pi} \frac{\lambda}{L^2}$, where $\frac{\lambda}{L^2}$ is called “normalized curve length per area”. As a consequence, the normalized TPB length per area L_A is calculated by the line intersect count, P_L and is defined as [82, 83]

$$L_A = \frac{\pi}{2} P_L \quad [2-2]$$

In the case of deriving S_V , based on the previous description, the position probability for a pair of line probes (X) intersecting the surface element is the ratio of the projected area ($dA(\theta, \phi)$) to the square area (L^2).

$$X = \frac{dA(\theta, \phi)}{L^2} \quad [2-3]$$

Therefore, the projected surface area per volume can be calculated by integrating number of intersections per unit length of N test line probes (P_L) in space.

$$dP_L(\theta, \phi) = \frac{\frac{NdA(\theta, \phi)}{L^2}}{NL} = \frac{dA(\theta, \phi)}{L^3} \quad [2-4]$$

In spherical coordinates, ϕ is the angle between normal of the surface element and the line probe in y-z plane, and θ is the angle between normal of the surface element and the projection of the test line probe in x-y plane. The orientation probability (Y) of the line probe sweeping the surface element in all orientations is the enclosed area ($(d\phi \sin \phi d\theta)$ divided by the total sphere area (4π)). Taking into account all the positions and the orientations, the number of intersections with a unit of surface element by the unit length of a line probe is defined as

$$dP_L = \frac{N}{NL} \int_0^\pi \int_0^{2\pi} XY = \int_0^\pi \int_0^{2\pi} \frac{ds(\theta, \phi) \cos(\phi) \sin \phi d\phi d\theta}{L^3} \frac{1}{4\pi} = \frac{1}{2} \frac{ds}{L^3} \quad [2-5]$$

Finally,

$$P_L = \int dp_L = \iint_s \frac{ds}{2L^3} = \frac{S_v}{2} \quad [2-6]$$

where S_v is the surface area per unit volume.

The metric properties of the cathode can be quantified by the line probe technique. The probe can be randomly oriented in regular two dimensional images and can be uniformly spaced to get unbiased estimations of the TPB length and the pore surface area. The topological properties of the cathode can not be measured by one layer of regular optic images, because keeping track of the open pores changing to the closed pores, and observing one pore splitting up to several pores, require three dimensional reconstruction of the microstructure. A technique that

can take serial sections of the microstructure and can record fingerprints of the pores from the start to the end is necessary. A volume of about several microns is needed to see the internal microstructure.

2.2.2 New Quantitative Stereology

New quantitative stereology is recently developed comparing to the classical stereology.

2.2.2.1 Serial-section probe

A new stereology analysis technique, serial-section probe, is used to measure the topology of pore space. The topology of pore space affects diffusion and viscous flow of oxygen gas through the bulk of the cathode. It determines how many oxygen molecules are available at the interface [13, 84, 85]. In serial-section probe, a set of closed spaced sections sweep through the 3D structure. It surveys details of the entire feature of interest in the milled volume provided that the spacing of the two consecutive images is close enough. It allows calculation of the net spherical image (whole surface area that binds the 3D structure) Ω_{net} , which is the basic parameter for calculating connectivity of the pore space [53].

Connectivity C_v is a key topological parameter of a pore network, which is essential in terms of transport in porous media [41]. It measures how branched the structure is, or more specifically, the number of connections per unit volume or paths that are present between locations. The basic theorem of topology confirms that the connectivity C_v of a closed surface is equal to the corresponding genus G , which is the largest number of cuts that are made through parts of the shape without totally isolating any part from the rest. In this work, connectivity is calculated by relating number of the area tangent count of convex, T_{v++} , number of the area tangent count of concave, T_{v--} , and number of the area tangent count of saddles, T_{v+-} , to the Euler characteristic, $(N_v - C_v)$. C_v is the connectivity of the pore and N_v is the number of pores,

respectively. A 3-D structure can be reproduced by building a net spherical image (the area of the unit sphere element in 3D microstructure). The area of the unit sphere is 4π steradians. The net spherical image consists of convexes, concaves and saddles as shown in Figure 2-3 [53]. This image is a function of number of the tangent vectors of the convex, concave and saddle as Eq 2-7 shows.

$$\Omega_{Vnet} = 2\pi(T_{V++} + T_{V--} - T_{V+-}) \quad [2-7]$$

where Ω_{Vnet} is the net spherical image, T_{V++} , T_{V--} , and T_{V+-} are the number of the tangent vector count for convexes, concaves and saddles, respectively. In addition, the net spherical image is numerically equal to the Euler characteristic.

$$\Omega_{Vnet} = 4\pi(N_V - C_V) \quad [2-8]$$

In the case of $N_V \ll C_V$ and $T_{V++} + T_{V--} \ll T_{V+-}$, connectivity density (volumetric connectivity) of a fully connected network in porous electrode is half the number of the tangent vector of the saddles per volume (V), as described in equation 2-9 [81].

$$C_V = \frac{1}{2VT_{V+-}} \quad [2-9]$$

Connectivity is closely related to tortuosity in terms of gas transport through the pore network. Connectivity offers possibility for the gas transport through the porous cathode. Tortuosity is related to the distance that gas must travel within the cathode bulk. In other words, gas prefers to follow along the less tortuous path through the interconnected channels if the connectivity is high. Quantification of the tortuosity and connectivity are tedious. A new sampling strategy, called disector probe, is applied to simplify the quantification process. The next section will introduce disector probe.

2.2.2.2 Disector probe

The disector probe technique characterizes the volume contained between two closely spaced plane sections (a small thin volume element). Compared to the serial-sections probe, the disector probe is not so stringent to orientational isotropy but emphasizes design of probes and sampling strategies [69]. One disadvantage of the serial-section probe versus the disector probe is a strong dependence on a computer processing. Therefore, the disector is very useful for dealing with a pore network in ceramics. By examining the changes that occur between successive sections at random sampling spots, the disector probe provides homogeneous topological information for a distributed feature in the 3D microstructure.

2.3 Transmission Electron Microscopy (TEM)

Transmission electron microscopy (TEM) uses a high-energy electron beam to image the microstructure of a material [86]. This technique permits high-resolution imaging, with point-to-point resolution of better than 2 nm. Therefore, it reduces measurement errors of the tertiary phase at the cathode/electrolyte interface as compared with the SEM due to the difference in the interaction volume, which is discussed in the following paragraph. Combining with the analytical TEM, it allows for recording interdiffusion between the cathode and the electrolyte by collecting the characteristic X-rays from the interaction volume. Furthermore, it provides information of present phases, crystal orientation and atom arrangement due to elastically transmitted electrons scattering within the interaction volume.

A variety of reactions occur when the high-energy electron beam interacts with the sample. Figure 2-4 shows the various byproducts due to these electron-sample reactions [86]. The shape and size of the interaction volume inside the sample depends on a number of factors, such as the atomic number of the components being imaged, the accelerating voltage being applied, and the incident angle for the electron beam. Higher atomic number materials absorb more electrons and

therefore have smaller interaction volume; higher accelerating voltages penetrate farther into the sample and generate larger interaction volumes; and the greater the incident angle, the smaller the interaction volume. Regardless of the interaction volume, these electron-sample interactions can be used to study various aspects of the material being imaged. Inelastically scattered electrons are incident electrons losing energy during the interaction. These electrons are then transmitted through the rest of the specimen. The inelastic loss of energy by the incident electrons produces characteristic x-rays or Auger electrons, which are characteristic of the elements that the beam interacted with. These energies are unique to the energy state of each shell of the atom and thus can be used to extract compositional information on the specimen region being examined. Therefore, these signals contributing to analytical TEM are collected to identify extra phases. It is well known that a portion of the electrons within the beam are transmitted through the sample without any interaction occurring inside the sample. These are commonly referred to as unscattered electrons. The transmission of unscattered electrons is inversely proportional to the specimen thickness. Areas of the specimen that are thicker will have fewer transmitted unscattered electrons and so will appear darker, conversely the thinner areas will have more transmitted and thus will appear lighter. Elastically scattered electrons are incident electrons that are deflected from their original path by atoms in the sample without loss of energy. These scattered electrons are then transmitted through the remaining portion of the sample. Since the electrons that follow Bragg's Law are scattered according to

$$\lambda = 2d \sin \theta \quad [2-10]$$

where d and θ are the interplanar spacing for a particular set of planes and the angle between the incident beam and the lattice plane of interest, respectively. All incident electrons scattered by the same atomic spacing will be scattered by the same angle. These scattered electrons can be

collected using magnetic lenses to form a diffraction pattern; an array of spots each of which corresponds to a specific interplanar spacing (i.e., an atomic plane). The interplanar spacing can be calculated by use of

$$Rd=\lambda L \quad [2-11]$$

where R is the measured distance between the transmitted beam and the diffracted spot of interest, λ is the wavelength of the electron beam, and L is the camera length being used. Since both λ and L are measured constants, the interplanar spacing can be calculated by measuring R. In the case of the cubic crystal structure, the corresponding d is compared to

$$d = \frac{a}{\sqrt{h^2 + k^2 + l^2}} \quad [2-12]$$

where a is the lattice parameter of the material being examined, and h, k, and l correspond to the Miller indices of the atomic plane [87]. If a is known, then the correct combination of Miller indices can be calculated. It should be noted that since the λL product is constant for a particular micrograph, the $R_1/d_2 = R_2/d_1$ comparison can be used to conveniently calculate neighboring lattice planes. Since the diffraction obeys the Bragg's law, the angle between R_1 and R_2 is an important parameter to rule out atomic planes which has the same ratio of d_1 to d_2 . Therefore, the diffraction pattern can be used to yield information about the orientation, atomic arrangements, and phases present in the area being examined.

Scanning and transmission electron microscopy (STEM) will be used to study interdiffusion between the cathode and the electrolyte. High resolution transmission electron microscopy (HRTEM) will be used to monitor the tertiary phase growth as a function of both sintering temperature and sintering time. In addition, crystal structure and orientation

relationship between the tertiary phase and two parent phases are identified by the HRTEM under both the isochronal and the isothermal sintering conditions.

2.4 Electrochemical Impedance Spectroscopy (EIS)

Electrochemical impedance spectroscopy (EIS) has been widely used in the fields of aqueous corrosion science and solid state ionics for probing the nature of electrochemical mechanisms [88]. It is a powerful tool to measure impedance of the SOFC components, $Z(\omega)$, as a function of a wide range of the characteristic frequency, ω , from 1mHZ to 1MHZ. This represents the kinetics of each electrochemical reaction in the SOFCs.

2.4.1 Fundamentals of EIS

The impedance of a device can be calculated as an alternating voltage, Δv , is applied between two electrodes and the resulting current, \dot{I} , is measured, according to the following equation :

$$Z(\omega) = \frac{\Delta v'}{I'} = \frac{\Delta v \sin(\omega t)}{I \sin(\omega t + \phi)} \quad [2-13]$$

where $Z(\omega)$ is a time-dependent variable, and consists of real impedance, Z_{real} , and imaginary impedance, Z_{imag} , which are plot as x-axis and y-axis in the Nyquist plot (Figure 2-5a), respectively. For a single electrochemical process, the Nyquist plot has a semicircle with a diameter coinciding with the x-axis. This simple Nyquist plot can be simulated with some equivalent circuit models, which consists of resistors and capacitors. The magnitude of the diameter, R_p , multiplied by the corresponding capacitance, C_p , indicates the time constant of the electrochemical reaction, τ , therefore the characteristic frequency, ω , for the specific chemical step as shown in equation 2-14,

$$\omega = \frac{1}{\tau} = \frac{1}{R_p \times C_p} \quad [2-14]$$

where C_p can be calculated based on Z_{imag} . Z_{imag} corresponds to the peak magnitude of the semicircle in the Nyquist plot, as described in the following equation:

$$Z_{imag} = \frac{1}{j\omega c} \quad [2-15]$$

Therefore, several steps in the oxygen reduction are identifiable if they have distinctive time constants. The transport of O^{2-} ions through solid electrolytes is generally the fastest process so it is observed at the highest frequencies (Figure 2-5a). This will change if the isolating phase on the electrolyte surface slows down transport of O^{2-} ions. If the charge-transfer is a fast electrode process but not as fast as O^{2-} ions conducting through the electrolyte so its contribution to the sample impedance is observed at intermediate frequencies (Figure 2-5a). Gas transport and adsorption/desorption of gas are both slow processes so they are observed at low frequencies, for the A.C., EIS case (Figure 2-5a). A time-constant for each of these processes has its own dependency on temperature, reactant concentration, materials, and microstructure. As a result, it is possible to differentiate serial reaction steps in the oxygen reduction by measuring the impedance as a function of the dependent variables (temperature, gas concentration, etc.), and by developing an equivalent circuit which fits the experimental data.

A modified Voigt equivalent circuit, which consists of a constant-phase element (CPE) in series (a resistor in parallel with a capacitor) (Figure 2-5b), is applied to deconvolute individual rate-limiting electrode reaction in this work. The assumption is that these individual rate-limiting electrode reactions (charge transfer reaction, dissociative adsorption reaction and gas transport reaction) are in serial within the whole oxygen reduction mechanism. Each rate-limiting electrode reaction has its own characteristic time constant. A nested equivalent circuit, which is composed of a double layer capacitor in parallel with a series connection of a resistor and a Voigt element, and then the double layer capacitor is in serial with a Voigt element, which

describes the electrical response of an electrochemical reaction with a strongly adsorbed intermediate, and includes components which contain the contribution of the surface concentration (coverage) of the adsorbed intermediate (mass transport, GT), the rate of adsorption or desorption (DA), and charge transfer reaction (CT) (Figure 2-5c) [171]. This circuit is applied in this work, because LSM is a major electronic conductive electrode, adsorption and/or surface diffusion can replace mass transport [89]. An accurate understanding of the cathode polarization depends on the determination of the sequence and the mechanisms of the electrochemical steps contributing to the oxygen reduction mechanism.

2.4.2 Error Analysis of EIS

There are many uncertainties on the sequence and the individual mechanism of the oxygen reduction mechanism, the big concern is about deconvolution of the impedance spectra, which is often hindered by the presence of a high-frequency ($>5 \times 10^4$ Hz) artifact. The influence of this artifact on the quality of the impedance data is described in details [89]. In that work, author attempts to use the Kramers-Kronig relations to examine the validity of impedance data. The objective is to study kinetics of chemical reaction happen within the frequency range of 6×10^3 to 8×10^4 Hz using valid high-frequency impedance data. Since many of the electrochemical steps of interest happen within the frequency range of 6×10^3 to 8×10^4 Hz, presence of a high-frequency-artifact can complicate data analysis. For ideal data, which is consistent with the Kramers-Kronig relations, Z_{real} and Z_{imag} share the same information. Failure of this consistency between the Z_{real} and the Z_{imag} corresponds to a failure of the experiment to comply with one or more of the constraints of linearity, stability and causality [90]. Therefore, utilization of the Kramers-Kronig relations enables one to identify and/or reduce error in the acquired data [91]. Smith et al. have found that the high-frequency can significantly alter electrochemical parameters attained when modeling the raw data. A high frequency correction process is proposed which significantly

increases the KK consistency of the high-frequency data, thus making high-frequency data more reliable.

A modified Voigt equivalent circuit (resistance-constant phase element, R-CPE) can be used to simulate the impedance response of many electrochemical phenomena as seen in Figure 2-5. For a single Voigt element in Figure 2-5a, the characteristic frequency of the individual process (the peak of the arc) in Figure 2-5d (Bode plot) is given by

$$\omega = \frac{1}{\tau} = (RQ)^{-\frac{1}{\alpha}} \quad [2-16]$$

where Q and α are parameters of the constant phase element. R represents individual reaction resistance. Each constant phase element in the modified Voigt element equivalent circuit represents a single electrochemical process seen as an arc in the Bode plot (Figure 2-5d). In the end, the individual reaction is differentiated from each other due to the distinct characteristic frequency of the various processes.

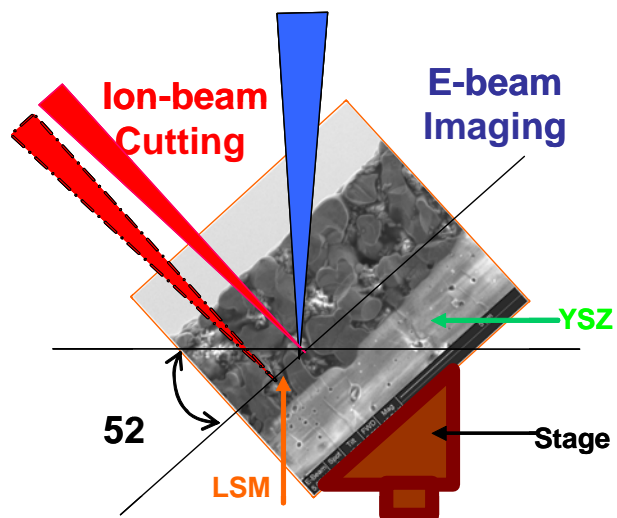


Figure 2-1. FIB geometry

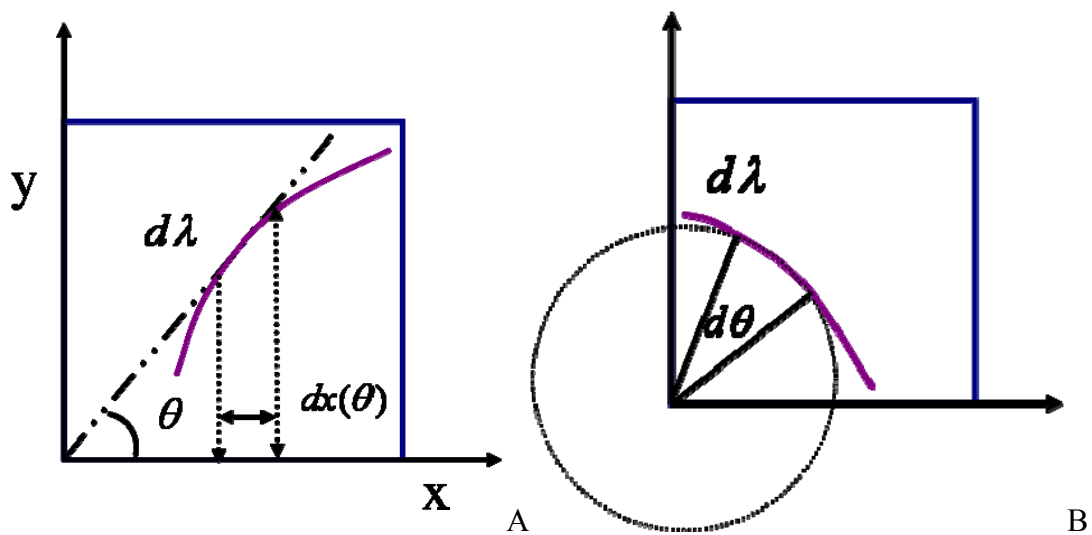


Figure 2-2. Sampling a curve with a line probe. A) Position probability. B) Rotation probability.

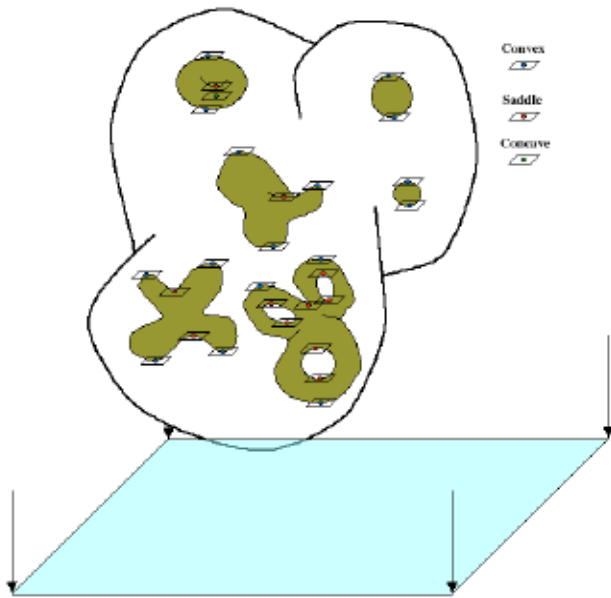


Figure 2-3. The calculation of net spherical image by counting number of concaves, convexes and saddles [53].

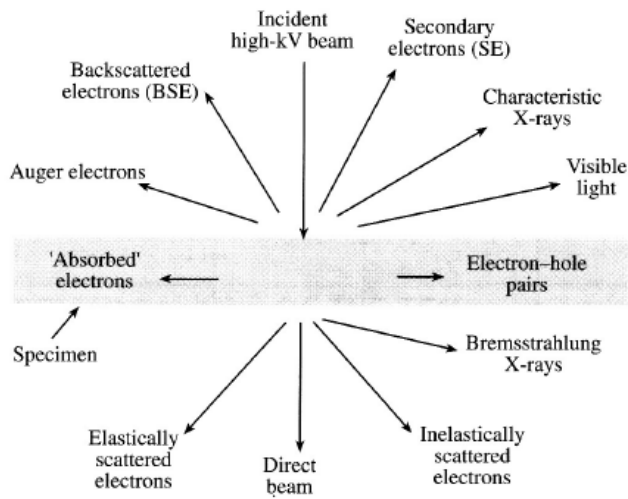


Figure 2-4. Interaction of a high-energy electron beam with a sample [86]

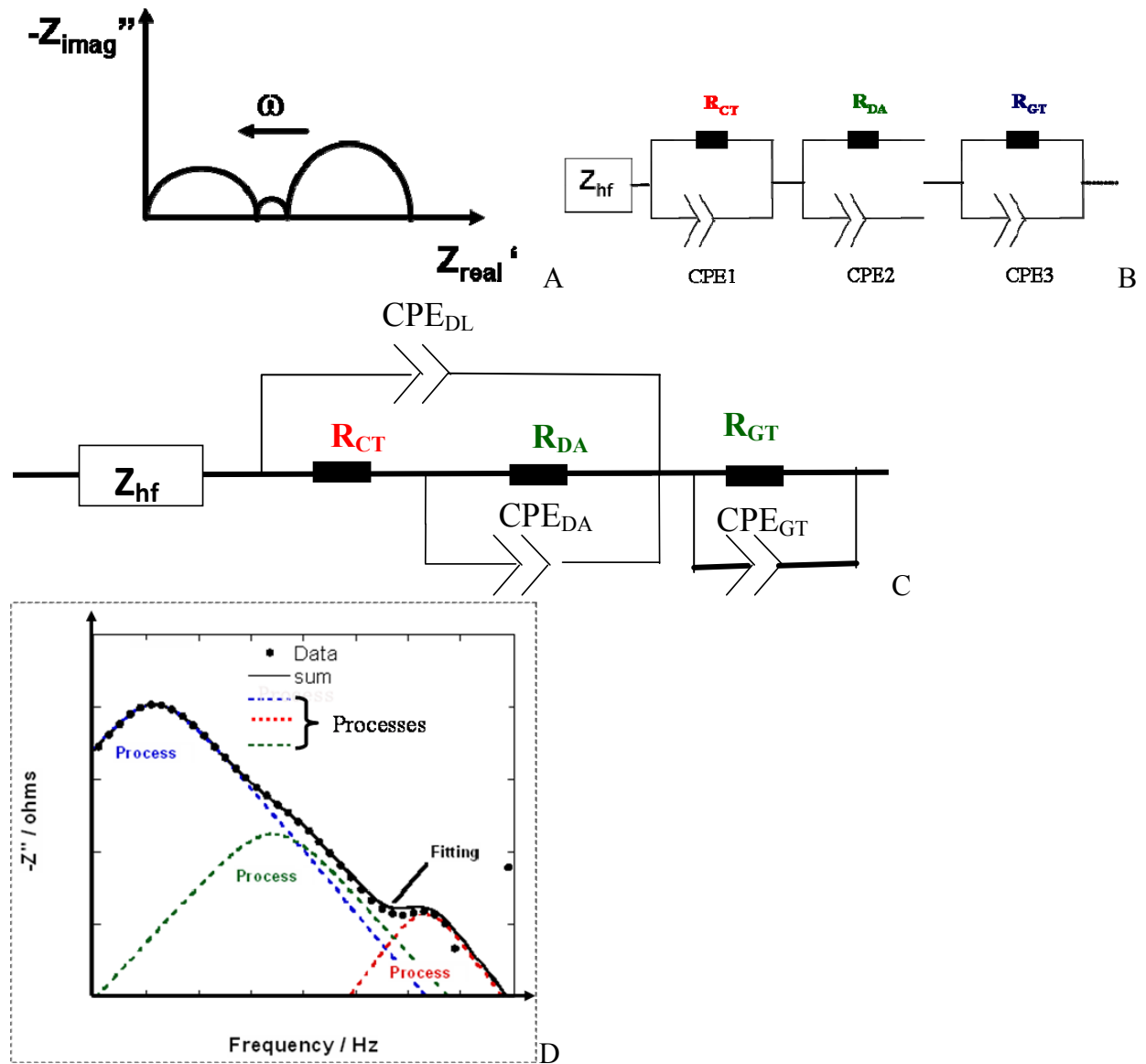


Figure 2-5. Individual resistance measurement using a modified Voigt equivalent circuit. A) Nyquist plot. B) Modified Voigt equivalent circuit. C) Nested equivalent circuit. D) Bode plot of impedance data.

CHAPTER 3 FIB/SEM TECHNIQUE DEVELOPMENT

The investigation of new FIB applications is a crucial point of this research. The focus of this chapter will be on FIB techniques for these advanced analyses, in particular, the statistical quantification of the metric properties of the Siemens-Westinghouse cathode-supported solid oxide fuel cell (SWCSSOFC) sample, the interfacial characterization of the SWCSSOFC sample, and the homogeneity study of the topology of the isothermally sintered samples will be reported.

3.1 Metric Property Analysis of the Composite Electrode

3.1.1 Introduction to the Composite Cathode

Ca-doped perovskite-type LaMnO_3 cathode (LCM) is an alternative to LSM. The electrical conductivity of the LaMnO_3 has been improved since Ca^{2+} has lower valence levels than La^{3+} . LCM also shows good compatibility of the thermal expansion and chemical properties with other SOFC component materials. Furthermore, LCM has the same perovskite-type crystal structure. However, differences in elemental properties might cause variations in lattice stability and thermal reactivity with the YSZ. It has been reported that zirconate formation can be easily avoided in LCM than in LSM [92] based on thermodynamic analysis.

Composite electrodes are commonly made by sintering simultaneously two kinds of powder. One is mainly electronic-conductive powder, another is mainly ionic-conductive powder. One of the main advantages of the composite cathode over a purely electronic conductive electrode is that in the composite cathode, the triple-phase-boundary active sites spread over the composite cathode bulk, whereas in a purely electronic conductive electrode, triple-phase-boundary active sites exist only at the purely electronic conductive electrode/electrolyte interface thus reducing SOFC performance. Since this chapter is mainly focused on the description of the development of FIB techniques by using the LCM/YSZ

composite cathode as a demonstration, oxygen reduction mechanism for this materials system is beyond the scope of this work. The objective of this section is to demonstrate FIB/SEM's capability of statistical quantification of the porosity and pore size of the composite LCM/YSZ cathode.

3.1.2 Quantification of V_v, S_v and Pore Size

Porosity (V_v) and pore surface area (S_v) can be quantified by area-probe and line-probe, respectively, which were introduced in section 2.2.1. The pore size (d_p) can be calculated by applying a geometric idea, mean line interception (λ) [53], which is defined as

$$\lambda = 4 \frac{V_v}{S_v} \quad [3-1]$$

The nature of the classical stereology can be displayed by FIB random serial sectioning.

3.1.3 Experimental Design

SWCSCOFC samples were made by Siemens-Westinghouse. Samples were prepared by the traditional manually polishing and by the low energy ion milling. The final thickness of the electrolyte was reduced from 50 μm to 10 μm . Before taking pictures from these samples, FIB serial sectioning geometries were decided based on how the specific microstructure properties affect the possible rate limiting steps. Metric properties (S_v and d_p) influence gas adsorption and dissociative adsorption occurring on the cathode surface, variation of metric properties (S_v and d_p) with height was captured in the cross-section images. The normal of the cross-section is parallel to the YSZ/LSM interface. Microstructure properties are related to gas transport gradually through the volume (on the top of the cathode surface to the LSM/YSZ interface), therefore, C_v , V_v , and τ are characterized by plane serial sectioning. Plane serial sectioning records continuously microstructure changes along the gas transport path. The normal of the plane-view section is perpendicular to the LSM/YSZ interface. Therefore, one geometry is the

milling perpendicular to the surface to collect cross-sections, and the other is the imaging on the top down (plane-view) while milling simultaneously parallel to the surface.

The sample was mounted on the 45° SEM holder for easy changes in FIB geometry. Before FIB cross-section imaging, a region which consisted of a thin layer of the electrolyte and a thick layer of the cathode was selected. The top of the electrolyte was tilted 7° toward the ion beam column. In this way, the FIB was perpendicular to the region of interest (ROI) during the milling of the electrolyte. The SEM (electron beam column) 52° away on the FIB (ion beam column), was applied automatically to collect a cross-section image of the smooth surface of the sample as shown in Figure 3-1a. The cross-section image shows the position of the cathode/electrolyte interface, therefore, the thickness of the electrolyte as well as the pore size of the cathode can be identified. The thickness of the electrolyte that is milled away up to the cathode/electrolyte interface decides the work volume of the plane-view imaging. In addition, the spacing of ~1/5 of the pore size between serial-sections during milling on the cathode/electrolyte interface to the top of the cathode will be verified to help keep track of the changes in the pores.

The plane-view serial-section images of the cathode were collected on the same ROI where cross-section images were collected. A series of fiduciary marks were patterned beside the ROI for accurate alignment. In this case, the side of the sample was tilted 7° toward the ion beam column (Figure 3-1b). FIB first milled away the whole layer of the electrolyte and left cathode/electrolyte interface as well as the cathode layer, then consequently milled into serial layers of the cathode with a repeatable spacing of about one fifth of the pore size (~1µm).

Before line probes were randomly oriented and placed across the whole cross-section or area probes were performed on the plane-section of the LCM/YSZ, the stacks of the plane or cross-section images were loaded into a ResolveRT software. After serial sections were aligned

and plane-view images were segmented, the number of interceptions of the line probe with the pore as well as area fraction of the pore in the segmented imaged were measured.

3.1.4 Results and Discussions

LCM/YSZ cross section was obtained using the FIB/SEM (Figure 3-2). A 30 μm wide by 60 μm deep trench was created to image and quantify the microstructure. Since electrolyte and the electrode have different crystal structures, channeling contrast of the ion beam was used to distinguish interfaces between the electrolyte and cathode phases. The microstructure on the top (region A) represents the dense microstructure of the YSZ electrolyte. Below the electrolyte (region B) lies a ~ 20 μm thick composite cathode (LCM-YSZ) with pores size on the order of 1-2 μm . The cathode support (LCM) below the composite cathode (region C) consists of coarser grains and larger pores > 2 μm .

The one μm thick series of slices was analyzed for porosity and pore size. Figure 3-3 shows the progression of the pores on the electrolyte up to the composite cathode. The corresponding quantification of pore size as a function of depth on the electrolyte surface to the porous cathode layer is shown in Figure 3-4. The x-axis represents the investigated depth away on the electrolyte layer (Figure 3-3a). The fluctuation of pore size and porosity is attributed to the large 8 μm slice thickness between each image.

Table 3-1 shows that the composite cathode region (8 μm -16 μm above the electrolyte) has finer, more closely spaced pores (Figure 3-3b), compared to the cathode support pores found at the 16 μm to 48 μm depth. Region A at Table 3-1 represents the electrolyte layer where no pores were observed. There exists a distribution of porosity and pore size in region B and C, which was observed in Figure 3-3b-f. Table 3-1 shows that the averaged pore size within regions of A and B is ~ 2 μm .

3.1.5 Conclusions

The FIB automated serial sectioning technique has been successfully developed to statistically characterize microstructure feature in 2-D combined with stereology. This technique can be expanded to other materials characterization. The FIB/SEM serially sectioned samples showed that the composite cathode region (LCM/YSZ) was ~20 μm thick with average pore diameter on the order of 1-2 μm . The cathode support above the composite cathode consisted of coarser grains and larger pores with the size of >2 μm . Porosity within these cathode regions ranged from 5% to 28%.

3.2 Interfacial Analysis of the Lanthanum Calcium Manganite (LCM)/YSZ Composite Electrode

3.2.1 Objective

It is well-known that TPB has been expanded into the LCM/YSZ interface within the bulk of the composite cathode. It has been recognized that the deleterious $\text{La}_2\text{Zr}_2\text{O}_7$ (LZO) phase is formed at the LSM cathode/YSZ electrolyte interface in co-sintering samples at high sintering temperatures [93-96]. The LZO formation dramatically degrades the cathode electrochemical properties [97-101]. It is crucial to characterize the formation of the tertiary phase at the interface of the LCM/YSZ composite cathode on atomic scale, for this purpose, HRTEM was used. However, it is always challenging to make an electron-transparent TEM cross-section sample on such porous and complicated oxides. Additionally, it is not easy to find the right position of the interface of the LCM/YSZ composite cathode.

3.2.2 Experimental Design

The LCM/YSZ cross-section was prepared by ion milling and then was polished by FIB ion beam. An ion-beam image was taken to find the position of the LCM/YSZ interface (Figure 3-2). SEM-EDS line-scans confirmed the position of the LCM/YSZ interface by composition

analysis. The in-situ TEM cross-section foil was prepared using a dual-beam FIB system and an in-situ Omniprobe manipulator at the LCM/YSZ interface (Figure 3-5a~d). The detailed descriptions of experimental procedures are shown in Appendix A Part one and two. A planarized region of interest was protected by Pt deposition on the top at the cross-section of the LSM/YSZ interface, then it was isolated by trenching surrounded areas with a Ga ion-beam milling current of 3nA, followed by ion polishing to a sample size of 32 μ m perpendicular to the LSM/YSZ interface \times 9 μ m parallel to the LSM/YSZ interface \times 1.5 μ m thick (Figure 3-5a). The TEM cross-section sample was released by undercutting on the LSM/YSZ interface after being attached to the in-situ Omniprobe-manipulator (Figure 3-5b). After the sample was transferred on the Omniprobe-manipulator to the Omniprobe Cu-grid, it was further thinned to 150nm by milling with the Ga ion beam current of 300pA (Figure 3-5c). A Ga ion beam current (50pA-100pA) was used for the final thinning (Figure 3-5d). The final sample thickness was <50nm thick to enable high resolution phase contrast imaging in the TEM.

High-resolution TEM was applied to characterize the LCM/YSZ interface. Several scanning transmission electron microscopy- energy-dispersive X-ray spectrometry (STEM-EDS) line scans were performed to more precise determine the LCM/YSZ interface position. These scans collected the characteristic X-rays on the LCM/YSZ interface with a tilt of $\sim 10^\circ$ to a X-ray detector. Selected area diffraction patterns were taken with a camera length of 25cm at different regions: LCM and YSZ far away from the LCM/YSZ interface, and LCM and YSZ at the LCM/YSZ interface. Diffraction patterns taken at the LCM at the LCM/YSZ interface covers larger area of the LCM than diffraction patterns taken at the YSZ at the LCM/YSZ interface. Vice visa. The aperture size of the selected area diffraction is 120nm. In order to observe details at the LCM/YSZ interface, in the presence of a tertiary phase, a bright field TEM (HRTEM)

image at high magnification was taken at the LCM/YSZ interface, when the electron beam was parallel to one of the major zone axis of YSZ.

3.2.3 Results and Discussions

This is a new sample preparation technique of the TEM cross-section foil that has never been attempted before but appears to work well for this type of structure. The advantage of using the Omniprobe grid is that the sample does not need to sit on a carbon film, which can interfere with the EDS analysis in the TEM. Also, by attaching the sample to an Omniprobe Cu grid, we were able to examine the sample in the TEM and subsequently thin it until the sample was sufficiently thin for high resolution phase contrast imaging. This technique allowed for STEM-EDS involving phase identification and lattice study at the atomic LCM/YSZ interface.

A high resolution TEM (HRTEM) image of the LCM/YSZ interface is shown in Figure 3-6a. The corresponding single phase diffraction patterns are shown in Figure 3-6b-c. The results are listed at Table 3-2. The diffraction pattern taken at the LCM region is shown in Figure 3-7a far from LCM/YSZ interface, and diffraction pattern taken at the YSZ region is shown in Figure 3-7d far from LCM/YSZ interface. Figure 3-7b covers larger area of the LCM than Figure 3-7c, and Figure 3-7c covers larger area of the YSZ than Figure 3-7b. YSZ diffraction spots are circled and the other diffraction spots are LCM. Most of the diffraction spots in Figure 3-7b and Figure 3-7c are LCM. Whereas diffraction patterns were taken with different emphases, structure information is the same. A high resolution phase contrast image of the LCM/YSZ interface is shown in Figure 3-8. Diffraction patterns taken at the LCM and YSZ bulk (Figure 3-7a and Figure 3-7d) were compared to those taken at the LCM/YSZ interface (Figure 3-7b and Figure 3-7c), no extra diffraction spots were observed at the LCM/YSZ interface (Figure 3-7a and Figure 3-7d). This indicates that there is no tertiary phase formation at the LCM/YSZ interface. Table 3-2 summarizes the indexed diffraction patterns of the LCM and the YSZ far from the

LCM/YSZ interface as shown in Figure 3-7a and Figure 3-7d. The difference in d-spacing between the reference values ($d_{8\text{YSZ}}$) and the calculated ones (d_{calc}) is a variation of mole percentage of Y_2O_3 dopant on the 8 mol%, in standard YSZ. The d-spacing of LaMnO_3 (LMO) should be different on the measured d-spacing (d_{calc}) after the addition of strontium. The R and d-spacing of LCM and YSZ are also summarized in Table 3-2. With the assumption that LCM and LMO have similar d-spacing, Table 3-2 shows that the LCM and YSZ are essentially phase pure. The high resolution phase contrast image is formed by interference effects of direct and diffracted beams (Figure 3-8). Periodic fringes within the LCM and the YSZ region displays high crystallinity of the LCM and YSZ, and the smooth interface between the LCM and the YSZ was observed everywhere except in a small transition region $< 6\text{\AA}$ thick. Phase contrast HRTEM indicates that a tertiary phase is unlikely to have formed at the observed LCM/YSZ interface. If a tertiary phase exists within this transition region, it is too thin to allow for diffraction collection.

3.2.4 Conclusions

This FIB sample preparation technique worked well for this type of the SOFC material. The STEM-EDS, diffraction patterns, and the HRTEM phase contrast was used to characterize the LCM/YSZ interface. All results show there was no tertiary phase formed at the LCM/YSZ interface.

3.3 Homogeneity Analysis

3.3.1 Objective

Disector probe enables investigations of the homogeneity of the distribution of the pore space within the cathode bulk by comparing the connectivity of each region of interest (ROI) with other ROIs. This provides a unique opportunity to identify the effectiveness and limits of the classical stereology for quantifying complicated pore-network and also to estimate the

number of the ROIs that should be analyzed by the classical stereology to get unbiased results before serial-sectional images are collected.

Homogeneity is one of the important assumptions for classical stereology quantification [49, 81, 83]. “Homogenous” in spatial statistics means “stationary” in physics. In other words, homogenous means that the distribution of the structure analyzed is translation invariant. Knowledge of the homogeneity of the pore-network is crucial to deciding effective usage of either classical stereology or 3D reconstruction analysis based on serial -sectioning in this work. Classical stereology is economical and effective for quantifying volume fraction (V_V) and interface densities (S_V) as well as line densities (L_{TPB}) [102, 103]. Additionally, the design of the classical stereology analysis determines the accuracy of the quantification of the metric properties. If 3D feature parameters (C_V and τ) are needed, 3D reconstruction analysis based on serial sectioning with simplified assumptions is required. Hence, homogeneity investigations provide further insight into the nature of the pore space. The nature of the pore space decides the operation of the classical stereology analysis and the 3D reconstruction analysis. This section examines the homogeneity of the distribution of the pore-network for the isothermally sintered samples using disector analysis. The experimental design that enables unbiased quantification of 2-D and 3-D geometric properties of the cathode is discussed.

3.3.2 Disector Analysis

The basic formula to perform the disector analysis has been introduced in section 2.2.2.2, connectivity density (C_V) can be quantified by calculating changes in number of connections (T_{V+-}) among pore networks per volume as written by

$$C_V = \frac{1}{2VT_{V+-}} \quad [3-2]$$

3.3.3 Experimental Design

Because this section is focused on FIB techniques, the sample preparation of the isothermal sintered $\text{La}_{0.78}\text{Sr}_{0.20}\text{MnO}_{3-\delta}/\text{YSZ}$ is described in section 4.1.3. In order to track changes in connections of a big volume of pore network, the cross-serial sections were collected with a spacing of $\sim 1/5$ of the pore size between two consecutive slides. This critical spacing was determined after several adjustments in spacing between two consecutive slides. There are not obvious changes in connections if the spacing is less than this critical spacing. It is too hard to track continuous changes in connections if the spacing is larger than this critical spacing. The disector analysis was performed on three pairs of the cross-serial sections on three random ROIs in all isothermally sintered samples. It covered an area of $15\mu\text{m}$ (the distance away from the YSZ/LSM interface toward the top of the cathode) by $15\mu\text{m}$ (the distance parallel to the YSZ/LSM interface). Connectivity density was quantified on twenty pairs of the plane-view sections and twenty pairs of the cross-section in one isothermally sintered sample. These plane-view disectors covered a distance ranging from $11\mu\text{m}$ to $20\mu\text{m}$ away from the LSM/YSZ interface. The cross-section disectors covered a distance of $10\mu\text{m}$ away from the LSM/YSZ interface. Twenty pairs of the cross-serial sections were taken on twenty random ROIs in the same sample. Each ROI is not related to one another. The area of the cross-section was $15\mu\text{m}$ by $15\mu\text{m}$. Another twenty pairs of the plane-view sections were taken on twenty ROIs for this isothermally sintered sample. Each ROI of the plane-view sections followed the same track along the same normal of the YSZ/LSM interface. Each ROI was randomly taken on a distance ranging from $11\mu\text{m}$ to $20\mu\text{m}$ away from the LSM/YSZ interface. The area of the plane-view section was $15\mu\text{m}$ by $15\mu\text{m}$. Changes in morphology of the sectioned features (saddles, concaves, and convexs) were compared within a finite volume of $15\mu\text{m}$ by $15\mu\text{m}$ by $\sim 1/5$ of the pore size, the

area sectioned by FIB was determined by the resolution of the FIB image and the time spent on disector analysis. The total distance being milled away along the normal of the LSM/YSZ interface (depth) was determined by a compromise between the resolution of FIB images and the depth of field of the FIB. $\sim 5\mu\text{m}$ was the total depth ($5\mu\text{m}$ away from the LSM/YSZ interface) for plane-view serial images to quantify 3D microstructure property. It is the critical distance that ensures accurate alignment of the serial-section images using the Amira software. It is not necessary to pre-process images artifacts before image analysis. These image artifacts are caused by corrections of the stage shifts.

3.3.4 Results and Discussions

The connectivity density was calculated on images with a pixel size of $0.019\mu\text{m}$ by $0.024\mu\text{m}$ on x and y dimensions, respectively. The pixel size in the z direction depends on the pore size of all isothermally sintered samples. It ranges from $0.044\mu\text{m}$ to $0.064\mu\text{m}$. Figure 3-9 shows the change in connectivity density as a function of the sintering time.

It appears that the connectivity density changes from one sample to another. Connectivity density for the sample sintered from 1h to 25h is initially increased then decreased. It is consistent with DeHoff's paper [104]. Initial increase of the connectivity density occurs because the number of contacts between particles within a given volume increases when volume shrinks. Decreasing in connectivity density occurs because pore channels close as the sintering time increases, thus reducing open porosity.

Figure 3-10 shows the connectivity density calculated on the serial-section images taken on 40 random cross-section and 40 random plane-section images. A gradient in open porosity is shown in Figure 3-11 as a function of the height of the sample. Connectivity density calculated on forty ROIs (twenty pairs of cross-section images and twenty pairs of plane-view images) was

compared within one sintered sample, and the results were statistically analyzed. T-test shows that the connectivity density is distinct within a confidence level of 95% between plane-view images and cross-section images. This might indicate nonhomogeneity of the sample on the micron scale. The plane-view disectors covered the region further away from the YSZ/LSM interface than the cross-view disectors. Connectivity density quantified by plane-section disectors is high within the distance ranging from 11 μm to 20 μm away from the LSM/YSZ interface. Connectivity density quantified by cross-section disectors is low within a distance 10 μm away from the LSM/YSZ interface. The connectivity of pore network is reduced when the pores are closer to the LSM/YSZ interface. The connectivity density is higher on the top half of the sample (Figure 3-10) because open porosity is higher (Figure 3-11). Disectors taken on the bottom half of the LSM give lower connectivity density (Figure 3-10) because open porosity is lower (Figure 3-11). Difference in connectivity density at different heights of the sample reflects the gradient of open porosity (the gradient in density of the cathode) (Figure 3-11).

Error bar of the connectivity density based on plane-view sections is less than a half of that on cross-section images. Of twenty sets of the plane-view disectors (first ten pairs taken from the top of one seventh of the LSM, from 17 μm to 20 μm away from the LSM/YSZ interface, and second ten pairs taken from the middle one quarter of the LSM (a distance from 16.3 μm to 11 μm away from the LSM/YSZ interface). T-test shows that connectivity density is 66% the same between twenty sets of the plane-view disectors. Whereas, only 20% of connectivity density is statistically identical between the twenty sets of cross-section images (taken at the bottom half of LSM, a distance of 10 μm away from the LSM/YSZ interface) with a confidence level of 95%. The connectivity does change less from the top half of the LSM (from 11 μm to 20 μm away from

the LSM/YSZ interface) than the bottom half of the LSM (from 0 μ m to 10 μ m away from the LSM/YSZ interface).

Connectivity based on cross-section disectors is so different that the twenty ROIs on cross-section are enough to differentiate geometric properties of different ROIs. These ROIs were taken within a distance of 10 μ m away from the LSM/YSZ interface. Additionally, more than 40 pairs of plane-section image are needed for differentiating topological properties. In this work, 25 ROIs will be studied for characterizing the metric properties. This means that precision of the measurements of the metric properties will be increased by 80% if ~25 ROIs have cross-section images taken for each sample. ~5 μ m (~100 plane-section images) away from the LSM/YSZ interface of one sample will be characterized for the topological properties. This number allows an increase in the precision of the measurements by 90% with the confidence level of 95%. The mean value of the topological properties will be two times closer to its averaged value of the topological properties. This conclusion is based on a comparison of an investigation of the 100 plane-section images to an investigation of the 40 plane-section images. It is a sufficient number to meet the requirement of the classical stereology.

3.3.5 Conclusions

The homogeneity of one sample was explored by the disector analysis of the connectivity density coupled with a T-test. Connectivity density appears to change as the distance away from the LSM/YSZ interface changes. Connectivity density for the isothermally sintered samples initially increased and gradually decreased with increasing sintering time. 20 sites were enough to identify significant differences in geometric properties of the cross-section. The number of cross-section images for metric property analysis and plane-view images for quantification of the

topology were decided to be 25 and 100, respectively. These optimized numbers enable unbiased quantification of geometric properties.

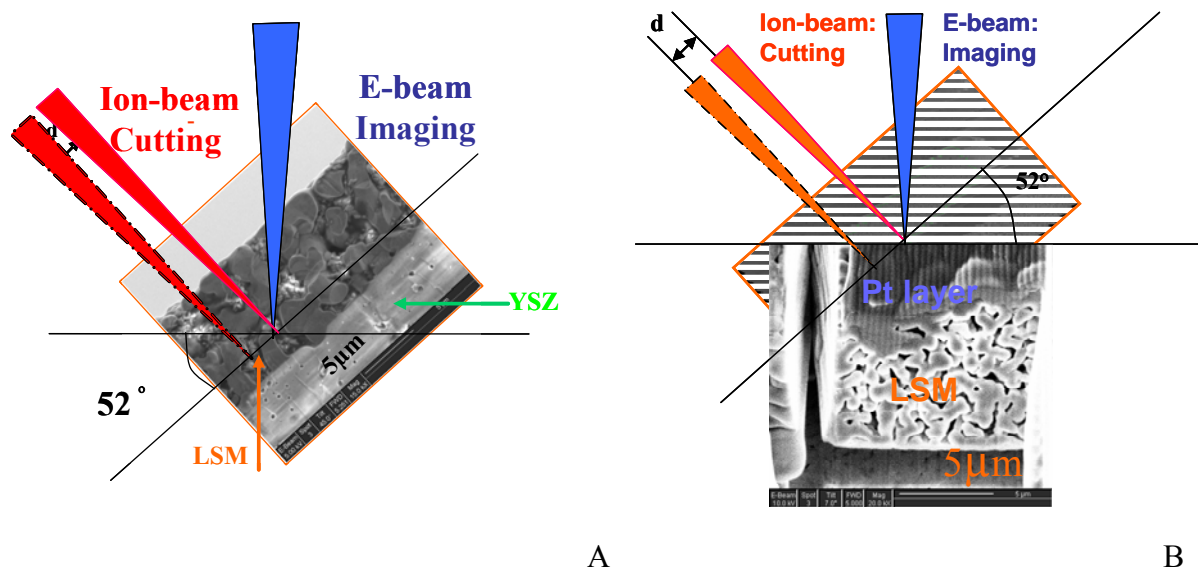


Figure 3-1. FIB flexible geometries. A) Cross-serial sectioning. B) Plane-serial sectioning

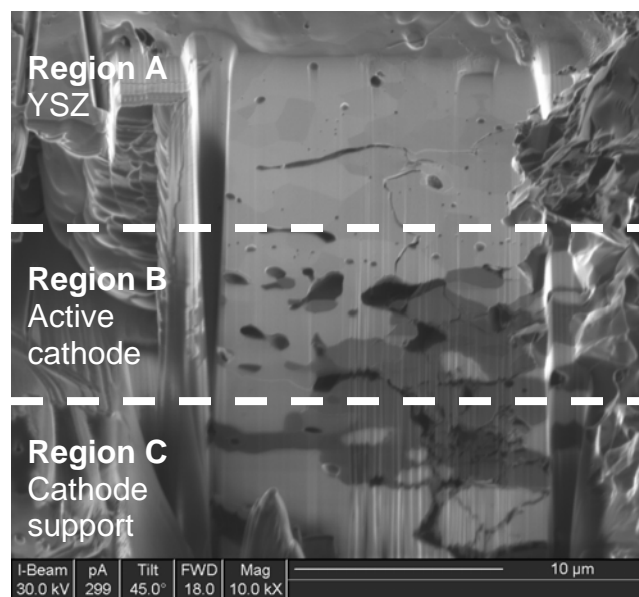


Figure 3-2. FIB/SEM cross section of cathode supported SOFC sample imaged with ion beam. Interfaces between LCM and YSZ are visible.

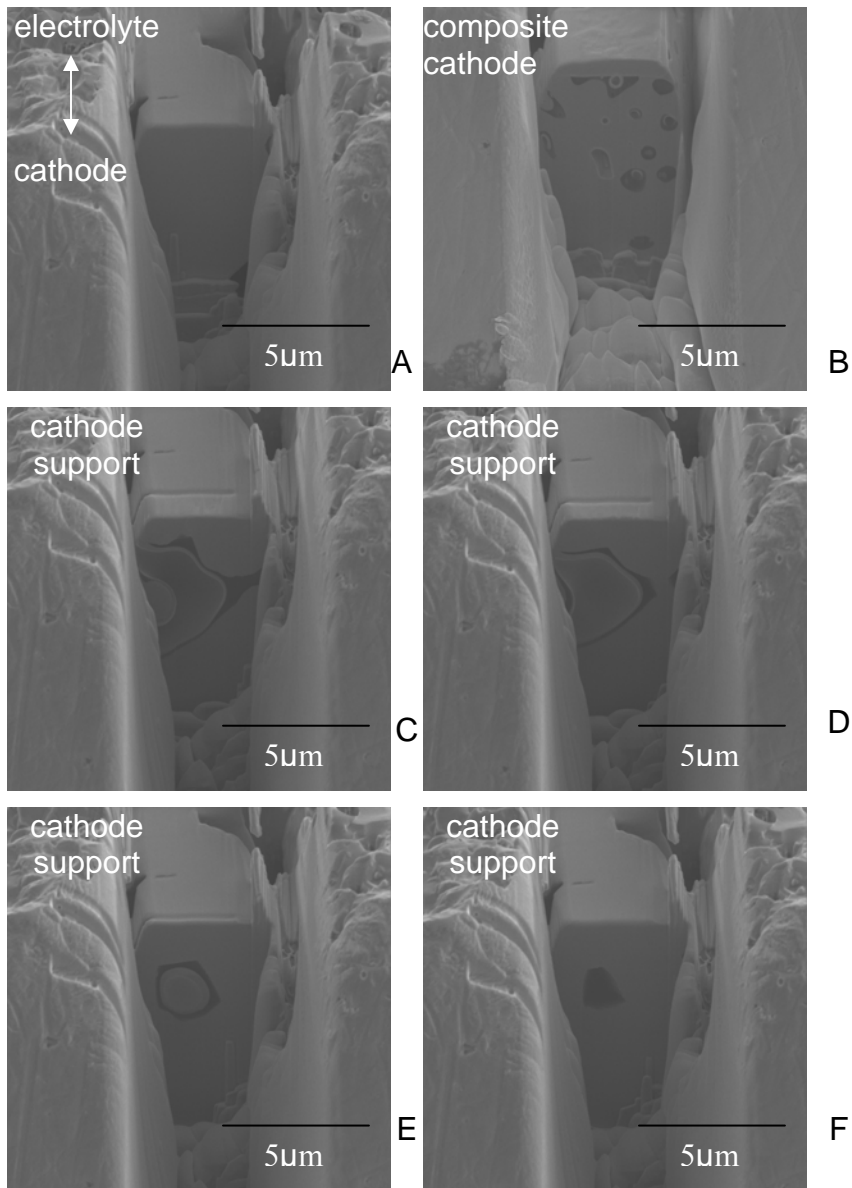


Figure 3-3. Pore migration on the dense electrolyte. A) Up through the composite cathode. B) Composite cathode. C-F) Cathode support.

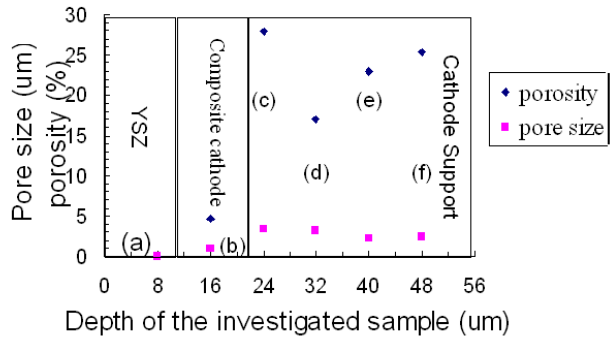


Figure 3-4. Pore size and porosity of the cross-section sample in Figure 3-3

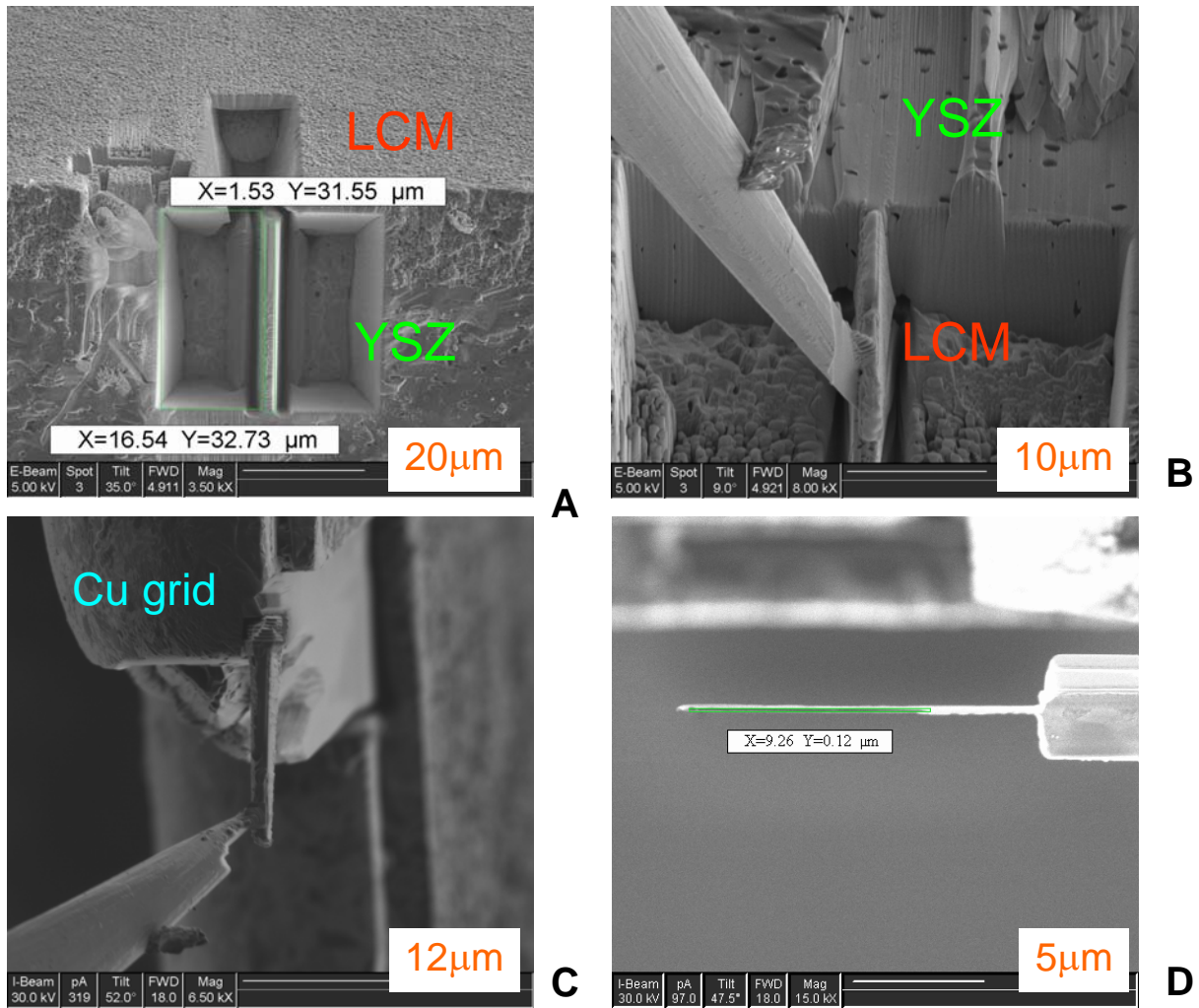


Figure 3-5. Schematic of Omniprobe-made TEM cross-section sample

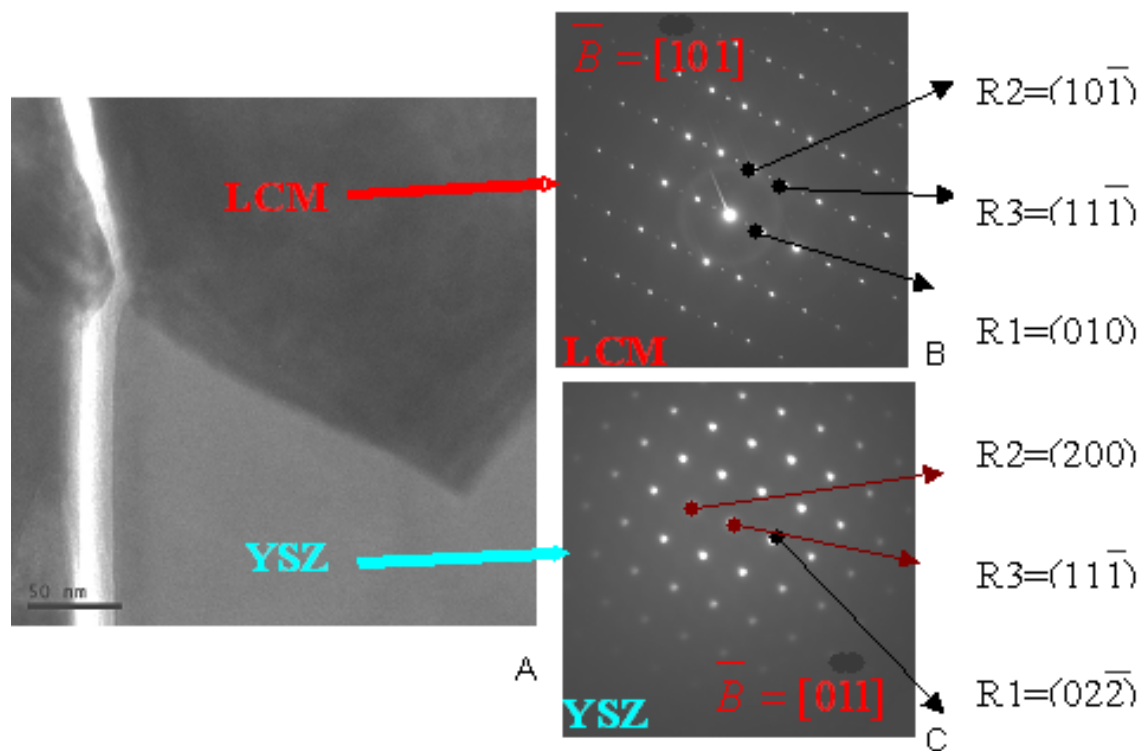


Figure 3-6. High magnification bright field image of LCM/YSZ and the corresponding diffraction patterns. Beam direction for LCM is $[101]$, and $[011]$ for YSZ A) Bright field image at the LCM/YSZ interface. B) Diffraction patterns of the LCM. C) Diffraction patterns of the YSZ.

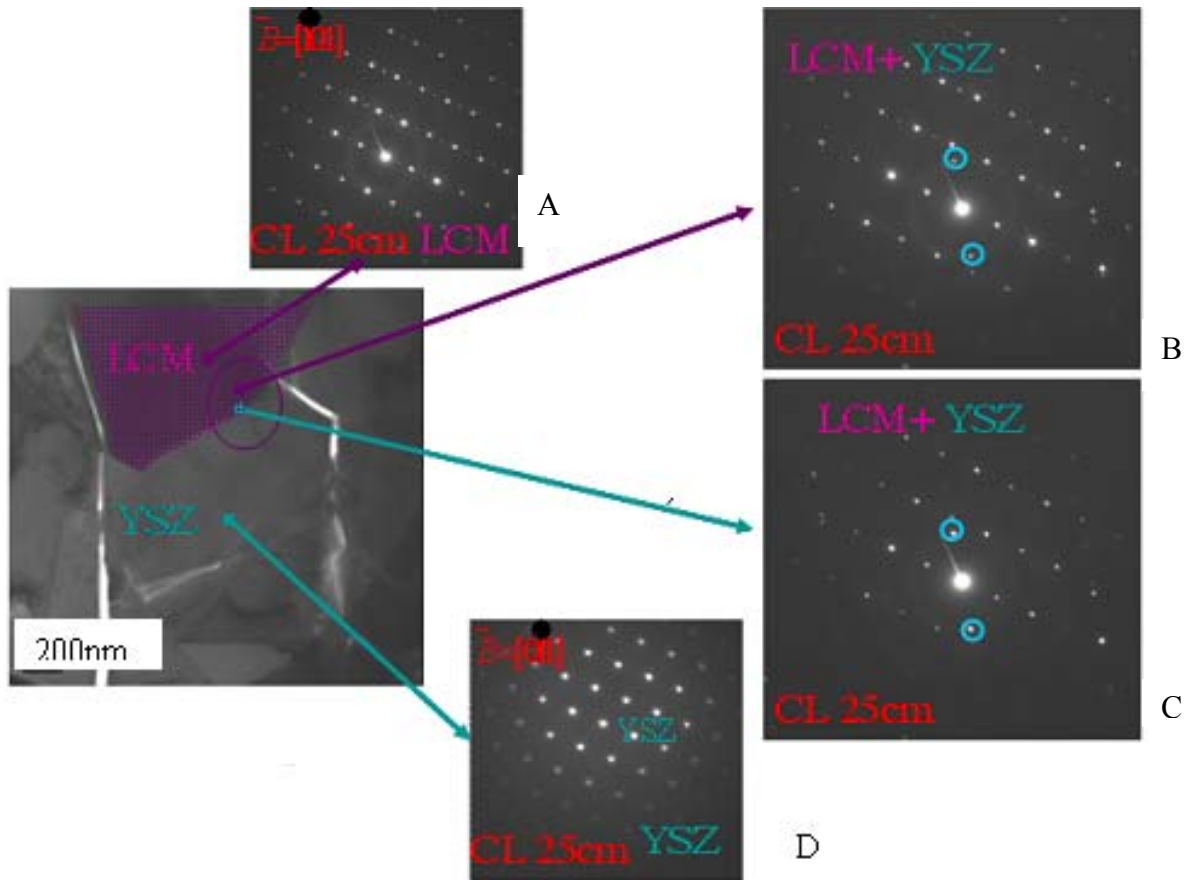


Figure 3-7. Comparison of diffraction patterns. A) Was taken at the LCM bulk ($B=[001]$). B-C) Were taken at the LCM/YSZ interface. D) Was taken at the YSZ bulk ($B=[011]$). Index as Figure 3-6).

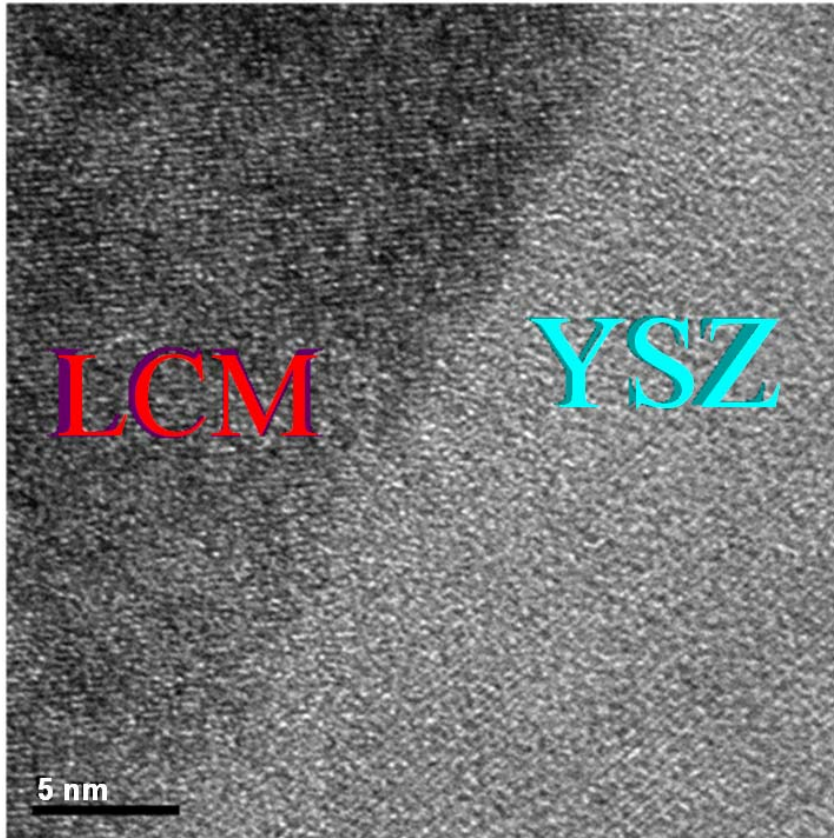


Figure 3-8. High resolution phase contrast image at the LCM/YSZ interface. LCM on the left and YSZ on the right have different crystallographic orientations, which correspond to different oriented periodic fringes. It is apparent that the LCM/YSZ interface is not rough.

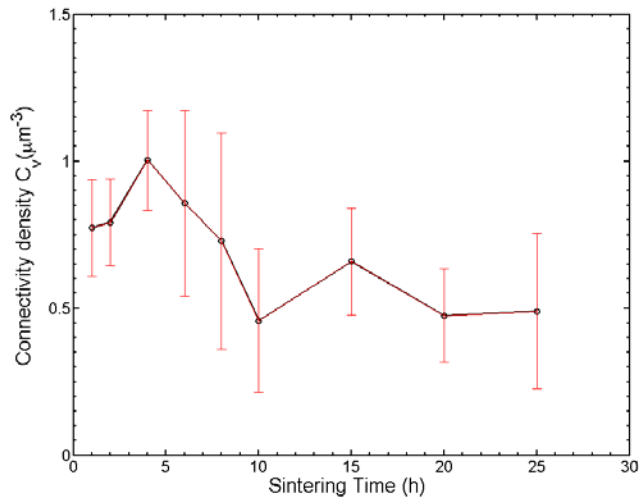


Figure 3-9. Homogeneity test of the isothermally sintered samples

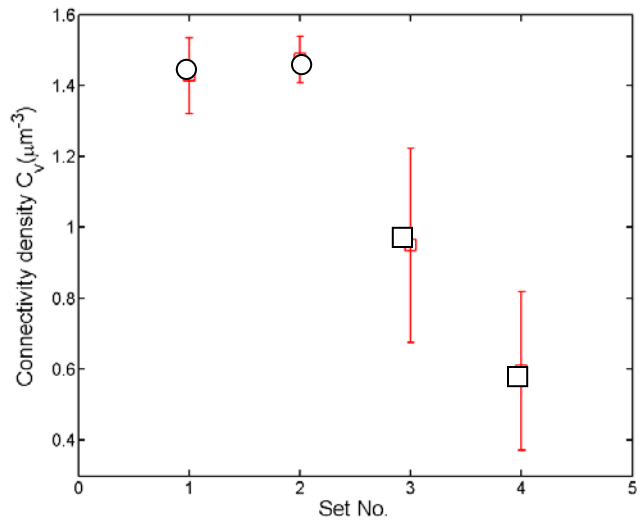


Figure 3-10. Homogeneity test within a sample. First two sets of data represent connectivity density based on plane-view serial stacks, which were taken from the top half of the cathode; last two show changes in connectivity density of the cross-section serial images, which were taken from the bottom half of the cathode.

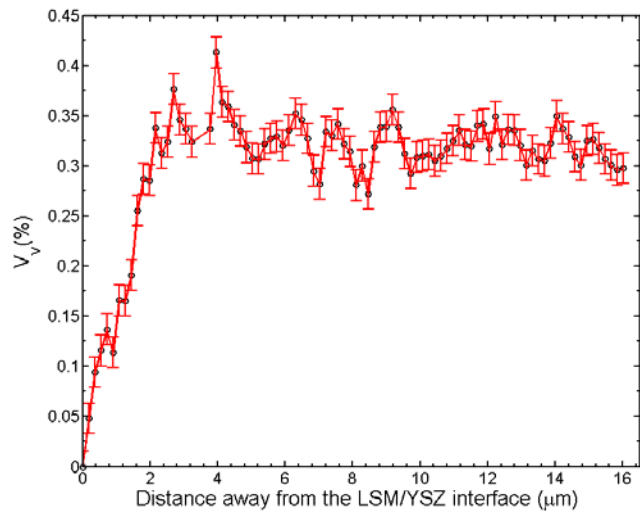


Figure 3-11. Open porosity gradient of one isothermally sintered sample

Table 3-1. Summary of porosity and pore size measurement

Region	Pore size (μm)	Porosity (%)	Depth of the region of interest (μm)
A-electrolyte	0	0	0~8
B-composite cathode	0.19~1.79	4.6	8~16
	1.07~5.81	27.84	16~24
	2.48~4.07	17.05	24~32
C-cathode support	0.7~3.87	22.9	32~40
	1.63~3.2	25.3	40~48
	0	0	0~8

Table 3-2. The R and d spacing of LCM and YSZ on TEM diffraction patterns

LCM $\bar{B} = [101]$				YSZ $\bar{B} = [011]$			
R(mm)	(hkl)	$d_{\text{LMO}} (\text{\AA})$	$d_{\text{calc}} (\text{\AA})$	R(mm)	(hkl)	$d_{\text{YSZ}} (\text{\AA})$	$d_{\text{calc}} (\text{\AA})$
$R_1=21.3$	010	3.96	3.7	$R_1=41$	022	1.82	1.9
$R_2=30.3$	$10\bar{1}$	2.80	2.6	$R_2=28.5$	200	2.58	2.8
$R_3=37.5$	$11\bar{1}$	2.29	2.1	$R_3=25.5$	$11\bar{1}$	2.97	3.1
$R_1=21.3$	010	3.96	3.7	$R_1=41$	$02\bar{2}$	1.82	1.9

CHAPTER 4 ISOCHRONAL SINTERING STUDY

This chapter will attempt to apply FIB techniques that were described in the previous chapter to study effect of the metric properties of the LSM/YSZ materials on activation polarization. In addition, this chapter will point out tertiary phase formation mechanism, which is ascribed to dramatic changes in metric properties and activation polarization under the isochronal sintering.

4.1 Effect of Metric Properties on Activation Polarization

4.1.1 Literature Review

Electrochemical impedance spectroscopy (EIS) are used to characterize the overall reaction resistance or interfacial reaction resistance (R_p) by studying changes in reaction kinetics [4, 105-107]. These reactions either occur within the electrode bulk or occur at the electrode/electrolyte interface. Previous work suggested that the interfacial electrochemical properties dominate SOFC performance [27, 93, 108]. It becomes important to study how the interfacial electrochemical polarizations are ascribed to interfacial reactions kinetics. It is necessary to understand the effect of the specific metric properties of the microstructure on the interfacial reactions kinetics. There have been many studies on the impact of the triple-phase-boundary length (L_{TPB}) on the interfacial reaction resistance (R_p) [4,109-111,107]. L_{TPB} affects efficiency of the charge transfer reaction occurring at the electrode/electrolyte interface. There exists a relationship between the charge transfer resistance and the L_{TPB} . This relationship varies if charge transfer resistance and L_{TPB} are quantified in different ways. In other words, if an overall interfacial resistance is assumed to be the charge transfer resistance [111], or if the shape factor of the triple-phase-boundary is neglected (Figure 4-1), (triple-phase-boundary is assumed to be

an ideal circle)[4, 109], then different dependences of the charge transfer resistance are obtained on the TPB length.

In my study of such an important relationship, the charge transfer resistance and the dissociative adsorption resistance will be separated from the overall resistance by using EIS [89]. FIB coupled with classical stereology enable us to quantify specific microstructure parameters. Microstructure parameters include triple-phase-boundary length, L_{TPB} , surface area of the pore/LSM interface, S_{cp} , as well as open porosity, V_v . Since my study is focused on the low current-density region, a linear proportionality law can be applied to describe the activation polarization of the cathode to the exchange current density, which is a function of microstructure parameters [26]. In my study, individual charge transfer resistance and dissociative adsorption resistance will be compared to L_{TPB} and S_{cp} .

4.1.2 Quantification of L_{TPB} and S_v

Three fundamental relationships are applied in the classical stereology analysis, two dimensional microstructural features can be simply quantified by a one dimensional line probe technique (see section 3.1.2). However, this quantification technique must be applied to open pores. More specifically, closed pores in the optical images must be differentiated with open pores before classical stereology analysis [49, 47]. Additionally, to get accurate measurement of the TPB length and pores, correctly applying classical quantitative stereology is as crucial as

identifying open pores to achieve unbiased estimations. Equation 2-2 ($L_{TPB} = \frac{\pi}{2} P_L$) and Equation 2-6 ($S_v = 2P_L$) can be applied to quantification of the metric properties of the microstructure.

4.1.3 Experimental Design

A set of nine symmetric SOFC samples was made by screen-printing LSM on both sides of the YSZ samples. The electrolyte used in the work contained 8 mol % yttria, the thickness of the YSZ is 150 μm , a 10mm \times 20mm sample was prepared from it by a tape cast method by Marketech International, Inc.. LSM ink, with a composition of $\text{La}_{0.78}\text{Sr}_{0.20}\text{MnO}_{3-\delta}$, was provided by Nextech Materials, Ltd.. The LSM ink was screen-printed on both sides of the YSZ with a square area of 64 mm². A drying step was performed in a Fisher Isotemp drying oven at 120°C for two hours. After drying, a set of nine isochronal samples was sintered at temperatures ranging from 950°C to 1400°C for one hour in Lindberg/Blue high-temperature box furnace. The resulting symmetrical samples had a cathode thickness of about 43 μm and YSZ thickness of 180 μm .

FIB/SEM experimental design in this section is referred from FIB techniques described in section 3.1.3 and section 3.3.3. FIB/SEM was operated at electron-beam energy of 5kV and a Ga ion beam current of 300pA. Thirty stacks of five cross-serial sections with a spacing of $\sim 1/5$ of the pore size were taken first from an area of 15 μm \times 20 μm . The magnification of the cross-section image was 15kX. Open pores at the LSM/YSZ interface were identified by observing pore evolutions in consequent slices. Then 25 cross-section images with the spacing of the pore size were taken randomly from this set of 150 cross-section images to quantify L_{TPB} and S_V . A line probe was applied right across the LSM/YSZ interface to quantify L_{TPB} , and two line probes were placed on the 25 cross-section with random angles to quantify S_V . Charge transfer resistance and dissociative adsorption resistance were obtained using electrochemical impedance spectroscopy [89].

4.1.4 Results and Discussions

The changes in the microstructure and the reaction impedance will be discussed as a function of the sintering temperature.

4.1.4.1 Effect of sintering on the cathode microstructure

The cross-section images of the LSM/YSZ in the isochronal sintering study are shown in Figure 4-2. Microstructure evolutions of LSM grains and pores, which were observed at these stages: (950-1200°C, 1200-1300°C and 1300-1400°C) in my study are common in the sintered ceramic materials [112]. Figure 4-2 shows that microstructure of the 1000°C sintered sample is similar to 1100°C in terms of grain size, but contact areas between LSM grains are slightly increased by neck growth of LSM grains [113]. Up to 1200°C, rapid grain growth and coarsening of LSM grains enclose continuous pore channels at LSM grain edge. On the other hand, rapid growth of pores continues and reduces the contact area between the cathode and the electrolyte [113]. Up to 1300°C, continuous pores are eventually pinched off. Closed pores are present at the LSM/YSZ interface (Figure 4-2 at the temperature of 1400°C). Densification of the LSM grains becomes evident. At such high temperatures, densification of cathode microstructure is likely caused by bulk diffusion of atoms to the grain boundary or by vacancy diffusion along grain boundary from pore channels [112].

4.1.4.2 Effect of metric properties on the reaction impedance

Figure 4-4a shows the TPB length as a function of the sintering temperature. It is found that TPB length is reduced from $1.41 \pm 0.07 \mu\text{m}/\mu\text{m}^2$ to $0.21 \pm 0.01 \mu\text{m}/\mu\text{m}^2$ as the sintering temperature increases from 950°C to 1350°C. This reduction is due to an increase in the grain size from sintering. Figure 4-4b shows the pore surface area as a function of the sintering temperature. Pore surface area decreases from 5 to $0.5 \mu\text{m}^2/\mu\text{m}^3$ as the sintering temperature increases. Pore surface area at 1350 °C is eight times smaller than that of 950 °C (Figure 4-4b).

Decreasing of the pore surface area is caused by growth of pore from sintering [113]. The charge transfer resistance increases from 1 to 300Ω as a function of the sintering temperature (see Appendix B Figure B-7). The comparison of the TPB length to the charge transfer resistance is showed in Figure 4-5. The charge transfer resistance increases as the TPB length decreases. The rapid increase of the charge transfer resistance correlates strongly with the abrupt reduction in the TPB length upon sintering above 1200°C. Reduction in TPB length contributes to a loss of the number of active sites for the charge transfer reaction, thus increasing the charge transfer resistance. The dissociative adsorption resistance is quadrupled from 100 to 400Ω as a function of the sintering temperature (see Appendix B Figure B-8). The dissociative adsorption resistance increases by a factor of 4 as the pore surface area decreases by a factor of 3 (Figure 4-6). The decreasing trend of the dissociative adsorption resistance slows down when the pore surface area is larger than $3.3\mu\text{m}^2/\mu\text{m}^3$. The increasing of the pore surface area increases the active area for the dissociative adsorption reaction, this appears to lead to a decrease in the dissociative adsorption resistance.

The microstructure evolution of the sintered sample is consistent with the effect of the sintering temperature on TPB length and pore surface area. The TPB length is decreased by 23% starting from 1000°C to 1200°C (Figure 4-4a) and the corresponding pore surface area slowly decreased (Figure 4-4b). Both TPB length and pore surface area are reduced gradually as a function of the sintering temperature. Neck growth of the LSM grains competes with pore growth at the LSM/YSZ interface, contact areas between LSM grains and pores at the LSM/YSZ interface are decreased slightly thus reducing slightly TPB length. Consistent with Figure 4-5, it shows that the charge transfer resistance increases only by one time as TPB length decreases gradually. This phenomenon was previous observed by other studies of interfacial resistance

around the sintering condition of the 1200°C [95, 114-116]. Slight pore growth leads to the slight decrease of the pore surface area. The pore surface area was decreased by 27% in the range of 1000-1200°C and results in the decrease of the active area for the dissociative adsorption reactions. The growth of pores results in the slight decreasing of the pore surface area [113], as a consequence, the dissociative adsorption resistance was increased by 6% (Figure 4-6). This can be explained by the fact that pore area determines the area exposed for dissociative adsorption of oxygen and therefore affects the cathode activation polarization. The pore surface area falls sharply between 1200°C and 1300°C (Figure 4-4b). As a result, the dramatic decrease of TPB length by 57% causes a dramatic increase of the charge transfer resistance by four times, as shown in Figure 4-5. The rapid decrease of pore surface area by 63% results in the dramatic increase of the dissociative adsorption resistance more than 188% (Figure 4-6). It is noted that the dissociative adsorption resistance was increased suddenly and rapidly within this temperature range. It might indicate that connected pores start to close channels thus reducing pore surface area rapidly [113]. From 1300°C to 1400°C, microstructure images in Figure 4-2 show a combination of grain densification and formation of closed pores. Up to 1400°C, TPB length and pore surface area are reduced to ~0 [113] due to complete densification of the LSM microstructure. Unfortunately, resistance values are too high to be determined by EIS measurement within this temperature range. Densification of the microstructure reduces tremendously the available TPB boundary area, which is close to zero, for the charge transfer reaction. In addition, isolated pores inhibit transport of oxygen molecules or diffusion of the oxygen intermediates to reaction sites at the LSM/YSZ interface.

It is apparent that microstructure evolution above 1200 °C degrades the electrochemical properties of the sintered samples [93]. The study of this dramatic evolution of the

microstructure and its effect on the observed increase of the cathode polarization upon the isothermal sintering at 1200 °C will be discussed in section 5.1.

4.1.5 Conclusions

In summary, the cathode activation polarization, which consists of charge transfer resistance and dissociative resistance, depends on two aspects of the microstructure: TPB length and pore surface area. Consistent with common sintering behavior of the ceramics material, the isochronal sintering study displays three stages of the sintering as following:

1) First stage (950 °C -1200 °C): Neck growth of the LSM grains competes with pore growth at the LSM/YSZ interface, the gentle reduction in contact areas at the LSM/YSZ interface reduces gradually TPB length. This appears to be correlated with a slight increase in the charge transfer resistance. Slight reduction in the pore surface area due to gradual increasing of the pore size causes the gradual rise of the dissociative adsorption resistance. Both TPB length and pore surface area are not reduced abruptly as a function of the sintering temperature. This is consistent with gradual reduction trends in both the charge transfer and the dissociative adsorption resistances at this temperature range.

2) Second stage (1200 °C -1300 °C): Rapid grain coarsening of cathode microstructure leads to abrupt decreases of the grain/pore contact area [113] at the LSM/YSZ interface thus reducing dramatically TPB length. This appears to be correlated with a dramatic increase of the charge transfer resistance. Rapid growth of pores and continuous pore channels enclose at LSM grain edge cause the dramatic reduction in the pore surface area [113]. This appears to increase dramatically the dissociative adsorption resistance. Reduction slopes in both metric properties (TPB length and pore surface area) at this temperature range are at least two times as steep as the slopes in the temperature range of 950-1200 °C. Reduction in the activation

polarizations (charge transfer and dissociative adsorption resistances) are more rapidly at this temperature range than the temperature range of 950-1200 °C.

3) Final stage (1300 °C -1400 °C): Densification due to grain growth decreases abruptly TPB length, and formation of closed pores reduces dramatically pore surface area [113]. As a result, TPB length and pore surface area are close to zero at 1400 °C. Therefore, both charge transfer resistance and dissociative adsorption resistance increases tremendously. It should be noted that the magnitude of the charge transfer resistance being increased at this stage is seven times larger than increase in the L_{TPB} at the second stage. It does not follow a linear proportional law. TEM results of tertiary phase formation at the LSM/YSZ interface will explain this dramatic change in the activation polarization (see section 4.2.3.3).

4.2 Tertiary Phase Formation Mechanism

4.2.1 Literature Review

Tertiary phases, lanthanum zirconate (LZO) and/or strontium zirconate (SZO), increase cathode polarization due to their lower ionic conductivity than YSZ [108]. For cathode materials with Sr<30mol%, $La_2Zr_2O_7$ (LZO) is the only tertiary phase [93, 28]. The deleterious LZO phase was observed at the LSM/YSZ interface for co-sintering at high temperatures [36, 93-96]. LZO phase degrades the cathode electrochemical properties [97-101]. Therefore, the focus of some work are on how to avoid or control formation and growth of zirconate phases by adjusting composition of La [6], modifying fabrication method of the cathode, and sintering processing [118]. Specifically, how LZO formation depends on La activity is the popular topic.

Yokokawa et al. predicted the possible reactions between LSM and YSZ to form LZO by thermodynamic study. LZO can be avoided if La composition is less than ~86mol% [119]. Chen et al. studied LZO phase diagram and showed that LZO formation could not be avoided by substituting a LSM cathode with a La deficient LSM. LZO formation is rather dependent on Y

composition in YSZ than dependent on La insufficiency in LSM [120]. Absence or retarded formation of the LZO has been confirmed by XRD [35] and SEM analyses [27] at the A-site (La, Sr) deficient LSM/YSZ interface. LZO can be avoided or minimized due to low cation activity of the LSM [27, 28, 35]. However, previous studies of LZO formation were limited by the poor detection limits of XRD and SEM or by the challenge of making TEM cross-sections of the interface, numerous studies of LZO formation focused on either very long time anneals (>100h) at low temperature (<1473K) or shorter anneals (<10h) at high temperature (>1473K). In order to identify factors of the initial stages of LZO formation, a few studies of the LZO formation by TEM were performed.

4.2.1.1 Lanthanum zirconate (LZO) formation mechanism

Tricker et al. reported the morphology evolution of the LZO phase nucleation at the LSM/YSZ interface by HRTEM [36]. LZO nucleates on the YSZ surface, forming bridge-like connections [121, 36] and LZO grows primarily into the LSM phase. Loss of contrast in the bright field image near the LZO/LSM interface contributes to the presence of a new Mn-deficient LSM phase at the LZO/LSM interface. Misfit dislocations were observed at the LZO/YSZ interface. Loss of Mn appears to be the primary cause of LZO formation. Mn diffusion alters the LSM stoichiometry beyond the solubility limit of La. This rejected La reacts with YSZ to form LZO [121, 122].

Mitterdorfer et al. further analyzed the nucleation mechanism for the initial stages of LZO by using HRTEM, atomic force microscopy (AFM) and EIS [6]. Of particular interest is the comprehensive analysis of the effect of the A-site (La, Sr) nonstoichiometry on the LZO formation and the detailed kinetics study of the LZO formation at the A-site rich $\text{La}_{0.85}\text{Sr}_{0.15}\text{Mn}_{0.98}\text{O}_3$ /YSZ interface. AFM experiments showed that cube-like LZO embryos were initially formed and grown in diameter and height, and then LZO islands were formed by

combining LZO embryo with one another. Mitterdorfer et al. suggested that LZO islands grow between the cathode grains and the YSZ surface towards the cathode, although cathode layer was etched before TEM sample preparation. Surface diffusion of Zr cations along the side of the LZO island to the top of the LZO island controls the growth of the LZO islands. As soon as the YSZ surface is entirely covered by LZO, further growth is limited by bulk diffusion or grain boundary diffusion of Zr cations [6]. LZO phase was formed in a distinct way at the A-site deficient $\text{La}_{0.85}\text{Sr}_{0.15}\text{Mn}_{1.02}\text{O}_3$ /YSZ interface. Mn-rich YSZ rings were detected initially on top of the YSZ surface by HRTEM and AFM (Figure 4-3a). They were formed after sintering for two hours at 1100°C . LZO grains start to nucleate on the top of the Mn-rich YSZ rings until La_2O_3 forms (Figure 4-3a and Figure 4-3c). After a sintering time of twelve hours at 1100°C , ring-shaped LZO islands were observed on top of the Mn- ZrO_2 rings by HRTEM (Figure 4-3b). LZO is precipitated after La_2O_3 reacts with ZrO_2 at the TPB (Figure 4-3c). LZO growth in this Mn excess LSM is controlled by the reductive decomposition of the LSM, which supplies La cations for the LZO reaction [6]. Tricker et al. and Mitterdorfer et al. showed that LZO insulating layer starts to nucleate at the TPB.

Structure analysis was performed by Tricker's and Mitterdorfer's groups. An epitaxial relationship between the LZO and the YSZ was reported by both groups [6, 36] based on diffraction patterns taken at the YSZ/LZO interface [6] (Figure 4-3d). The epitaxial growth of LZO occurs because it consumes a low energy. This epitaxial relationship depends on the crystal orientations of the YSZ [36]. The splitting of the LZO reflections represents a slight misorientation ($\sim 1^\circ$ tilt) of the diffraction patterns existing between LZO and YSZ.

In order to quantify the probability of the LZO phase formation, many groups calculated activation energy for various stoichiometries of LSM under different sintering conditions [6-8,

123]. An Arrhenius law was applied to extract the slope of the rate constant vs. the reciprocal temperature (the activation energy of the LZO phase formation). The rate constants of the LZO formation were determined using an established method [7, 123, 124]. This method assumes that the LZO thickness increases linearly with the square root of time.

4.2.1.2 Open questions

Among the few studies of LZO formation at the initial stage, Mitterdorfer et al. mainly focused on the kinetics of the LZO formation in various stoichiometric A-site rich LSM, especially in the A-site rich $\text{La}_{0.85}\text{Sr}_{0.15}\text{Mn}_{0.98}\text{O}_3$ /YSZ interface [6]. However, the ability to measure the thickness of the LZO layer by AFM is compromised if the acid etching process removes any of the LZO layers [6] or if the sample is too thick to accurately measure the initial stages of LZO formation by TEM [36]. There are no in-depth kinetics studies of the initial stages of LZO formation at the A-site deficient LSM/YSZ interface in the literature at present.

The following section reports on a study of the initial stages of LZO formation using the TEM/EDS analysis. TEM enables to monitor the formation of the LZO at the A-site deficient LSM/YSZ interface at an early stage. Based on TEM measurements of the LZO thickness, the formation mechanism of the LZO and the kinetics of the interfacial reactions to form LZO will be discussed. The effect of the LZO formation on the charge transfer resistance will be briefly addressed.

4.2.2 Experimental Design

A set of nine SOFC samples with a composition of $\text{La}_{0.78}\text{Sr}_{0.20}\text{MnO}_{3-\delta}/8$ mol % Y_2O_3 -92 mol % ZrO_2 was prepared (section 4.1.3). This set of nine isochronal samples was sintered at temperatures ranging from 950°C to 1400°C for one hour. TEM cross-section foils of four samples were prepared with a Dual-beam FIB system and an in-situ Omniprobe manipulator.

The details were described in section 3.2.2. The TEM analysis was performed on this set of four isochronally sintered samples.

High-resolution TEM was applied to characterize the LSM/YSZ interface. The diffusion profile was characterized by scanning transmission electron microscopy- energy-dispersive X-ray spectrometry (STEM-EDS). The structure orientation relationship was determined by selected area diffraction with an aperture size of 1200 Å. Diffraction patterns were taken with a camera length of 25cm in the YSZ bulk far away from the LSM/YSZ interface, and at the YSZ/LSM interface. Fixed position EDS of the LSM bulk, LSM/YSZ interface and YSZ bulk were performed to determine the tertiary phase composition. In addition, adjacent fixed spots were placed at the region of interest 15nm-40nm apart. These scans collect the characteristic X-rays from the LSM/YSZ interface with a tilt of ~10° to an X-ray detector. Diffusion profiles of the different species at the LSM/YSZ interface were constructed. EDS line scans were also collected. Thickness of the tertiary phase was measured based on the corresponding bright field image, which was taken when the electron beam was parallel to one of the major zone axis of the YSZ. This procedure was repeated for four isochronally sintered samples (1100°C, 1200°C, 1300°C, and 1400°C). The rate constant (r) for tertiary phase formation was estimated by using the Wagner equation of $r = \frac{x^2}{t}$, where x is the LZO thickness determined by TEM and t is the annealing time.

4.2.3 Results

4.2.3.1 LZO composition profile

Figure 4-7 and Figure 4-8 show TEM results of the 1200°C one hour sintered sample. Figure 4-7a shows a bright field image taken at a high magnification. The LZO layer is present between the LSM grains and the YSZ surface (Figure 4-7a) on three samples sintered at 1200°C,

1300°C and 1400°C. A sharp boundary was observed in the bright field image of the LSM/LZO interface. A tertiary phase was present at the LSM/YSZ interface analyzed by STEM-EDS on each of three samples (1200°C, 1300°C and 1400°C). Figure 4-7b represents the typical EDS concentration profiles of this tertiary phase. The tertiary phase contains La and Zr (Figure 4-7b). Vertical lines have been placed on the EDS line scan to indicate the approximate location of the interfaces between phases. It should be noted that no Mn was found in the LZO and the YSZ regions. No ZrO₂ was observed between the YSZ and LZO region. The Zr concentration decreases in the YSZ region. Figure 4-9 shows TEM results of the 1100°C one hour sintered sample. Figure 4-9a shows a sharp boundary at the LSM/YSZ interface, Figure 4-9b represents the corresponding STEM-EDS profile. A transition region with high concentration of La and Zr was not observed in the 1100°C sintered sample. The change in concentration of Mn and La appears the same at the LSM/YSZ interface.

4.2.3.2 Epitaxial relationships

Diffraction patterns were obtained both from the YSZ bulk and the LSM/YSZ interface for each of three samples (1200°C, 1300°C and 1400°C). Structural results are the same. Diffraction patterns taken in the YSZ bulk and at the YSZ/ LSM interface are showed in Figure 4-8a and Figure 4-8b, respectively. The corresponding high resolution phase contrast images are shown in Figure 4-8c and Figure 4-8d, respectively. Figure 4-8a shows the cubic-fluorite structure of the YSZ with the zone axis of [011]. The tertiary La and Zr-rich phase appears to form coherent interface with the YSZ (Figure 4-8c). The diffraction patterns for the two phases appear very similar and well aligned. It is known that the tertiary phase has a different pyrochlore crystal structure. The more intense diffraction spots in Figure 4-8b came from the tertiary phase matrix, these are identified as La₂Zr₂O₇ (LZO) based on d-spacing. The small spots in an array

correspond to double diffraction [95]. Several pairs of diffraction spots, each consisting of two spots in close proximity to one another, are identified from both LZO and YSZ.

$$[011]_{LZO} // [011]_{YSZ}$$

$$(22\bar{2})_{LZO} // (11\bar{1})_{YSZ}$$

Therefore, LZO shows the epitaxial relationship to the YSZ, which is confirmed by lattice image at the YSZ/LZO interface (Figure 4-8c), in which $\langle 111 \rangle$ in YSZ extends into LZO, and overlaps with $\langle 222 \rangle$ LZO. No parallel relationship was observed from a lattice image at the LZO/LSM interface (Figure 4-8d). In addition, some misfit dislocations were observed at the YSZ/LZO interface both in the corresponding lattice image (Figure 4-8c) and in the bright field image shown in Figure 4-7a. There remains $\sim 1^\circ$ tilt between the epitaxial relationship between LZO and YSZ.

Figure 4-9 and Figure 4-10 show TEM results of the 1100°C one hour sintered sample. There exists a sharp boundary in both bright field image (Figure 4-9a) and lattice image (Figure 4-10c) between the LSM and YSZ phase in the 1100°C sintered sample. Figure 4-10b shows that YSZ has a cubic-fluorite structure with the major zone axis of $[001]$. The more intense diffraction spots in an array in Figure 4-10b came from the YSZ matrix. The small spots correspond to the LSM phase. The angle of $\sim 18^\circ$ between the YSZ (200) plane and the diffraction plane of the LSM in diffraction patterns is consistent with the plane orientation between the YSZ and the LSM in the lattice image as shown in Figure 4-10c. Extra diffraction spots were not observed at the LSM/YSZ interface. It is consistent with the absence of the tertiary phase region in STEM-EDS profile of the LSM/YSZ interface (Figure 4-9b).

4.2.3.3 Kinetics of the tertiary phase formation

The LZO thickness of the isochronal sintered samples increases as the sintering temperature increases (Figure 4-11). The rate constant of the LZO formation at 1200°C in $\text{La}_{0.78}\text{Sr}_{0.20}\text{MnO}_{3-\delta}$ is lower than LZO rate constant at 1100°C in $\text{La}_{0.85}\text{Sr}_{0.15}\text{Mn}_{0.98}\text{O}_3$ [6] (Figure 4-12).

4.2.4 Discussion

4.2.4.1 Tertiary phase formation mechanism

Mn is the most mobile species [7]. EDS suggests that Mn diffuses further into the LSM bulk and reduces the ratio of the B-site (Mn) to A-site (La,Sr) in the LSM lattice, and then the La-rich LZO region causes the tertiary phase to form in the LZO region (Figure 4-7b). In addition, Mn diffusion causes such a La-rich LSM that La^{3+} is able to react with Zr^{4+} in the YSZ lattice to form a LZO layer at the LSM/YSZ interface [6, 121, 122]. Therefore, formation of the La and Zr-rich layer is mainly controlled by Mn diffusion [6, 7, 95]. LZO formation cannot be avoided with a La composition less than 86mol% [6, 120]. STEM-EDS results of the LSM/YSZ interface suggest there are no Mn in the YSZ and the LZO regions, and suggest an absence of ZrO_2 near the YSZ/LZO interface. The detection limit of the STEM-EDS is ~1 mol%. If there were 1 mol% Mn, the Mn composition (at most 1 mol%) is much lower than the 7.4 ± 1.0 mol% Mn in the Mn-rich YSZ ring and the 7 mol% Mn in the ZrO_2 islands detected by TEM-EDS in Mitterdorfer's study [6]. In addition, EDS results support absence of Mn near the LSM/LZO interface (Figure 4-7b). The sharp boundary of the bright field image suggests that a new phase was not observed near the LZO/LSM interface (Figure 4-7a). It contradicts with Tricker's observation. Tricker mentioned that a Mn-depleted LSM phase contributes to the contrast loss of a LSM region near the LSM/LZO interface in a TEM bright field image [14]. It is possible that

changing the chemistry of the cathode and varying sintering conditions contribute to differences in Mn diffusion.

The epitaxial relationship between the LZO and the polycrystalline YSZ was observed as discussed in all samples sintered above 1100°C. These samples have LZO phase. This epitaxial relationship is independent of the different crystalline orientations of the polycrystalline YSZ. It does not change as a function of the sintering temperature (1200°C -1400°C for one hour sintering), and the sintering time (1h-25h at 1200°C), which will be describe in section 5.1. The inconsistency with the Tricker's structural analysis is attributed to the wider range of sintering conditions being studied in this work. Misfit dislocations at the YSZ/LZO interface (Figure 4-7a) are responsible for the small misorientation of $\sim 1^\circ$ of the diffraction patterns at the YSZ/LZO interface as shown in Figure 4-8b [6, 36]. A roughly 1° tilt between the epitaxial relationship between LZO and YSZ corresponds to the small misfit strain of $\sim 4.88\%$ between the LZO and YSZ [6].

It is not clear where the initial interface of the LSM/YSZ is located. Structural information of the sample sintered at 1200°C suggests that the initial interface of the LSM/YSZ is located at the YSZ/LZO interface, and misfit dislocations at the YSZ/LZO interface support that the initial interface of the LSM/YSZ has low mobility. The epitaxial LZO starts to grow at the LSM/YSZ interface and grows toward LSM [6, 36]. However, if the initial interface of the LSM/YSZ is located at the YSZ/LZO interface, then it is not clear where the Zr comes from in the LZO layer. No mass balance is observed between Zr in YSZ and Zr in LZO. If the initial LSM/YSZ interface is located in the middle of the LZO [7], then EDS concentration results explain that Zr comes from YSZ and La comes from LSM in the LZO layer. However, the epitaxial growth usually grows perpendicular to the YSZ/LSM interface. Further study of the surface morphology

is needed to determine where the LSM/YSZ initial interface is located. Apparent slopes of the La at the YSZ/LZO interface and Zr at the LZO/LSM interface may be artifacts of the EDS scans. La has at most 1.5mol% solubility in the YSZ [119, 120].

It has been proposed that there are two stages for the LZO formation at the LZO/YSZ interface [6, 36]. During the first stage, the interface reaction is mainly controlled by diffusion of Mn out of the LSM lattice. As a result, the La in LSM reacts with the Zr in YSZ to form a LZO layer. During the second stage, LZO is epitaxially grown away from the parent phase, YSZ, into the LSM grain [36].

4.2.4.2 Delay of the tertiary phase formation

The established method [7, 123, 124] of determining the rate constants at different sintering temperatures will be confirmed in the isothermal sintering study. The isothermal sintering study shows that the LZO thickness increases linearly with the square root of time from 1h to 25h (section 5.2.4). In my study, no LZO was observed after 1100°C sintering for one hour (Figure 4-10). The minimum thickness detected by HRTEM is $\sim 10\text{\AA}$, thus the LZO thickness was assumed to be less than or equal to 10\AA to calculate the maximum rate constant of the LZO formation at 1100°C. Figure 4-12 compares the rate constant of LZO formation as a function of sintering temperature, determined by the TEM measurements in my study with the rate constants of LZO formation from the study of Mitterdorfer, which were calculated by AFM measurements [6]. Mitterdorfer et al. reported that increasing the ratio of A-site to B-site from 1:0.95 to 1: 1.02 retards the formation of LZO. In my study, no tertiary phase was observed after one hour sintering at 1100°C with the ratio of A-site to B-site, 1:1.02. This is consistent with the report of Mitterdorfer: after four hours sintering at 1100°C with the same ratio of A-site to B-site (1:1.02). The rate constant of the LZO formation at 1200°C in my study is lower than the result in the study of Mitterdorfer at 1100°C (Figure 4-12). The ratio of A-site to B-site (1:1.02) in my

study is at least 4% lower than the ratio of A-site to B-site (1:0.98 and 1:0.95) in Mitterdorfer's study. As the sintering temperature is increased above 1100°C, LZO formation increases dramatically despite the lower A-site to B-site ratio. Therefore, changing in the ratio of A-site to B-site will not prevent LZO formation [6, 28, 120] but appears to delay its formation [6, 120]. It is possible that the decrease in A-site to B-site ratio stabilizes the LSM thus retarding LZO formation. In other words, LZO formation is retarded by excess amount of Mn and insufficient supply of La [6].

The activation energy calculated based on my study (170 ± 10 KJ/mol) is comparable to other stoichiometric LSM: 168 (KJ/mol) for $\text{La}_{0.85}\text{Sr}_{0.15}\text{MnO}_3$ [7, 124] and 167 (KJ/mol) for $\text{La}_{0.65}\text{Sr}_{0.3}\text{MnO}_3$ (although this paper reported both SZO and LZO formation) [7]. There does not appear to be a significant effect of the ratio of A-site to B-site on the activation energy for LZO formation. However, this is difficult to confirm given that many variables involved in these various studies including characterization techniques, variation in sample composition, different sintering histories etc. If the activation energy at higher temperatures is not significantly affected by the stoichiometry of the LSM materials, then the effect of varying the A-site to B-site ratio discussed by Mitterdorfer is probably related to a change in the attempt frequency of the reactions.

4.2.4.3 Change in the interfacial resistance

The relationship between the charge transfer resistance and the triple-phase-boundary length (Figure 4-4) shows that the decrease of TPB length by 57% causes an increase of the charge transfer resistance by four times above 1200°C. On the other hand, the charge transfer resistance is only increased by 52% as decreasing TPB length by 22% below 1100°C. TEM study showed that LZO phase was observed above 1200°C. LZO formation at the LSM/YSZ

interface inhibits oxygen ion conduction to the LSM/YSZ interface, thus LZO phase blocks the supply of the oxygen vacancies from the YSZ to the TPB [107]. Oxygen vacancies are one type of reactant species for the charge transfer reaction. A reduction in concentration of the oxygen vacancies directly decreases the exchange current density at the LSM/YSZ interface as described in the Faraday's law, as a result, charge transfer resistance increases. Therefore, this effect can account for the dramatic increasing in charge transfer resistance between 1200°C and 1300°C.

Both reduction in TPB length and LZO formation are attributed to the Mn diffusion at the LSM/YSZ interface. LZO formation at the LSM/YSZ interface is controlled by Mn diffusion. Excess Mn stabilizes LSM thus retarding LZO formation. The reduction in the amount of the active sites is caused by Mn diffusing away the LSM/YSZ interface. Absence of Mn in the LZO region in STEM-EDS profile (Figure 4-7) suggests Mn diffusion away the LSM/YSZ interface. STEM-EDS profile shows vacancy evolution on the nanometer scale. Mn diffusion enhances vacancy concentration at the LSM/YSZ interface [26]. Increasing in vacancies concentration at the LSM/YSZ interface on the scale of the nanometer is consistent with pore growth at the LSM/YSZ interface as showed in cross-section FIB/SEM image (Figure 4-2). Cross-section FIB/SEM image shows vacancy evolution on the micron scale. Reduction in contact area among LSM/YSZ/Pore (TPB length) is attributed to the pore growth at the LSM/YSZ interface.

In the isochronal sintering study, a quantitative study of the cooperative effects of the LZO formation and triple-phase-boundary length on charge transfer resistance is not focused on, since many dependent variables are involved at the same time in this isochronal sintering study, such as distinct microstructure evolutions and their different contributions to the LZO formation. Therefore, an investigation of an isothermal sintering, under which the effect of the microstructure evolution on the cathode performance is minimized, will show the influence of

LZO formation and the effect of reduction in L_{TPB} on the interfacial resistance. This open question will be answered by the isothermal sintering study described in the Chapter5.

4.2.5 Conclusions

FIB in-situ Omniprobe manipulator has been applied to make electron-transparent TEM cross-section samples from A-site deficient LSM/YSZ material. This sample preparation technique enables the study of the LZO formation kinetics of an initial stage. The kinetics study of the LZO formation clarifies the delay of the LZO formation in previous thermodynamic studies, whether La deficiency avoids or retards the LZO formation. HRTEM, STEM-EDX analysis, diffraction pattern and lattice image at YSZ /LZO interface indicate that LZO phase formation is not avoided but is retarded by reducing La composition. Comparison of rate constants of LZO reaction in 1100°C samples shows that decreasing the ratio of A-site (La, Sr) to B-site (Mn) is necessary for retarding LZO formation. LZO phase formation is controlled by Mn diffusion at the interface. Rate constants for the interfacial reaction were affected by Mn concentration within samples sintered between 1100°C and 1400°C for one hour. The different observations of Mn diffusion and of the epitaxial relationship between the LZO and the YSZ were emphasized. The interfacial reaction between the LSM and the YSZ does not cause a new Mn-deficient phase formation at the LSM/LZO interface. The structural analysis shows an epitaxial relationship between the LZO phase and the YSZ. The epitaxial relationship does not change with different crystalline orientations of the YSZ. Calculated activation energy of the LZO formation for this ratio of A-site to B-site (1:1.02) is similar to those of previous studies with different stoichiometry of LSM. LZO formation appears to correlate well with the dramatic increase in the charge transfer resistance above 1200°C. Further study of the isothermal sintering is needed to answer this question.

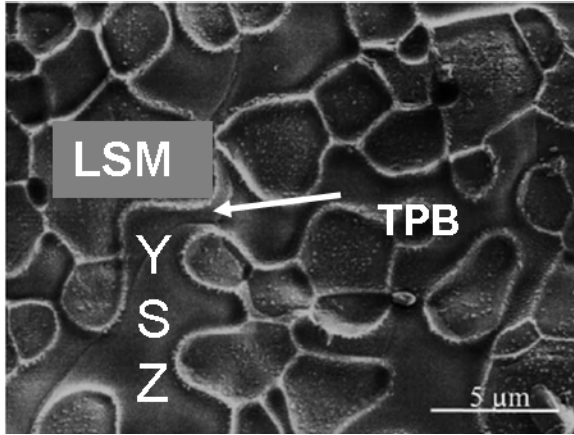


Figure 4-1. Top view of the LSM/YSZ interface. The sharp outline is the triple-phase-boundary.

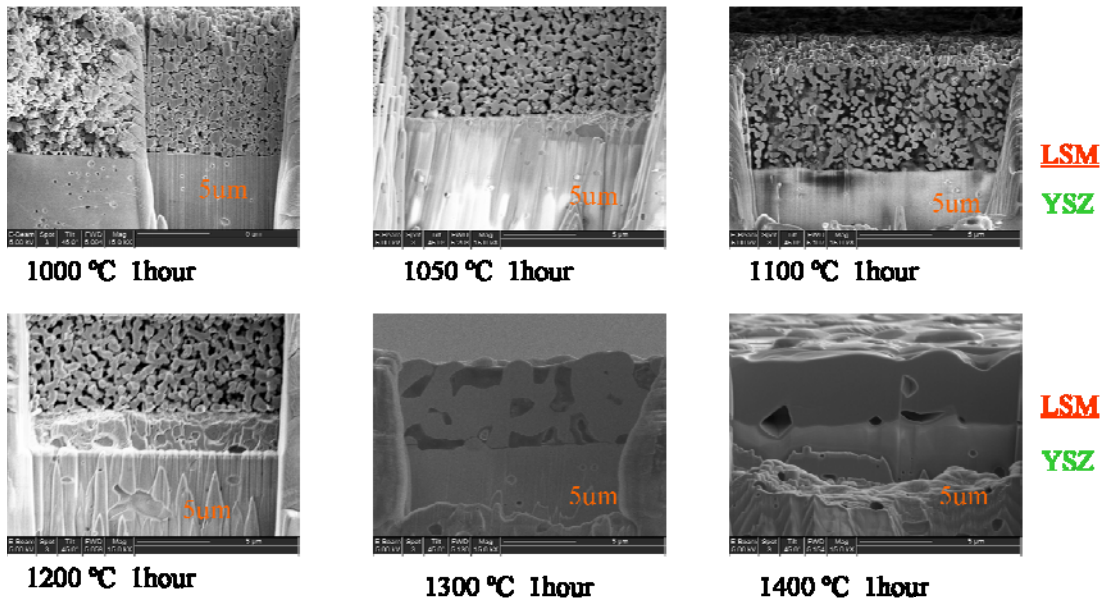


Figure 4-2. Cross-section images of the isochronal sintered samples

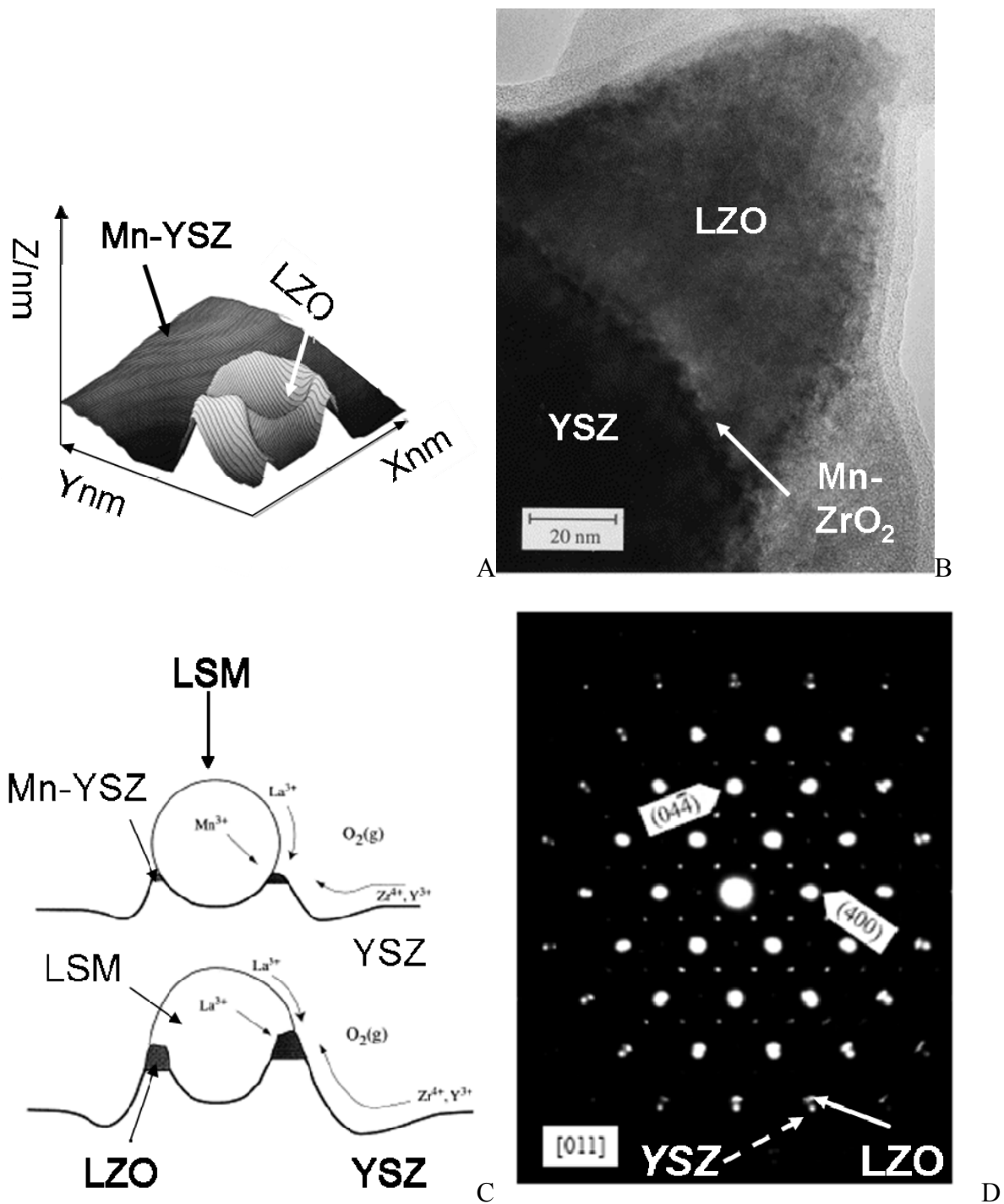


Figure 4-3. LZO formation by Mitterdorfer et al [6]. A) On Mn-rich YSZ ring detected at the A-site deficient LSM/YSZ interface by AFM. B) On Mn-rich ZrO₂ detected at the A-site deficient LSM/YSZ interface by HRTEM. C) Proposed LZO formation mechanism at the A-site deficient LSM/YSZ interface. D) Epitaxial relationship at the A-site rich LSM/YSZ interface.

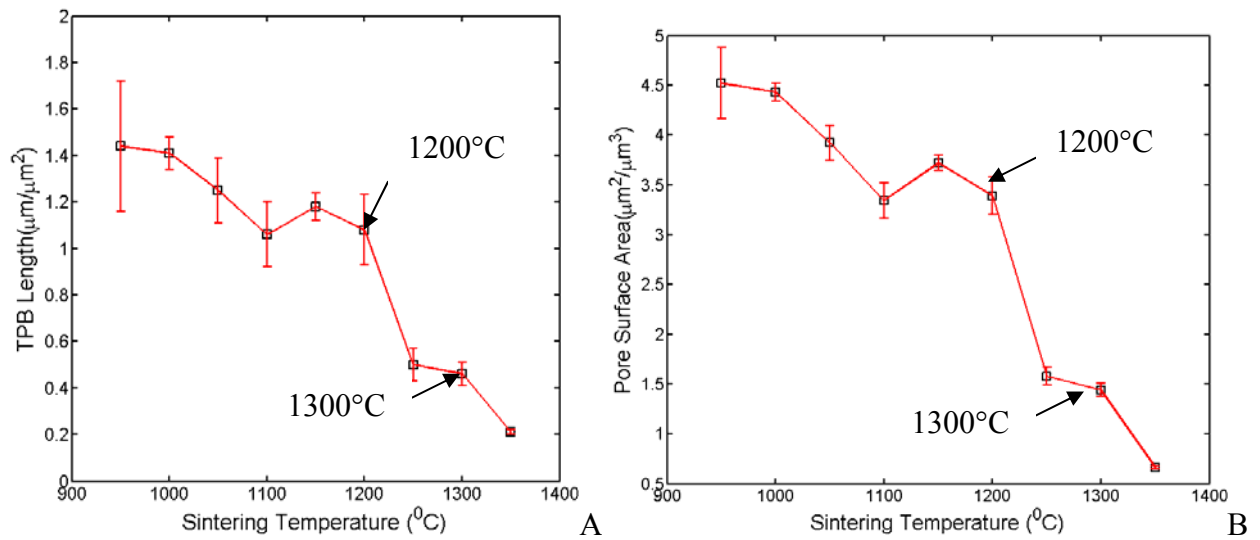


Figure 4-4. Metric properties of the isochronal sintered samples. A) TPB length of the isochronal sintered sample. B) Pore surface area of the isochronal sintered sample.

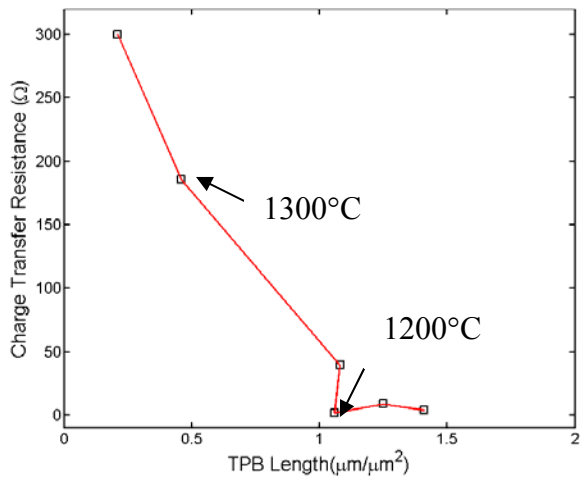


Figure 4-5. Dependence of the charge transfer resistance on the triple-phase-boundary length

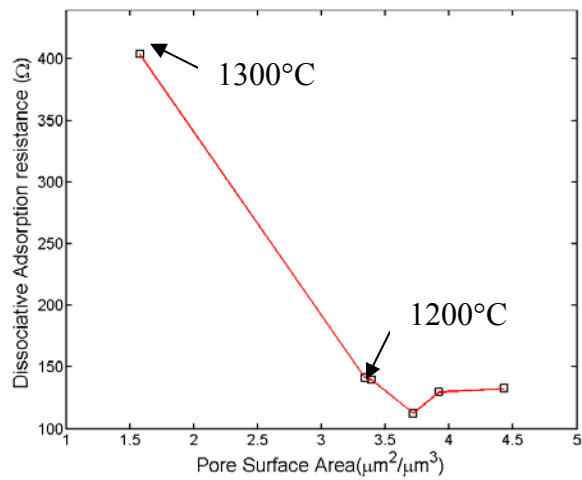


Figure 4-6. Dependence of the dissociative adsorption resistance on pore surface area of the isochronal one hour sintered samples

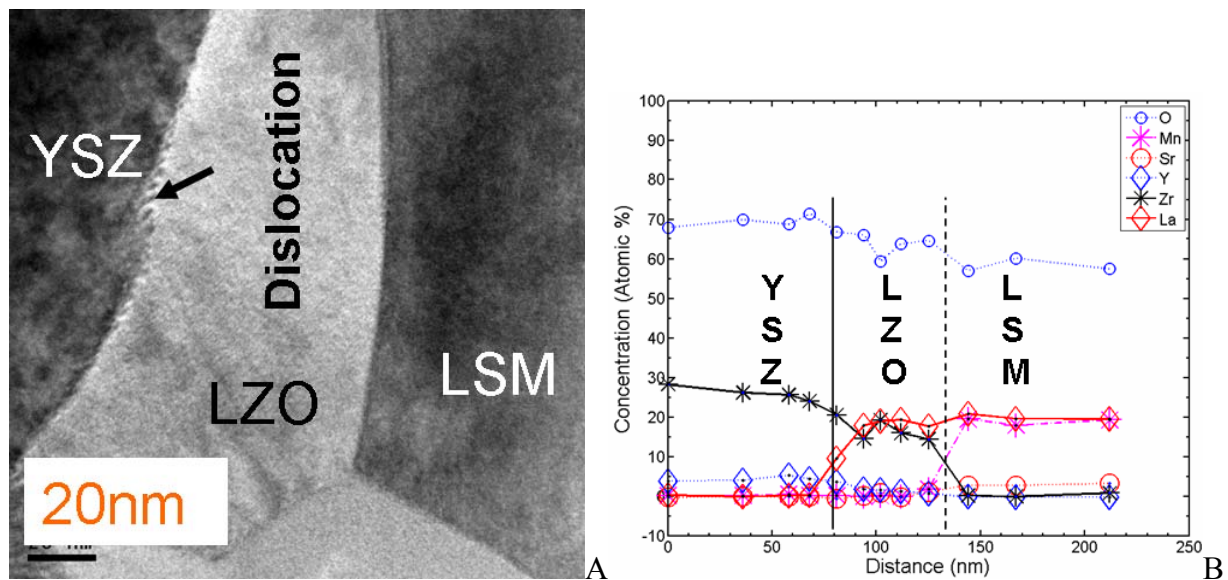


Figure 4-7. LSM/YSZ interface after 1200°C one hour sintering. A) HRTEM image. B) STEM-EDS analysis.

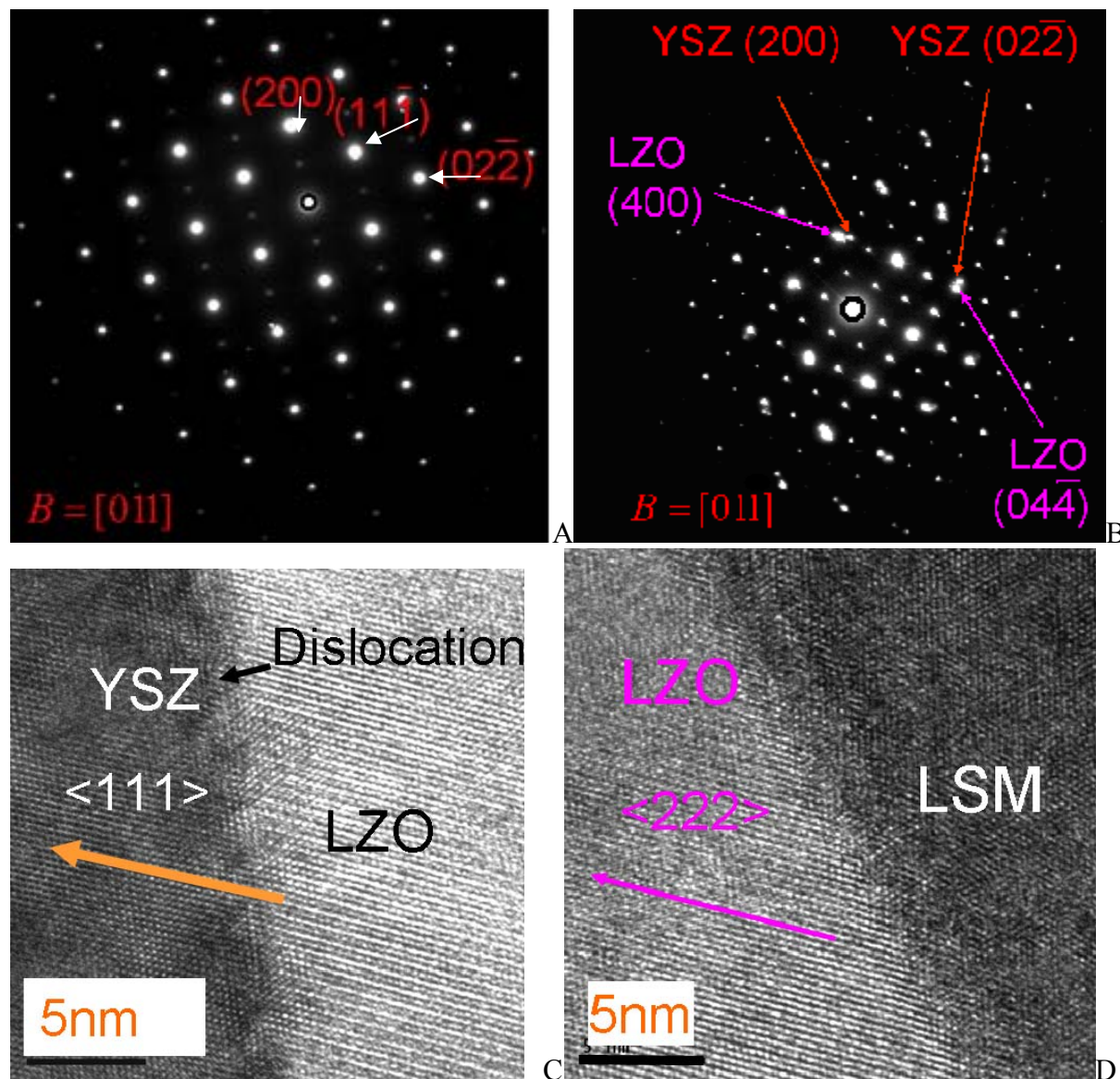


Figure 4-8. YSZ/LZO interface and LZO/LSM interface. A) Diffraction pattern of YSZ from the bulk for 1200°C one hour sintering. B) Diffraction pattern of LZO/YSZ interface for 1200°C one hour sintering. C) Lattice image of YSZ/LZO interface for 1200°C one hour sintering. D) Lattice image of LZO/LSM interface for 1200°C one hour sintering. (Note lack of epitaxial relationship).

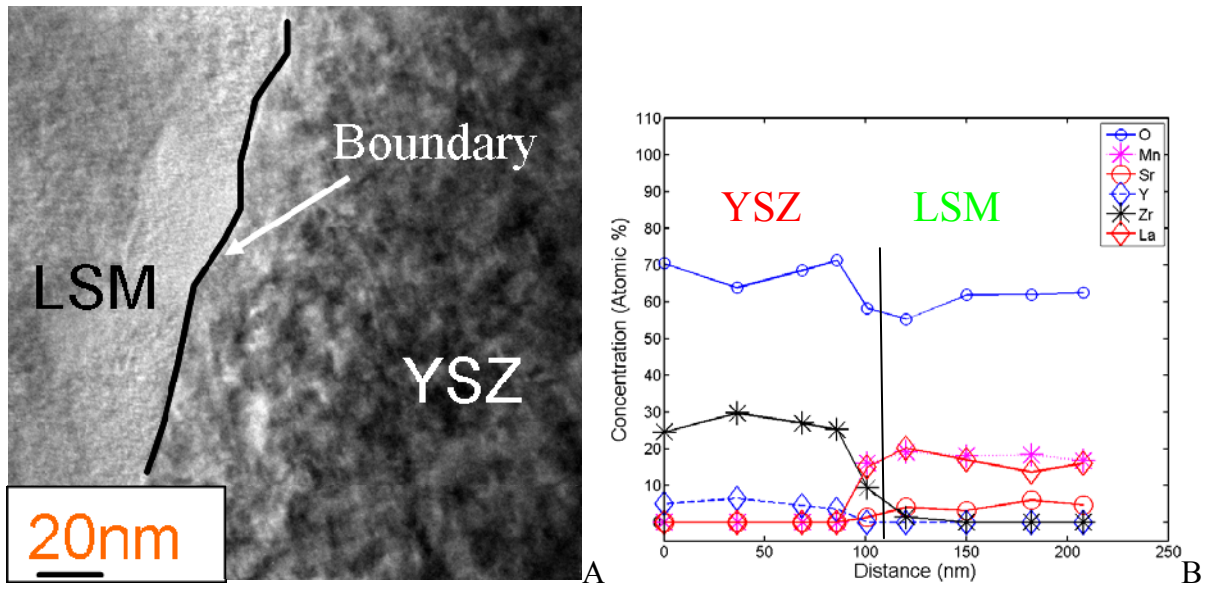


Figure 4-9. LSM/YSZ interface after 1100°C one hour sintering. A) HRTEM image. B) SETM-EDS analysis

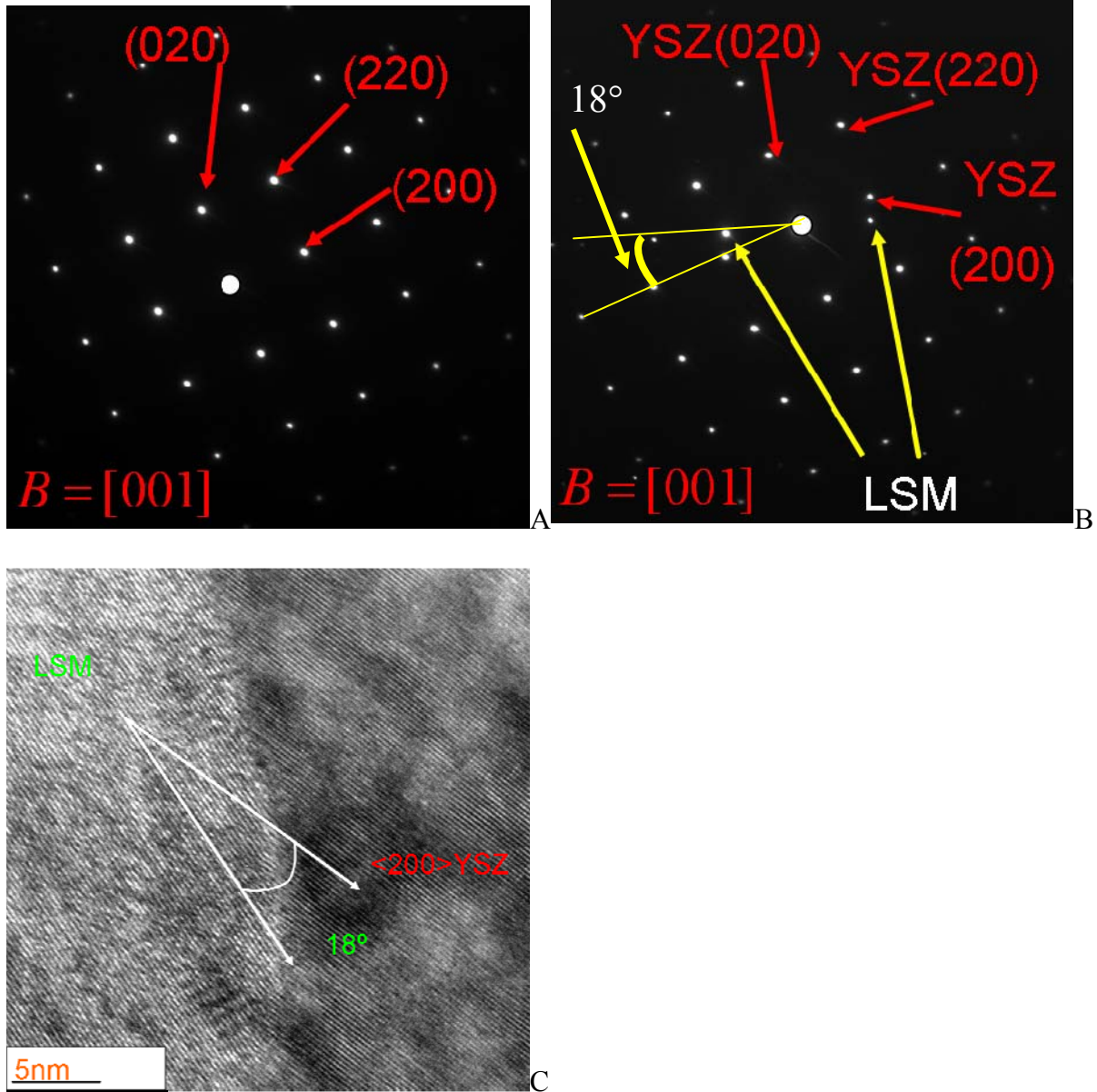


Figure 4-10. YSZ//LSM interface for 1100°C one hour sintering. A) Diffraction pattern of YSZ from the bulk. B) Diffraction pattern of LSM/YSZ interface. C) Lattice image of YSZ/LSM interface. (Note 18° between the LSM and YSZ both in B and C)

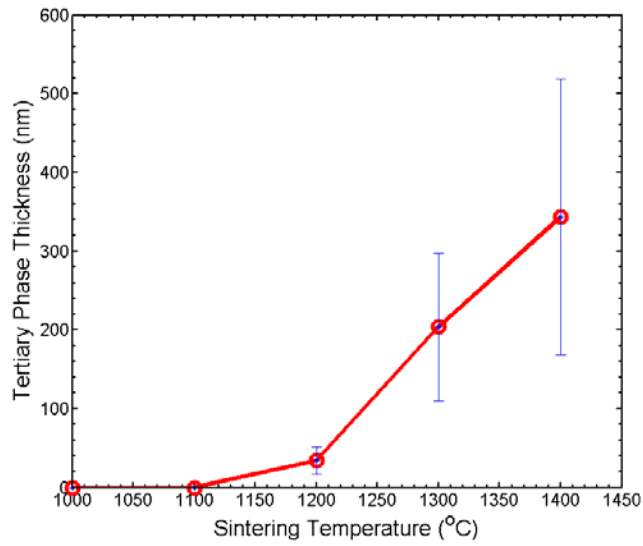


Figure 4-11. LZO thickness of one hour sintering at different temperatures

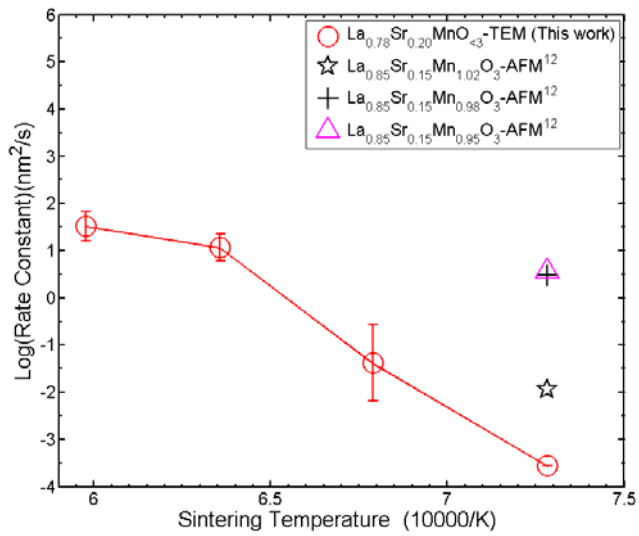


Figure 4-12. Comparison of rate constants of the LZO formation based on: TEM-circle; AFM-cross, star and triangle [6].

CHAPTER 5 ISOTHERMAL SINTERING STUDY

In this chapter, developed FIB techniques are applied to extend the findings in chapters 3 and 4 in order to clarify the relationship between the microstructure properties and the cathode polarization. Furthermore, this chapter will study the tertiary phase growth kinetics to explain the degradation of the cathode polarization that has been observed during the isochronal sintering study (see the previous chapter).

Isothermal sintering was performed at various times between 2h and 25h at 1200°C. This set of sintering samples was focused on: 1) the impact of the metric properties of the cathode microstructure on charge transfer resistance in section 5.1; 2) the kinetics of the LZO growth at the LSM/YSZ interface and the impact of the LZO phase formation between the LSM and the YSZ on the total ohmic polarization of the SOFC. How LZO growth and L_{TPB} affect the charge transfer reaction will be addressed in the isothermal study (see section 5.2); 3) the role of topology on cathode concentration polarization in section 5.3. Therefore, the manner in which these parameters impact all components of the cathode polarization will be discussed.

5.1 Effect of Metric Properties on Activation Polarization

5.1.1 Literature Review

Previous work reported that interfacial reactions kinetics and geometric properties dominate SOFC performance. There have been many studies on the impact of the geometry of the cathode, electrolyte and the cathode/electrolyte interface on the interfacial reaction resistance (R_p) [4, 107, 110, 125]. Many researches suggested that the interfacial reaction resistance depends on the diffusion paths for oxygen through the cathode material as well as on the triple phase boundary [3, 4, 126, 127]. In terms of which diffusion path of oxygen reactants take, the electrode is defined as surface-diffusion and bulk-diffusion types.

In the surface diffusion electrode, if the electroactive species are supplied to the reaction zones by surface diffusion, then the interfacial impedance (R_p) is inversely proportional to the L_{TPB} [4, 105, 107, 110, 128]. Mizusaki et al. assumed that adsorption of oxygen gas and dissociative adsorption occur at the YSZ/pore interface followed by the surface diffusion of dissociated oxygen atom (Figure 5-1 P1). Occurring at the TPB site, charge transfer reaction is not the rate-limiting-step. The electrolyte resistance was studied by Fabry and Kleitz's groups as well. The electrolyte resistance is a linear function of the reciprocal of the averaged interface radius for a point electrode [129, 130], the averaged interface radius was defined as a function of L_{TPB} . It is questionable that L_{TPB} is the only factor. Steele et al. concluded that the interfacial resistance is inversely proportional to a surface diffusion area of dissociated oxygen atom (O_{ad}) along the LSM/pore interface toward the TPB, the product of the L_{TPB} and the collection length (l_c) [109, 125]. The collection length represents the vertical diffusion distance of the dissociated oxygen atom (O_{ad}) from the touching point on cathode/pore interface to the TPB [125] (Figure 5-1). A second reaction path is come up with, adsorption of oxygen gas and dissociative adsorption occur not at the YSZ/pore interface but at the LSM/pore interface (Figure 5-1 P2). A dissociative oxygen adsorption step might be the rate-limiting-step [125]. In addition, R_p (the interfacial resistance) is affected by the oxygen molar volume in the perovskite (V_{lsm,O_2}) and surface exchange coefficient (β) at the TPB as following:

$$R_p = \frac{RT}{z^2 F^2} \frac{V_{lsm,O_2}}{\beta} \frac{1}{L_{TPB} l_c} \quad [5-1]$$

In the internal diffusion electrodes, oxygen is supplied to the electrode interface by bulk diffusion through the electrode material. In this case, the interfacial potential resistance was found to be proportional to $L_{TPB}^{-1.3}$ [106, 111]. Assuming LSM as a mixed electronic and ionic

conducting cathode, Kuznecov applied a bulk-diffusion controlled oxygen reduction model, which was developed by Adler [110], and concluded that the interfacial resistance (R_p) is affected by TPB length as well as contact area between the cathode and the electrolyte. Kuznecov assumes that the oxygen transport at the $\text{La}_{0.8}\text{Sr}_{0.2}\text{MnO}_3/\text{YSZ}$ interface is controlled by bulk diffusion of oxygen vacancies [107]. The relationship is written as $R_p \sim (S_c L_{TPB})^{-\frac{1}{2}}$ derived from equation 4-2. A third reaction path was assumed. Whole oxygen reduction occurs at the same place, the mixed conducting cathode/pore interface, oxygen ion conducts through cathode bulk into the YSZ (Figure 5-1 P3). It is a special case that LSM materials function as a ionic conductor. Ionic conductivity of the LSM could not be negligible when the operational atmosphere changes between oxidizing and reducing conditions. Adler et al. pointed out that the polarization resistance depends not only on the microstructure (L_{TPB} , S_c and V_V), but also on the electrocatalytical properties of the cathode material: ionic conductivity (σ_i), chemical diffusion coefficient of oxygen vacancies ($D_{V_o^{**}}$) and surface exchange coefficient (β) etc. as following [110]:

$$R_p = \frac{1}{(1-V_V)\sigma_i} \left(\frac{S_c}{L_{TPB}\beta} D_{V_o^{**}} \right)^{\frac{1}{2}} \quad [5-2]$$

where contact area is approximate to be surface fraction of the cathode grains in the LSM/YSZ interface, defined by $S_c \sim (1-V_V)$. The average time of the oxygen vacancy transferring into the

electrolyte is defined as $\tau_0 = \frac{S_c}{L_{TPB}\beta}$, and the collection length represents the surface diffusion distance of the oxygen vacancies in Kuznecov's model, and $l_c = (D_{V_o^{**}}\tau_0)^{1/2}$. The surface

diffusion distance of the dissociated oxygen atom is also equal to the collection length [125].

Finally, Equation 5-2 can be simplified as:

$$R_p = \frac{l_c^{1/4}}{S_c \sigma_i} \quad [5-3]$$

If collection length is not introduced in this equation, then Equation 5-2 can be expressed as

$$R_p = \frac{1}{(S_c L_{TPB})^{1/2} \sigma_i} \left[\left(\frac{D_{V_o}}{\beta} \right)^{1/2} \right] \quad [5-4]$$

It is noted that these models question that L_{TPB} is the only geometric factor. If all models had considered a condition under which the interfacial reaction is blocked by a tertiary phase, then these models predicted reliable relationships between the R_p and the L_{TPB} . It is well-known that LSM reacts with YSZ to form a deleterious tertiary phase at the LSM/YSZ interface at the normal operating temperature of 1000 °C [93]. In order to reduce the interfacial resistance, it is more credible to investigate the contribution of the interfacial microstructure to the kinetics of the dominant reaction step. At least resistance of three processes (charge transfer of oxygen ions at the cathode/electrolyte interface, dissociation of adsorbed oxygen molecules and diffusion of oxygen species to the cathode/electrolyte interface) contribute to the overall resistance, when the $La_{0.85}Sr_{0.15}MnO_3$ cathodes were sintered at 1300°C [131, 132]. It also was confirmed by EIP characterization of the $La_{0.78}Sr_{0.20}MnO_{<3}$ cathodes in the isochronal sintering study [89].

5.1.2 Experimental Design

Symmetric SOFC samples were prepared by screen-printing process (see section 4.1.3). This set of eight isothermal samples was sintered at 1200°C from 2h to 25h. The resulting cathode thickness is about 43µm and YSZ thickness is about 180µm. Cross-section image stacks were collected in the same way as described in section 4.1.3. L_{TPB} and S_V were quantified by applying the same relationship of the classical stereology (section 4.1.3). Open porosity was

quantified using the area probe on ~100 FIB/SEM images. Area probe assumes that open porosity (V_v) is numerically equal to the area fraction of open pores (A_A). The contact area between the LSM and YSZ (S_c) was calculated as a function of the area fraction of open pores. $S_c = A(1 - V_v)$, where A is determined by the screen-print process. Charge transfer resistance and dissociative adsorption resistance were obtained using electrochemical impedance spectroscopy [89] based on Nyquist plot (see Appendix B Figure B-3) and Bode plot (see Appendix B Figure B-4).

5.1.3 Results and Discussion

Cross-section FIB/SEM images are shown in Figure 5-2 for samples sintered at 1200°C from two hours to twenty-five hours. Figure 5-2a shows the cross-section images of the isothermally sintered samples from two hours to eight hours, the highlighted part represents contact region between the cathode and the electrolyte. It appears that the contact area between the LSM grains and the YSZ was changed by two competitive mechanisms (neck growth of LSM grains and pores growth) at the LSM/YSZ interface. Neck growth of LSM grains causes face to face contact, whereas, point to point contact increases by pore growth. At the early sintering process (less than 8 h), contacts among LSM grains and between LSM and YSZ increase, point to point contact changes into face to face contact. Figure 5-2b shows that after sintering for 8h, coarsening of the LSM grains competes over the growth of the continuous pore channel, LSM grains densify. Figure 5-3a and Figure 5-3b show changes in the contact area and changes in TPB length as a function of the sintering time. Figure 5-3a shows that the contact area between the LSM and YSZ increases as the sintering time increases. Increasing contact area arises from changes in contact between the LSM and the YSZ from point to point contact to face to face contact. Pore growth intends to reduce contact area as the sintering time is increased up to

8h, whereas, grain growth becomes dominant and intends to increase contact area. As a result, contact area increases. The TPB length is initially increased to the maximum ($0.9\mu\text{m}/\mu\text{m}^2$) and then decreased to the minimum ($0.4\mu\text{m}/\mu\text{m}^2$) as the sintering time increases (Figure 5-3b). It is consistent with changes in TPB length in the samples sintered at 1100°C from 10min to 10^3 min based on AFM measurement [6].

Variation of the TPB length is contributed to changes in effective contact area between the LSM grains and the YSZ. After sintering less than 8h, contact between LSM grains and YSZ increases by grain neck growth, at the same time, continuous pore channels are present at the LSM/YSZ interface. Thus, increasing face to face contact increases effective contact area, subsequently, increases TPB length. After sintering for 8h, formation of the closed pore channels decreases the effective contact area between the LSM grains and the YSZ. As a result, TPB length is dramatically reduced whereas contact area is increased. Two mechanisms of the interfacial microstructure evolution affect the TPB length.

Nyquist plot is shown in Appendix B Figure B-3. At the high frequency in the Nyquist plot, a slope of the 45° line was observed. Peak frequency from the right to the left in the Bode plot (see Appendix B Figure B-4 1200°C 8h) are $\sim 10^4$ Hz (high frequency intercept), ~ 10 Hz (middle peak) and ~ 0.1 Hz (low frequency intercept). As the sintering time increases, two semicircles/peaks are combined into one ~ 1 Hz (1200°C 25h). Interfacial resistance (the math difference between the high-frequency and the low-frequency intercept in the Nyquist plot) as a function of the square root of the sintering time is shown in Appendix B Figure B-5.

The comparison of the interfacial resistance to the TPB, collection length and contact area is shown in Figure 5-3c, Figure 5-3d and Figure 5-3e. The interfacial resistance as a function of the sintering time is shown in Appendix B Figure B-5. It increases from 187 to $565\ \Omega$. Figure 5-

3c shows that the decrease of L_{TPB} increases the interfacial resistance (R_p), R_p and TPB length do follow the trend ($R_p \sim L_{\text{TPB}}^{-1}$). In Mizusaki's impedance data, one depressed semicircle was observed. It arises from the charge transfer process with a peak frequency of $\sim 10^4$ Hz. This relationship was discussed by many groups [105-111]. The deviation (at the shortest sintering time) from the straight line will be explained as the effect of the TPB length on the charge transfer resistance will be discussed (see page 123).

The interfacial resistance increases as the surface diffusion area (the product of the L_{TPB} and l_c) decreases (Figure 5-3d). The interfacial resistance follows the prediction of the Steele's model after sintering up to 8h. However, at the sintering time less than 8h, data points are more scattered comparing with the Mizusaki's model. One reason arises from the introduction of the collection length, which represents the diffusion distance of the oxygen intermediates (oxygen vacancy or oxygen dissociative species) in the cathode to the TPB. In other words, a distance over which oxygen intermediates must be collected to maintain a specified current density at the TPB. Another reason arises from the assumption of the Steele's model, the mass transfer process is not rate-limiting-step. Nyquist plot shows apparent mass-transfer process, which contributes to a slope of 45° on the left side of the semicircle.

The interfacial resistance increases as the product of the L_{TPB} and S_c decreases (Figure 5-3e). Not all data points follow a power dependence of -0.5 of the interfacial resistance on the product of the L_{TPB} and S_c [107]. Kuznecov's model gives the worst fit with the isothermal sintering sample comparing to Mizusaki's and Steele's models. Deviation of the isothermal sintering data from the Kuznecov's model might be contributed to different interfacial reaction mechanisms under different sintering stages and the various ionic conductivity of the LSM. In the Kuznecov's impedance data, one semicircle with a peak frequency of ~ 2 Hz was observed

after sintering for 5h at 1300 °C. It indicates that the microstructure was in the late densification process. However, the isothermal sintering microstructure was in the early densification process. In the Kuznecov's model, LSM was increased its ionic conductivity by three orders of magnitude by mixing with the YSZ powders. YSZ has the ionic conductivity of 0.1 Scm^{-1} [29]. In the isothermal sintering samples, the regular LSM was used, LSM has an ionic conductivity of 10^{-7} - 10^{-6} Scm^{-1} [107]. It should be noted that LSM electrodes do not generally exhibit behavior consistent with the bulk diffusion model, since LSM is a poor ionic conductor [110]. It is consistent with the electrochemical impedance study described in Smith's paper [89]. The controversy between the isothermal sintering study and the Kuznecov's model might arise from the changes in contact area as well.

Three models that were discussed above predicted that the total interfacial resistance at the TPB, however, charge transfer resistance as a function of the sintering time is shown in Appendix B Figure B-6. It corresponds to the process with the peak frequency of $\sim 10^4 \text{ Hz}$ in the Bode plot [89], which is consistent with the Mizusaki's data. It increases from 3 to 9 Ω . The comparison of the charge transfer resistance to the TPB, collection length and contact area is shown in Figure 5-3f, Figure 5-3g and Figure 5-3h. The decrease of TPB length increases the charge transfer resistance. There does remain a linear relationship between the $1/L_{\text{TPB}}$ and the charge transfer resistance. The linear fit indicates that charge transfer resistance is $\sim 0 \Omega$ when L_{TPB} goes to infinite. In ideal case, charge transfer resistance should be close to zero because infinite L_{TPB} means that number of the reaction sites is sufficient for the charge transfer reaction. The inconsistency with Mizusaki's result ($R_{\text{P}} \sim L_{\text{TPB}}^{-1}$) at the shortest sintering time is ascribed to the sintering microstructure. Mizusaki et al. calculated TPB length at the LSM/YSZ interface contacted by face to face contact. TPB length will be larger with face to face contact than with

point to point contact. Therefore, the actual point $1/L_{\text{TPB}}$ is smaller than the first point predicted by the model (Figure 5-3f). In addition, limited amount of SEM images was applied to calculate TPB length. The homogeneity study of the microstructure has showed that the sintered LSM microstructure has some extent of nonhomogeneity (see section 3.3 in details). Therefore, TPB length in Mizusaki's study might only represents local metric property of the cathode microstructure. The charge transfer resistance is inversely proportional to the L_{TPB}^{-1} instead of the $L_{\text{TPB}}^{-1.3}$, which was observed by Kleitz et al., who assume the bulk-diffusion controlled mechanism, which will be discussed as Kuznecov's model is discussed.

The charge transfer resistance increases as the surface diffusion area of the oxygen intermediates (the product of the L_{TPB} and l_c) decreases (Figure 5-3g). The charge transfer resistance follows the prediction of the Steele's model. When the surface diffusion area goes to infinite, the charge transfer resistance is $\sim 1.6 \Omega$. It appears that the charge transfer resistance is affected by the collection length, the critical diffusion distance of the oxygen intermediates in the cathode to the TPB sites, over which the sufficient current density at the TPB is maintained. Steele et al. concluded that the dissociative adsorption reaction is the possible rate-limiting step. The impedance plots for this set of samples (see Appendix B Figure B-3 and Figure B-4) suggest that peak magnitude of the dissociative adsorption process ($\sim 10\text{Hz}$ in 1200°C 8h profile) increases as the sintering time increases. As the dissociative adsorption resistance increases, the supply rate of the oxygen intermediate in the cathode to the TPB site is slowed down, as a result, the charge transfer resistance increases as the oxygen intermediate is one of reactants of the charge transfer reaction. It seems that Mizusaki's model (Figure 5-3f) fits the isothermal sintering data better than the Steele's model (Figure 5-3g). This can be related to the effect of a tertiary phase formed at the LSM/YSZ interface on the collection length. If the tertiary phase

covers the diffusion distance of the oxygen intermediates to the TPB, the sufficient current density at the TPB should be maintained by adjusting the experimental collection length. In addition, as the collection length increases, diffusion of the oxygen intermediates in the cathode to the TPB site causes a resistance term in the charge transfer reaction, as a result, the intercept of the charge transfer resistance is larger than zero as the product of the L_{TPB} and I_c goes to infinite large.

The charge transfer resistance increases as the product of the L_{TPB} and S_c decreases (Figure 5-3h). A power dependence of -0.5 of the charge transfer resistance on the product of the L_{TPB} and S_c [107] was observed in the isothermal sintering study. It suggests that the charge transfer resistance depends on contact area between LSM and YSZ as well as TPB length. Contact area between the LSM and the YSZ as well as TPB length both affect the area of the chemical reactive zone for the charge transfer reaction [110]. It appears that the manner in which charge transfer resistance is affected by both L_{TPB} and S_c is similar to the manner in which charge transfer resistance is affected by the L_{TPB} (Figure 5-3h and Figure 5-3f). This model predicts that charge transfer resistance is $\sim 8 \Omega$ when L_{TPB} and S_c go to infinite large. It is different from Mizusaki's prediction with the infinite large of the L_{TPB} . In reality, charge transfer resistance should be close to zero if the chemical reaction zone of the charge transfer reaction goes to infinite. Kuznecov's and Kleitz's models assumed that the oxygen reduction mechanism is controlled by the bulk diffusion mechanism. The controversy between my study and two models suggests that the bulk-diffusion model is not applicable to explain the relationship between the activation polarization and the metric properties in this material [89, 110].

Varying diffusion paths for oxygen through the cathode material changes the effect of the triple phase boundary on the interfacial reaction resistance [3, 4, 126, 127]. In addition, the

interfacial reaction has an unstable nature. The variations in the dependence of the individual interfacial reaction resistance on the L_{TPB} have been reported by Suzuki et al. and Sasaki et al.. These changes occur because the dominant rate limiting step shifts from the dissociative adsorption and the charge transfer to the oxygen diffusion in micropores [133, 134]. The last but not the least, capability of quantification of the TPB length [4, 129, 130] is compromised by locally taking SEM images. Limited SEM images were taken from a local region of the whole sample. The L_{TPB} is not the same at different parts of the sintered sample as homogeneity study suggests (see section 3.3).

Dissociative adsorption resistance as a function of the sintering time is shown in Appendix B Figure B-7. It increases from 125Ω to 521Ω as the sintering time increases. Figure 5-4 shows that pore surface area affects the dissociative adsorption resistance. Dissociative adsorption resistance was increased from 125Ω to 184Ω as the pore surface area decreased by $0.2 \mu\text{m}^2/\mu\text{m}^3$. The dissociative adsorption resistance was dramatically decreased by two times as the pore surface area slightly increases by $0.2\mu\text{m}^2/\mu\text{m}^3$. This occurs after sintering for 8h. This can be explained by the fact that the growth of pores results in the decreasing of the pore surface area. Pore area determines the area exposed for dissociative adsorption of oxygen and therefore affects the cathode activation polarization. Change in the increasing rate of the resistance varies from the early sintering process to the late sintering process, this variation is consistent with the changes in the LSM microstructure of the isothermal sintering samples.

5.1.4 Conclusions

The relationship between the activation polarization and the metric properties was studied under surface-diffusion and bulk-diffusion controlled mechanisms. How the interfacial resistance was affected by TPB length, collection length and contact area was discussed. It was found that

the bulk-diffusion controlled mechanism gave the worst fit. It arises from the cathode fabrication.

It was found that charge transfer resistance was increased from 3Ω to 9Ω as the L_{TPB} decreased from $0.92 \mu\text{m}/\mu\text{m}^2$ to $0.46 \mu\text{m}/\mu\text{m}^2$. Charge transfer resistance increases because effective active sites for charge transfer reaction are dramatically reduced. This relationship was observed between this work and previous studies. In Mizusaki's model, the experimental data matches with the predicted data. Mizusaki's model gave reasonable estimation because charge transfer resistance is close to zero as the TPB length goes to infinite large. It was found that charge transfer resistance was increased from 3Ω to 9Ω as the surface diffusion area decreased from $0.11 \mu\text{m}^2/\mu\text{m}^2$ to $0.28 \mu\text{m}^2/\mu\text{m}^2$. The charge transfer resistance followed the prediction of the Steele's model. It might suggest that the charge transfer resistance is affected by the collection length, the critical diffusion distance of the oxygen intermediate to the TPB site. Steele's model predicted different collection length from the experimental data and positive charge transfer resistance with the infinite surface diffusion area. It might be related to the impact of the tertiary phase on the diffusion distance. These models based on surface-diffusion controlled mechanism appeared match with the experimental data. Small deviation contributed to the change in contacts of the LSM/YSZ interface from face to face contact to point to point contact upon sintering. The biased quantification of the TPB length might cause the scattered data. Quantification of the TPB length on a local region contributed to the inconsistency of the Mizusaki's result with my study.

5.2 Tertiary Phase Growth Kinetics

5.2.1 Literature Review

Consistent with previous studies in the literature, the isochronal sintering study supports that the tertiary phase dramatically degrades the performance of the cathode by abruptly increasing activation polarization. Since the deleterious effect of the LZO phase could not be neglected, focus of many research has been on how electrochemical resistances are influenced by formation of the LZO phase in A-site stoichiometric or A-site deficient LSM/YSZ based on EIS analysis [98-101, 127, 135-138]. EIS is effective to detect the blocking responses from different microstructure defects located at the LSM/YSZ interface [139, 140]. These microstructure defects formed at the LSM/YSZ interface include the isolating LZO phase. In previous studies, the electrochemical polarization due to the LZO phase formation was characterized by analyzing modification of the shape of the EIS impedance diagram [141]. LZO phase blocks interfacial reactions thus slowing down the interfacial reaction rate and changing the interfacial resistance and. Changes in the magnitude of the interfacial resistance and in the kinetics of the interfacial reactions influence the shape of the EIS diagram and the location of the intercepts with the real axis.

EIS studies have showed that the growth of the insulating phases at the LSM/YSZ interface has impacts on cathode electrochemical properties [127, 130, 135, 136, 138]. Brant et al. reported that the deleterious LZO phase was detected at the LSM/YSZ interface in samples sintered higher than 1200°C [130]. LZO starts to degrade the cathode electrochemical properties [97-101, 130] after the sample is sintered at 1200°C for 100h [130]. In Brant's paper, three intercepts at the high, middle and low frequency ranges with the real axis in the Nyquist plot were emphasized. The high-frequency ($1.3\text{-}5 \times 10^7$ Hz) intercept with the real axis represents the electrolyte impedance response. The middle-frequency intercept with the real axis is the

resistance that is contributed to the isolating LZO phase or other microstructure defects formed at the LSM/YSZ interface. In other words, the middle-frequency intercept with the real axis represents the blocking effect of the interfacial defects on the interfacial reaction. The low-frequency intercept with the real axis is the electrode impedance. The total polarization (R_t) is the mathematical difference between the low-frequency intercept with the real axis and the low-frequency intercept of the middle-frequency arc with the real axis in the Nyquist plot (Figure 5-5). The interfacial resistance (R_p) was determined from the difference between the high-frequency intercept with the real axis and the low-frequency intercept of the middle-frequency blocking resistance [130] (Figure 5-5). EIS result suggests that the middle-frequency blocking resistance changes the interfacial resistance. The interfacial resistance increases as the sintering time is increased. The interesting result of Brant et al is that the interface resistance shows the square root of dependence on the sintering time. If this result had been related to the microstructure characterization of the LZO growth on the atomic scale, then how basic physical mechanisms dominates the interface reactions therefore affects the interfacial resistance would be understood. These EIS studies have been devoted to the interfacial electrochemical properties or polarization effects, however, EIS could not provide structural information of the LZO phase formation. It is still not clear whether the interfacial resistance characterized by EIS represents the blocking effect of the LZO phase on the conduction and diffusion mechanisms on the atomic scale.

A few HRTEM studies were performed to collect structural information of the LZO formation. Mitterdorfer et al. provided complete structural information of the LZO nucleation using HRTEM, atomic force microscopy (AFM) and EIS [6], which were summarized in Chapter 4. Of particular interest is the comprehensive analysis of the diffusion mechanisms of

cations, which control LZO formation at the A-site rich $\text{La}_{0.85}\text{Sr}_{0.15}\text{Mn}_{0.98}\text{O}_3/\text{YSZ}$ and at the A-site deficient $\text{La}_{0.85}\text{Sr}_{0.15}\text{Mn}_{1.02}\text{O}_3/\text{YSZ}$ interfaces. Mitterdorfer reports at the A-site rich $\text{La}_{0.85}\text{Sr}_{0.15}\text{Mn}_{0.98}\text{O}_3/\text{YSZ}$ interface, that the nucleation of the LZO cube-shaped islands is controlled by surface diffusion of Zr cations along side of the LZO island to the top of the LZO island. As soon as LZO layer becomes dense and fully covers the YSZ layer, growth of the LZO dense layer is limited by bulk diffusion of Zr^{4+} . The supply of oxygen electric species within the Nernst diffusion thickness is realized mainly by the surface diffusion process of atomic species [6]. The thickness of the Nernst diffusion layer (the effective thickness of the diffusion layer of the dissociated adsorbed oxygen electric specie near the TPB) is in the order of 50-150 nm at temperatures between 550°C and 1000°C.

Mitterdorfer suggests that LZO islands are formed in a distinct way at the A-site deficient $\text{La}_{0.85}\text{Sr}_{0.15}\text{Mn}_{1.02}\text{O}_3/\text{YSZ}$ interface. LZO nuclei at an early stage are formed by surface diffusion of cations. After that, LZO island growth at a late stage is controlled by surface diffusion of cations and the supply of lanthanum. LZO growth is controlled by the reductive decomposition of the LSM, which is the only way to supply La cations. LZO formation at the $\text{La}_{0.85}\text{Sr}_{0.15}\text{Mn}_{1.02}\text{O}_3/\text{YSZ}$ interface has been significantly retarded as compared to LZO formation at the $\text{La}_{0.85}\text{Sr}_{0.15}\text{Mn}_{0.98}\text{O}_3/\text{YSZ}$ interface, because the supply of La cations in the primer is insufficient for LZO formation. It has been proposed that LZO nucleation rate in A-site deficient $\text{La}_{0.85}\text{Sr}_{0.15}\text{Mn}_{1.02}\text{O}_3$ is about one or two orders of magnitude lower than that in A-site rich LSM/YSZ. However, Mitterdorfer et al. rather emphasized the kinetics of the LZO nucleation at A-site rich LSM/YSZ interface than the kinetics of the LZO growth at A-site deficient LSM/YSZ. Kinetics study of the LZO growth is crucial to understand degradation of the SOFC performance under the operating conditions.

To better understand the degradation of the SOFC electrochemical properties due to the LZO growth at the A-site deficient LSM/YSZ interface, it is necessary to study how LZO growth affects the interfacial chemical reaction kinetics. Therefore, the quantitative dependence of the resistance of the specific reaction in the oxygen reduction mechanism on the corresponding cathode microstructure parameters has to be identified. An understanding of how LZO growth influences quantitatively activation polarization and ohmic polarization in the A-site deficient LSM/YSZ needs to be developed. In other words, how LZO phase affects diffusion mechanism of the oxygen intermediates, thus increasing the activation polarization, and how it affects the ohmic polarization by affecting conduction mechanism of the oxygen reactants. There are many reports on measurements of the LZO electrical conductivity in the literature [30, 101, 123, 142-145], value of the LZO electrical conductivity ranges from 10^{-5} to $3 \times 10^{-3} \text{ Scm}^{-1}$. Most of measurements were performed by impedance spectroscopy [101, 123, 144, 145], however, geometric factors (contact area between the cathode and the electrolyte, and the thickness of the cathode) were simplified in these measurements. In my study, geometric factors are quantified based on FIB/SEM and TEM images.

Isothermal sintered samples at 1200°C from 2 h to 25 h are selected since LZO has been observed at such a high temperature for one hour sintering based on the isochronal sintering study. Chapter 4 addressed the different results between my study and previous TEM studies of the LZO formation in details. This section will expand the kinetics study of the LZO growth, and it will emphasize that LZO phase changes cathode activation and ohmic polarizations on the micron scale by interruption of conduction and diffusion mechanism of reactant species for the oxygen reduction on the atomic scale. In addition, the following section will address calculation of the LZO conductivity. The LZO ohmic resistance will be measured by impedance

spectroscopy (EIS), TEM, FIB/SEM and the classical stereology will provide geometric factors in calculation of the LZO conductivity.

5.2.2 Experimental Design

The isochronal sintering study provides basic knowledge of the LZO phase formation. The same kind of TEM analysis and rate constant calculation was applied (see Chapter 4) for seven samples in this isothermal sintering study. High-frequency intercepts of the impedance plot on the real impedance-axis in the Nyquist plot were extracted to calculate ohmic resistance of the LZO. The Ohm's law ($R = \rho \frac{l}{A}$), was applied to calculate the YSZ ohmic resistance and LSM ohmic resistance. l is the dimension parallel to the conduction direction, and A is the cross-section area, perpendicular to the conduction direction. The contact area (S_c) is defined as $A(1 - V_v)$ (see section 5.1.2) and was used to calculate LSM ohmic resistance. LZO thickness was taken into account to understand the blocking effect of the LZO on the impedance of the sample. The surface diffusion area, which is blocked by LZO phase, is equal to the product of the LZO thickness and TPB length. The magnitude of the LZO thickness (30-80nm) in my study is comparable to the thickness of the Nernst diffusion layer discussed in Mitterdorfer's paper. The LZO thickness represents the diffusion distance of the oxygen electric and ionic species through the isolating LZO phase [6]. The blocked volume between the LSM grains and the YSZ surface was calculated by multiplying blocked contact area and LZO thickness. The blocked contact area is the contact area between the LSM grains and YSZ because LZO phase covers the contact area between the YSZ surface and the LSM grains. Mitterdorfer reports that LZO islands covers 90% of the YSZ surface after sintering for 12h and sintering at 1100°C. These samples have the A-site to the B-site ratio of 1:0.98. In my study, samples have A-site to the B-site ratio of 1:1.02. Rate constant of the LZO phase in my study is three orders of magnitude lower than that of LZO

phase formation in Mitterdorfer's paper. TEM study shows that LZO phase covers the interface region between the LSM grains and the YSZ surface. Therefore, blocked contact area by LZO phase is assumed to be the initial contact area between the LSM grains and the YSZ surface.

The ohmic contribution of the LZO phase (R) to the overall ohmic resistance was related to geometric factors (LZO thickness and TPB length) as a function of sintering time. The normalized LZO resistivity ($\rho_{o,LZO}$) is the product of the LZO ohmic resistance and the LZO thickness for simplification. In order to study the interruption of the oxygen ion conduction by LZO formation, half of the slope of the LZO ohmic resistance vs the quotient of the LZO thickness by the effective contact area is defined as the LZO electrical resistivity (ρ_{LZO}).

$$\rho_{LZO} = R_{LZO} \frac{1}{t_{LZO} / S_C} \quad [5-5]$$

5.2.3 Results and Discussion

5.2.3.1 Epitaxial relationship

LZO phase formation was characterized by STEM-EDS diffusion profiles, diffraction patterns and lattice images at interfaces for the isothermally sintered samples (see description in Chapter 4). Diffraction patterns and lattice images taken at the YSZ/LZO interface confirm that LZO shows the epitaxial relationship to the YSZ not to the LSM in the isochronal sintering study (see section 4.2). The epitaxial relationship was observed in diffraction patterns of all samples sintered at 1200°C. Figure 5-6 demonstrates the epitaxial relationships between the polycrystalline YSZ and the LZO, observed in two samples. Figure 5-6a shows that the epitaxial relationship was observed when the electron beam was parallel to the YSZ zone axis of [130] after the sample was sintered for 2h, and the same relationship was shown when the electron beam was parallel to the YSZ zone axis of [105] after the sample was sintered for 6h (Figure 5-

6b). Diffraction patterns taken at the YSZ/LZO interface suggest that this epitaxial relationship is independent on the different crystal orientations of the polycrystalline YSZ. One degree tilt was apparent in both Figure 5-6a and Figure 5-6b, tilt degree does not change as the sintering time increases. It does not change as a function of the sintering temperature (1473K-1673K for one hour sintering), and the sintering time (1h-25h at 1473K).

5.2.3.2 LZO growth kinetics

Figure 5-7a shows changes in the LZO thickness as a function of time, and Figure 5-7b compares LZO rate constants. It suggests that LZO thickness is increased from 38.2 ± 5.6 to 84 ± 4 nm by increasing the sintering time from 60 to 268s. A direct linear relationship was observed between the LZO thickness and the square root of the sintering time. The power dependence of the LZO thickness on the sintering time is two. It suggests that LZO growth is dominated by a diffusion-controlled mechanism [6]. This conclusion is consistent with the diffusion results of the STEM-EDS analysis at the LSM/YSZ interface in this work and other previous work [6, 7]. The diffusion of cations (La, and Mn) to the chemical reaction zone is the determining process for the formation of the LZO phase at the interface. In addition, the diffusion-controlled LZO growth might explain why the interface resistance measured by EIS shows the same dependence on the sintering time in Brant's paper [130]. If the interface resistance represents the blocking effect of the LZO phase instead of other microstructure defects at the LSM/YSZ interface, then the interface resistance should display characteristics of the LZO growth mechanism.

The power dependence of the LZO thickness on sintering time is two in the Mn-excess LSM. This dependence is smaller than an exponent of 2.48 in the Mn-deficient LSM reported by Mitterdorfer [6]. The rate constant of the LZO phase formation (see slope in Figure 5-7a) is

equal to $0.039\text{nm}^2/\text{s}$ in the 1200°C sintering study. It is at least one order of the magnitude lower than that of Mn-deficient LSM at 1100°C reported in Mitterdorfer's paper (Figure 5-7b). Mn in my study is at least 4 mol% excess than Mn-deficient LSM in Mitterdorfer's study. In addition, La in my study is $\sim 7\text{mol}\%$ less than La in the Mn-deficient LSM. The rate constant of the LZO formation at 1200°C is comparable to the result of Mitterdorfer at 1100°C . Both studies use LSM with the same A-site (La, Sr) to B-site (Mn) ratio, whereas there is $\sim 7\text{mol}\%$ less La in my study than La in the Mitterdorfer's study. The less La in the LSM, the smaller activity of La in the reaction of the LZO formation [34]. It is possible that the decrease in A-site to B-site ratio stabilizes the LSM thus retarding LSM decomposition. Mn inhibits decomposition of the LSM. The less LSM is decomposed, the less amount of the La is supplied to reactions between the LSM and the YSZ. As a result, LZO formation is delayed. Therefore, La deficiency and Mn excess delay the LZO formation [6].

LZO phase formed between the A-site deficient LSM and the YSZ is expected to affect electrochemical properties. At low-overpotential region, the insulating gap is expected to change the cathode diffusion mechanism or conduction mechanism [6, 28].

5.2.3.3 Contributions of LZO formation to activation polarization

In the early discussion, the amount of the LZO phase increases as the square root of the sintering time. The interfacial resistance shows a power dependence of two of the square root of the sintering time (see Appendix B Figure B-5). The effect of the LZO phase on the interfacial resistance is shown in Figure 5-7c. The increasing LZO thickness increases the interfacial resistance. It suggests that LZO phase blocks some electrode reactions, which include charge transfer reaction, dissociative adsorption reaction or surface diffusion of the oxygen intermediates, subsequently, interfacial resistance increases. It appears that the interfacial resistance follows a power dependence of two of the LZO thickness.

Impacts of the LZO phase on the interfacial resistance in previous three models are shown in Figure 5-7d, Figure 5-7e and Figure 5-7f. Figure 5-7d shows that increasing the ratio of the LZO thickness to the TPB length increases linearly the interfacial resistance. The experimental data matches better than the Mizusaki's model, in which deviation of the experimental data from the model was pointed out at the early stage of the isothermal sintering. Because the interfacial resistance in the Mizusaki's model was substituted by the charge transfer resistance. It appears that LZO blocks some TPB sites, in other words, effective TPB sites are reduced. Both LZO phase formation and reduction in the TPB length increase the interfacial resistance. After integrating impacts of the LZO phase, interfacial resistance shows a linear relationship than the predication of the Mizusaki's model.

The interfacial resistance increases as a function of the $t_{LZO}^2/(L_{TPB}l_c)$ as shown in Figure 5-7e, data points are not scattered at the early stages of the sintering, as what was observed in the Steele's model (Figure 5-3d). LZO phase is expected to block porosity, porosity of the LSM decreases as LZO phase is formed, as a result, interfacial resistance increases [107]. LZO phase affects the diffusion distance of the oxygen intermediates in the LSM to the TPB sites, collection length, has to be extended in order to maintain the sufficient current density at the TPB. Increasing the collection length increases the interfacial resistance [109].

Figure 5-7f shows that the interfacial resistance reduces by increasing the ratio of the LZO thickness and the product of the contact area and the TPB length. Scattered data at the early sintering process was absent, although it was apparent in the Kuznecov's model. It suggests that LZO phase causes the slow reaction rate of the interfacial reactions. The power dependence of the LZO thickness varies from 1.1 in the Mizusaki's 1-D model to 2 in the Steele's 2-D model (the surface-diffusion controlled mechanism) and then decreases to be 0.6 in the Kuznecov's 3-D

model (bulk-diffusion controlled mechanism). However, Steele's model assumes that the collection length is a constant. Collection length varies in this set of the isothermal sintering samples. Therefore, the power dependence of the LZO thickness is expected to be close to 1.1. The bulk-diffusion controlled mechanism is not applicable for the LSM system (see details in Section 5.1.3) [110], this corrected Kuznecov's model can be ruled out.

It should be noted that LZO phase changes the interfacial reaction by affecting TPB boundary. Since the charge transfer reaction is the reaction, which occurs directly at the TPB, it should be interesting to study the impact of the LZO phase on the charge transfer reaction. The effect of the LZO phase on the charge transfer resistance is shown in Figure 5-7g. The increasing LZO thickness increases charge transfer resistance. The charge transfer resistance is larger with the presence of the LZO phase than with the absence of the LZO phase. It indicates that LZO phase blocks the supply of the reactants (electrons or/and oxygen intermediates), and then slows down the charge transfer reaction, as a result, charge transfer resistance increases.

Section 5.1.3 showed that the TPB length is not only geometric factor to the charge transfer resistance (R_{CT}). If the effect of the TPB length on the charge transfer resistance is compared to the effect of LZO thickness, then it appears that the latter has the stronger effect. In other words, the charge transfer resistance increases as a function of a squared LZO thickness, whereas, the L_{TPB} shows a contribution of a single power. LZO phase aligns data points, which correspond to the large TPB length (Figure 5-7f). The large TPB length is caused by the early sintering process, during which the LZO nucleates at some TPB sites and grows laterally along the LSM/YSZ interface, the charge transfer resistance keeps increasing due to the gradual reduction in TPB sites. The qualification of the TPB length is offset from the real magnitude of the TPB length. Because the TPB boundary, in fact, is covered by LZO phase, this part of the

TPB boundary is invisible using SEM. After the LZO phase covers the whole LSM/YSZ interface, charge transfer reaction still occur at TPB sites, the quantification of the TPB length is not affected by the coverage of the TPB sites. As a result, small TPB length does not show deviation from the straight line. At this late sintering process, LZO layer grows parallel to the normal of the LSM/YSZ interface, as a result, LZO thickness increases, then charge transfer reaction slows down due to blocking the incorporation of the oxygen ion in the zirconia and inhibiting surface diffusion of the oxygen intermediate to TPB [6], as a result, the charge transfer resistance is increased by both increasing LZO thickness and reducing TPB length (Figure 5-7h). Because number of active sites for charge transfer reactions is reduced by increasing amount of LZO phase formed at the LSM/YSZ interface and by decreasing TPB length. Figure 5-7g shows a power dependence of two of the LZO thickness.

Applying relationships between the interfacial resistance and the TPB length in the previous models into the charge transfer resistance, the power dependence of the LZO thickness was 1.88 in Figure 5-7h, 2 in Figure 5-7i and 0.86 in Figure 5-7g. It should be noted that the interfacial resistance has different dominated electrode reactions. However, the t_{LZO}^2 or $t_{LZO}^{1.88}$ is consistent with the interfacial resistance as a function of the t_{LZO} , it represents the blocking effect of the LZO phase on supply of the surface diffusion of the oxygen reactant species for the charge transfer reaction from YSZ and or LSM to the TPB. It is possible that LZO phase affects the surface diffusion [6] or bulk diffusion mechanism of the oxygen reactant species [28].

In addition, the charge transfer resistance ($t_{LZO}=0$) is predicted to be 3 and 3.3 Ω , and is close to the experimental charge transfer resistance of 3.8 Ω , which was measured from one sample without LZO formation. LZO phase formed at the LSM/YSZ interface dramatically increases the energy barrier for the reactions to overcome by increasing charge transfer

resistance, thus the activation polarization increases. Therefore, charge transfer resistance is dominated by LZO phase formation. It appears that the study of the effect of TPB boundary on the charge transfer resistance should take the impact of the LZO phase into account.

5.2.3.4 Effect of LZO phase formation on ohmic polarization

Table 5-1 shows results of the ohmic polarizations (ohmic resistance) of the SOFC components and values of the geometric factors. Figure 5-8a and Figure 5-8b show changes in ohmic polarization of the LSM and ohmic polarization of the LZO as a function of the sintering time, respectively. The total ohmic resistance (high-frequency intercepts of the impedance plot on the real impedance-axis) consists of the YSZ ohmic resistance, the LSM ohmic resistance and the LZO ohmic resistance. YSZ is a fully dense material. Thickness of the YSZ layer (l) and cross-section area (A) are determined by the fabrication processing of tape casting. Conductivity of YSZ (σ_{YSZ})[29], A and l were used to calculate YSZ ohmic resistance using Ohm's law. The YSZ ohmic resistance ($\eta_{O,YSZ}$) is a constant of 0.07Ω although the sintering time increases.

Figure 5-8a shows that LSM ohmic resistance is not a constant, and it falls into a range of $4-6 \times 10^{-9}\Omega$. It is decreased as the sintering time increases. With the increasing sintering time, the contact area increases (Figure 5-3a). It should be noted that the cross-section area of the LSM in Ohm's law was normalized by the effective area fraction of LSM grains ($1-V_v$) at the cross-section area and the dimensionless connectivity among LSM grains (C_v), because Ohm's law states an ohmic loss for a dense and connected conducting material. LSM is porous so that pores and isolated LSM grains are not contributed to electron conduction within the cathode bulk. The effective cross-section area, A_{LSM} , should be the area of the connected LSM grains in the cathode bulk. A_{LSM} was calculated as the following equation:

$$A_{LSM} = A_{T_{LSM}} (1 - V_v) C_v \quad [5-6]$$

where A_{TLSM} is the total cross-section area of the screen-printed LSM layer and is determined by the screen-printing fabrication of the SOFC material. The product of the total cross-section area and area fraction of LSM grains is defined as the effective contact area (S_c) at the LSM/YSZ interface at the TPB (Figure 5-3a). S_c was calculated by

$$S_c = A_{TLSM} (1 - V_v) \quad [5-7]$$

Conductivity of the LSM (σ_{LSM}) [23] and LSM thickness (l) were used to calculate the ohmic resistance of the LSM. LSM thickness was measured from the cross-section FIB/SEM images.

LZO ohmic resistance (R_{LZO}) was calculated by subtracting YSZ and LSM ohmic resistance from the total ohmic resistance of the whole sample. Figure 5-8b shows that LZO ohmic resistance falls into the range of 3.67-6.43 Ω as the sintering time increases. Large LZO ohmic polarization is ascribed to much lower of electronic conductivity than LSM [23,27]. R_{LZO} can be defined as the following equation:

$$R_{LZO} = \rho_{LZO} \frac{t_{LZO}}{A_{LZO,TPB}} \quad [5-8]$$

where ρ_{LZO} is the LZO electrical resistivity and $A_{LZO,TPB}$ is the contact area of S_c , which is the LSM grain area at the LSM/YSZ interface (Figure 5-3a). This assumption is based on TEM study, which shows that LZO covers the layer between the LSM grains and the YSZ surface at the late sintering process (see chapter 4). The bigger contact area between the LSM and the YSZ, which is blocked by LZO phase, and the thicker the LZO layer, the more conducting electronic carriers, which are blocked by LZO phase. Therefore, the larger ohmic resistance at the late sintering process as the sintering time increases (Figure 5-8b).

Comparison of the total ohmic polarization to the LZO ohmic polarization is showed in Figure 5-8c. Figure 5-8d shows the normalized LZO electrical resistivity. Normalized LZO ohmic resistance dominates the total ohmic resistance, and it varies the total ohmic resistance of the LZO (Figure 5-8c). Large LZO ohmic polarization is ascribed to five orders of magnitude lower of the electrical than that of LSM [27,23], and two orders of magnitude lower than that of YSZ [29-33], therefore the magnitude of the LZO ohmic resistance is comparable to the total ohmic resistance. In addition, changes in the total ohmic resistance follow the same direction as variations in the LZO ohmic resistance. It might suggest that LZO phase formed at the LSM/YSZ interface changes cathode conduction mechanism by decreasing the effective conducting area at the cathode/electrolyte interface, therefore, cathode performance is degraded [127, 135, 136, 130, 138].

Figure 5-8d shows LZO normalized resistivity ($\rho_{O,LZO}$), which is the slope of the product of the R_{LZO} and S_c vs t_{LZO} . S_c is equal to $A_{LZO,TPB}$, which is blocked by LZO phase, then

$$\rho_{LZO} = R_{LZO} \frac{S_c}{t_{LZO}} \quad [5-9]$$

The slope (the LZO electronic resistivity) in Figure 5-8d is a constant, $\sim 5.4 \times 10^5$ (Ωcm), at a fixed temperature of 900 °C. The temperature was determined by furnace temperature when impedance data was collected.

The electrical conductivity of the LZO phase (the reciprocal of the slope) is approximated to be $2 \times 10^{-6} \text{ Scm}^{-1}$. It should be noted that the magnitude of the LZO electrical conductivity is calculated from the TEM measurement of the LZO layer. It is one tenth of $\sim 1e^{-5} \text{ Scm}^{-1}$ [101, 145, 144] of the LZO conductivity and much lower than $\sim 1e^{-3} \text{ Scm}^{-1}$ [30, 142], close to $1.1e^{-4} \text{ Scm}^{-1}$

[143], $2e^{-4} \text{ Scm}^{-1}$ [123] as well. This difference depends on techniques of the measurement, various defect chemistry of the dopants as well as different operating P_{O_2} ranges.

The degradation of the SOFC performance can be explained by contributions of the LZO phase to the ohmic polarization. LZO electrical resistivity is four orders of magnitude lower than conductivity of the YSZ [29-31] and seven orders of magnitude lower than conductivity of the LSM [14,23,27,101]. LZO electrical resistivity represents the interruption of the conduction mechanism of the electronic carriers through the contact region causes the increases in ohmic polarization.

5.2.4 Conclusions

Epitaxial relationship exists between the LZO and the polycrystalline YSZ. It was found that LZO growth was retarded by increasing Mn composition from a Mn-deficient LSM to a Mn-excess LSM. At the same time, reduction in La composition also retards LZO formation. Mn stabilizes the LSM and Mn-excess inhibits LSM decomposition thus decreasing supply of the La. As a result, LZO growth was delayed by reducing supply of the La to the LZO reaction.

Quantitative microstructure analysis of the LZO growth was first time related to the cathode polarization in the literature. The contributions of the LZO phase to the activation polarization and the total ohmic polarization of the SOFC were discussed. It is found that the calculated LZO electrical conductivity of $2 \times 10^{-6} \text{ Scm}^{-1}$ based on the microscopic analysis is smaller than the electrical conductivity of the LSM and YSZ. As a result, LZO phase becomes the major factor and attributes to the total ohmic resistance by changing conduction of the electrical species from the LSM to the TPB. The LZO phase has poor ionic conductivity compared to conductivity of the YSZ [29], LZO phase formed at the LSM/YSZ interface inhibits charge transfer reaction by blocking the supply of the oxygen reactant species from YSZ or LSM

to the TPB. In addition, LZO phase increases energy barrier for the charge transfer reaction to be activated.

5.3 Effect of the Topology Properties on Concentration Polarization

5.3.1 Literature Review

Pore-network models coupled with skeletonization models have been applied into simulations of the microvascular blood flow in some brain tissues to determine neuronal nutrition and development [146], the filtering process in some filtering cakes to design the filtering equipment [147] and the gas or oil transport in porous permeable rock to develop a successful hydrocarbon recovery process [148]. This is because the relationship between the bulk flow or transport properties of the media (quantified by the pore-network models) and the geometrical properties of the pore microstructure (characterized by the skeletonization models) is established. Pore-network modeling enables to gain fundamental understanding of multiphase fluid or gas flow in porous media. In conjunction with the skeletonization modeling in 3-D image analysis, it becomes possible to predict the fluid or gas transport properties of a porous media. Then the cathode concentration polarization can be associated with the gas transport properties of a porous media. The goal of this work is to understand how the geometric properties of the porous cathode affect the gas transport properties and therefore change cathode concentration polarization of SOFC. Unfortunately, development of a pore-network model is beyond the scope of this work to achieve the relationship between the geometric properties and the gas transport properties, therefore, relationships of two pore-network models developed by Mason and Koponen are applied into this work. However, this is the first study of quantifying the geometric property (tortuosity) of the porous cathode by implementing an elementary skeletonization model in 3-D image analysis. Three-dimensional images of the porous media are acquired by focus ion beam. Two pore-network models include Mason's dusty-gas model and Koponeon's

lattice-gas model. Two models predict gas transport properties of a porous cathode (effective diffusivity and permeability). The cathode concentration polarization is associated with the gas transport properties of a porous cathode by applying Kim's model.

5.3.1.1 Skeletonization model

Quantification of effective diffusivity and permeability need a way to quantify tortuosity, open porosity and pore surface area. Quantification of open porosity and pore surface area were explained in Chapter 3 and 4, the focus of this section is on quantification of the diffusional and hydraulic tortuosity by calculating geometric tortuosity using an elementary skeletonization model in 3-D image analysis. Despite its widespread use in petrophysics, tortuosity has various meanings to describe different transport processes taking place in a porous material, values for geometrical, diffusional, hydraulic and electrical tortuosity are generally different from one another [149]. Geometric tortuosity is the ratio of the pore length to the projection of the pores in the direction of flow [74]. In Mason's model, diffusional tortuosity is applied to study diffusion kinetics of a binary gas mixture. In Koponen's model, hydraulic tortuosity is used to analyze flow kinetics of a binary gas mixture. Differences in diffusion tortuosity and hydraulic tortuosity will be explained later.

An advanced skeletonization model in 3-D image analysis calculates geometric, diffusional and hydraulic tortuosity. It estimates transport distance of the gas through interconnected pore channels along the sinuous diffusion path when the transport is in the continuum diffusion domain [84] or approximates gas flow distance along the tortuous flow direction when transport is in the viscous flux domain [18]. In other words, gas transport distance is equal to the length of the skeleton of a connected pore-network (the length of the median axis of a pore-network). Additionally, skeletonization model determines the major flow channels of pores for the gas transport. In other words, connected flow channels with a large radius of pore throats are more

likely for gas transport to occur. Finally, it predicts efficiency of the gas transport through different topologies of connected pore channels. In other words, the higher volume fraction of the large radius of pore throats is within the porous cathode, the higher efficiency of the gas transport is through the porous cathode.

The elementary skeletonization model performs three main algorithms: homotopic, chamfer distance map and thinning algorithms in series. These algorithms are described in details in Fouard's paper [146]. Homotopic algorithm preserves the original topology of the 3-D pore space. Distance map algorithm ensures that the correct skeleton is located on media axis (center) of the original topology of the 3-D pore space. Euclidean distance map is similar to the topological map. It represents the shortest distance from a point of the 3-D pore space to its background in a unit of grey level. The background has the lowest grey level of zero. The media axis consists of points with the maxima distance maps. Thinning algorithm keeps crucial topological properties of the entire pore space and removes the redundant topological properties.

5.3.1.2 Pore-network models

Quantification of effective diffusivity and permeability become important in order to relate physical transport of gas in the porous cathode to the electrochemical property. The effective diffusivity of a binary gas is a key parameter to study gas transport kinetics [84]. Mason developed a two dimensional model to estimate the effective diffusivity of a binary gas under a steady-state in a porous media. The dust-gas model shows that effective binary diffusivity ($D_{c(eff)}$) is proportional to binary diffusivity of O_2-N_2 , $D_{O_2-N_2}$, porosity, V_V' , and reciprocal of the tortuosity, τ as the following [84]:

$$D_{c(eff)} = D_{O_2-N_2} \frac{V_V'}{\tau} \quad [5-11]$$

The magnitude of the $D_{c(eff)}$ of a composite anode ranges from $0.1\text{cm}^2/\text{s}$ to $0.2\text{cm}^2/\text{s}$ between 650°C and 800°C with the total porosity of 30%. The tortuosity of the composite anode is ~ 14.5 [13]. The flux dominated by the binary diffusion (continuous diffusion) is equal to the total flux of oxygen flowing in a porous media. Porous media was visualized as a matrix occupied by some immobile spherical molecules. V_v' represents the total porosity instead of the open porosity. Diffusion tortuosity is defined as the ratio of the gas diffusivity through the porous media ($D_{c(eff)}$) to the gas diffusivity through a dense bulk ($D_{O_2-N_2}$).

On the other hand, permeability is another important parameter to study fluid flow through a porous media [47]. The prediction of the permeability for various porous media has been performed either by the experimental methods or by the theoretical models. The experimental methods include mercury porosimetry, nuclear magnetic resonance, measurements of the electrical conductivity, and acoustic properties of the medium [151-156]. The theoretical simulation of the permeability involves models with the simplified pore geometries, microscopic fluid pattern and statistic methods [47, 157, 158]. However, various correlations between the permeability and the parameters describing the geometrical properties of the medium have been suggested. The simulated permeability of different types of sandstones varies from 116 to 5370 between porosity of 21.6% and porosity of 27%, although the same type of conduit simulation model was used to calculate permeability [47].

Koponen et al. studied the viscous flow in a complex porous microstructure in a two-dimensional lattice-gas model [18, 42]. The lattice-gas model relates the permeability (physical properties of the viscous flow in a porous media) to the geometry of microstructures (microstructure properties of the porous media) by modifying a simple capillary theory of Kozeny et al. [17]. Koponen et al. devised collections of two-dimensional model of

microstructure with various open porosity, V_v , then the fluid flow through each of these microstructures was simulated, finally, the permeability, K , was calculated as a function of open porosity. On the other hand, the relationship of permeability and geometry of the microstructure was achieved after tortuosity (τ), and pore surface area (S_v) were expressed in terms of open porosity (V_v). In other words, a theoretical relationship between the permeability (K) and the geometry of the microstructure was expressed as a function of open porosity (V_v). Then the simulated K vs V_v and the theoretical K vs V_v were compared for four different equations, which gave different relationships between K and the microstructure geometry. The following equation (5-11) fits very well with the open porosity of 33%-90% and is showed as the following:

$$K = \frac{V_v^3}{c\tau^2 s_v^2} \quad [5-11]$$

where c is a fitting parameter of the Kozeny coefficient (shape factor of the particle) with a range of 2-12. The magnitude of the normalized permeability (K/R^2) ranges from $5 \cdot 10^{-4}$ to $2 \cdot 10^{-3}$ with an open porosity of 33% and an open porosity of 43%, respectively. The value of the tortuosity is ~ 1.7 [42]. R is the averaged particle size in the simulation model. The hydraulic tortuosity is interpreted as the average of the relative lengths of the flow lines of all fluid elements with a fixed volume, passing through a given cross section during a given period of time (weighted averaging flux). Based on this two-dimensional lattice-gas model, a three-dimensional *ab initio* lattice-Boltzmann model has been developed to simulate the creeping flow through large random fiber webs. The simulated permeability is in good agreement with the experimental permeability in the fiber webs.

One of the differences between the Mason's model and the Koponen's model is the assumption of the controlled mechanism of the total oxygen flux. The flux of oxygen controlled by viscous flow is the major flux of oxygen flowing into a porous media in the Koponen's model. The porous media is envisaged as few hundreds of randomly positioned particles in two dimensions. The Mason's model assumes that continuum diffusion dominates the total flux of oxygen through a porous media, which consists of fixed particles. Two domains are possible for SOFC under operations. A second difference between the Mason's model and the Koponen's model is the definition of the porosity. Porosity in Mason's model includes porosity of closed pores and open pores. Whereas, porosity of open pores is taken into account in the Koponen's model. Open porosity of the porous media is determined by the fraction of the overlapped region between particles in the whole region. The third difference between two models is the definition of the tortuosity. Mason uses the diffusional tortuosity in his model, which is the averaged ratio of effective diffusivity to bulk diffusivity [159] formulated to porosity. In most SOFC models, the diffusional tortuosity is a function of the geometric tortuosity [13, 160-162], which is the ratio of the pore length to the projection of the pores in the direction of flow [74]. The value of the geometric tortuosity is 3 for an ideal isotropic porous media [163], and most often in the range of 2-10 for porous sintered ceramics [164] and 10-17 for anode tortuosity [13, 160,165]. Koponen utilizes the Kozeny hydraulic tortuosity (a weighted averaging flux in a flow field) in the calculation of the permeability. In unsolidated granular aggregates, the value of Kozeny hydraulic tortuosity ranges from $2^{0.5}$ to 2 and it rises up to ~5 in consolidated rocks and soils [47]. Witt et al. suggest that an upper limit on tortuosity in uncemented granular media is ~10 with platy grains [166].

5.3.1.3 Impact of gas transport on concentration polarization

Kim related microstructure parameters to the concentration polarization of SOFC by first introducing dusty-gas model as described in Chapter 1. Later on, the dusty-gas model was applied into SOFC models to simulate performance of the electrodes [13, 160-162].

Equation 1-12 shows that the concentration polarization is increased as decreasing the cathode limiting current density. The tortuosity and open porosity are related to the concentration polarization by

$$\eta_{conc}^c = -\frac{RT}{4F} \ln\left(1 - \frac{\tau}{V_v} i \times C\right) \quad [5-12]$$

where i is the current density and C is a function of oxygen partial pressure on the cathode side, $p_{O_2}^c$, operation temperatures, T , atmosphere pressure, p , and cathode thickness, l_c . Thus, $C = f(p_{O_2}^c, T, p, l_c)$. In this study, C is assumed to be a constant.

If the viscous flux dominates the total flux of oxygen flowing into the LSM/Pore surface ($J_{O_2,CP}^V$), the permeability is related to the concentration polarization by

$$\eta_{conc}^c = -\frac{RT}{4F} \ln\left(1 - \frac{\tau^2 s_v^2}{V_v^3} i \times C'\right) \quad [5-13]$$

where C' is affected by a Kozeny coefficient and C in equation 5-12. Under a steady-state operational condition, C' is a constant. Ideal gas law states that permeability is proportional to effective diffusivity. The permeability can be associated with the concentration polarization by using Kim's model.

5.3.2 Experimental Design

Symmetric SOFC samples were prepared (see section 4.1.3). This set of eight isothermal samples was sintered at 1200°C from 2h to 25h. The resulting symmetrical samples had a

cathode thickness of about $43\mu\text{m}$ and YSZ thickness of $180\mu\text{m}$. A set of fiduciary marks was patterned beside of the region of interest for accurate alignments. Few hundreds of plane-serial sections with a spacing of $0.044\mu\text{m}$ - $0.064\mu\text{m}$ were taken from an area of $15\mu\text{m} \times 20\mu\text{m}$ parallel to the LSM/YSZ interface and $\sim 5\mu\text{m}$ away from the LSM/YSZ interface. A Ga ion beam current of 300pA was used to mill materials layer by layer (see section 3.3.3). The contrast and brightness of each plan-view image was kept as close as possible for accurate skeletonization of one whole set of plane-serial images.

Before quantification of the topology of the cathode microstructure, the stacks of the plane-section images were load into a ResolveRT software. The pixel size of the plan-view images is $0.019\mu\text{m}$ by $0.024\mu\text{m}$ on the plane parallel to the LSM/YSZ interface. The pixel size in the direction away from the normal of the YSZ/LSM interface ranges from $0.044\mu\text{m}$ to $0.064\mu\text{m}$. After plane-view images were aligned and were segmented, the segmented images were skeletonized. The elementary skeletonization consists of pre-correcting artifacts of the plane-view images, adjusting threshold, reconstructing 3D pore space, thinning 3D pore space to the 3D pore networks, and calculating diameter of each branch in the 3D pore networks. In one whole set of serial slices, the decreased average intensity in some slices was pre-corrected by the CorrectZDrop module. The intensity changed in some slices due to excessive light absorption in other slices during the FIB/SEM operation. In order to reconstruct the 3D pore space, the thresholding images were segmented to differentiate pores from grains. A consistent value of the threshold was used for all images of eight samples. The main algorithm in the skeletonization model is the thinning algorithm. It peels off the exterior skin of the 3-D pore space layer by layer until the skeleton of the 3-D pore space is the media axis of the 3-D pore space. Evalonlines module provides radii of branches (pore channel) and branch junctions (pore throats) in a 3-D

skeleton of a pore-network. Lineset module was used to provide 3-D coordinates of the center of the pore channels. A matlab script was compiled to identify pore throats and to calculate the distance between adjacent connected pore throats (the length of the branch between connected pores). The connected pore throats have the maxima of the radii of pore channels. The tortuosity was normalized by the total length of the connected branches in the 3-D pore network divided by the total spacing of the stacks of the plane-section images (total distance is milled away toward the LSM/YSZ interface). Area probe was applied to the segmented plane-section images to quantify area fraction of open pores and pore surface area.

5.3.3 Results and Discussion

The elementary skeletonization model was implemented for eight isothermally sintered samples. The skeletons of the 3-D pore space in the isothermally sintered samples are shown in Figure 5-9. Figure 5-9a shows the typical skeleton of a 2-D pore channel with the dimension of $15\mu\text{m}$ by $15\mu\text{m}$. Most pores are connected by a continuous pore skeleton. Three-point and four-point junctions are most common (Figure 5-9a). It is noted that the skeleton of the 2-D pore channel follows the media axis of the 2-D pore structure. It means that the homotopic skeleton of the 2-D pore channel is achieved. The 3-D skeletons of a pore network were constructed based on the homotopic skeleton in 2-D (Figure 5-9b). These skeletons in 3-D were from the same volume for the set of the isothermally sintered samples. Pore-network density changes as the sintering time increases. Radius of the branches of the skeleton varies within one pore-network. Changes in the radii of the skeleton branches were also visible between different pore-network. Figure 5-9b indicates that varies in radii of the branches of the skeleton as well as changes in skeleton density become apparent between the sample sintered for 15h and the sample sintered for 25h. It indicates differences in tortuosity between these samples (Figure 5-10a).

Figure 5-10 shows tortuosity, open porosity and pore surface area as a function of the sintering time. Open porosity is initially increased by 33% as the sintering time increases up to 10h (Figure 5-10b). It might be contributed to the growth of continuous pore channels as the sintering time starts to increase, therefore the area fraction of the open pores in the FIB/SEM image increases. Connectivity density is gradually increased and then reduced (Figure 5-10c). After sintering for 10h, continuous pore channels pinch off and connections between continuous pore channels are lost to the minimum (Figure 5-10c), therefore open porosity is decreased by 16% at the sintering time of 25h. Pore surface area is decreased and the minimum occurs after the sintering time for 10h (Figure 5-10d). It means that growth of pore channels is the maximum at this time. After sintering for 10h, the growth of pore channels is abruptly slow down, and the pore surface area is slightly decreased. Tortuosity value of the porous cathode ranges from 2 to 17 [164, 160, 165]. Tortuosity shows a trend of the slow increase followed by the fast increase after sintering for 10h (Figure 5-10a). The number of connections between pore channels and radii of pore throats affect tortuosity. If wide pore throats are connected to other continuous pore channels, gas is more likely to transport through these wide pore throats than pore throats with narrow opening, therefore the tortuosity is small. However, if wide open pore throats are connected to isolated pore channels, gas prefers to flow through the pore throats with the narrow opening, because such kind of pore throats are connected to continuous pore channels, therefore, the tortuosity is large. After sintering for less than 10h, the loss of connections to other channels competes over the growth of pore channels, although pore throats become wide, tortuosity slightly increases by reducing connectivity density (Figure 5-10c). Shrinkage or pinching-off of the continuous pore channels causes the decreasing of the diameter of the pore throats as well as the decreasing of the number of the wide pore throats within the cathode bulk. Additionally,

reduction in connections between adjacent pore channels results in the decrease of the connectivity density of pores in the cathode bulk (Figure 5-10c). Loss of connectivity density and reduction in number of wide open throats (Figure 5-10b) dramatically increases tortuosity after sintering for 10h.

The effective diffusion coefficient (open porosity over tortuosity) and the permeability are plotted as increasing the sintering time (Figure 5-11). The relationships between the gas transport resistance and the geometric properties are shown in Figure 5-11 (effective diffusivity) and Figure 5-12 (permeability), respectively. Figure 5-11a shows that increase in tortuosity reduces the effective diffusion of the O₂-N₂, by at most two times. The value of the effective diffusivity of the O₂-N₂ ranges from 4*10⁻³ cm²/s to 2.1*10⁻² cm²/s at 1200°C. It is lower than Kim's result of 0.2cm²/s for the effective diffusivity of the H₂-H₂O at 850°C. It has been confirmed that effective diffusivity of the O₂-N₂ is lower than that of H₂-H₂O [26]. The gas transport resistance appears to increase by decreasing the effective diffusivity (Figure 5-11c). The higher effective diffusivity, the faster kinetics of the gas transports through the porous cathode, therefore the less resistance to the gas transport [13, 167]. The expected logarithmic relationship in Kim's model was not observed in Figure 5-11b. This difference is caused by a wide range of tortuosity and open porosity that has been studied in this work. The relationship between the gas transport resistance and the effective diffusivity is analyzed by varying tortuosity (2-12) and open porosity (0.23-0.41). Additionally, usage of the total porosity in Kim's model is one reason. The difference between the open porosity and total porosity can be up to 100% in case of open porosity of 20% [42].

The magnitude of the normalized permeability ($\frac{K}{R_p^2}$) is between 10⁻⁴ and 3*10⁻³ with an open porosity of 23%-41% (Figure 5-12a). R_p represents pore radius. It is consistent with

Koponen's normalized permeability. It ranges from $5 \cdot 10^{-4}$ to $2 \cdot 10^{-3}$ for the open porosity of 33%-43%. The normalized permeability appears to be insensitive to the sintering time.

Permeability describes two competitive microstructure evolutions: volume changes in pore channels and connections changes in pore channels within the porous cathode. If volume of open pores as well as connection among pores are decreased at a same rate, then permeability will decrease. If the connections among pores decrease faster than volume fractions of open pores reduces, then permeability will not monotonically decrease. If the viscous flux dominates the total flux of oxygen flowing into the LSM/pore surface ($J_{O_2,CP}^V$), the gas transport resistance is reduced by increasing the permeability as showed in Figure 5-12b. The ineffective gas transport through the porous cathode contributes to the starving of the oxygen therefore slows down kinetics of the oxygen reduction. As a result, concentration polarization is increased. The impact of the permeability on the gas transport resistance is compared to the effect of the effective diffusivity on the gas transport resistance (Figure 5-11b and Figure 5-12b). A direct relationship was observed between the permeability and the gas transport resistance as compared to the relationship of the effective diffusivity. It might indicate that the skeletonization and the lattice-gas models are more applicable to study gas transport properties in a porous cathode than the dusty-gas model. In other words, the tortuosity quantified by the skeletonization model might represent the hydraulic tortuosity (the weighted velocity of fluid flow in a fluid flow field) in Koponen's model instead of the diffusional tortuosity in Mason's model (the averaged ratio of the diffusion through a porous material to the diffusion through a dense bulk). In addition, changes in connections among pore channels are important to study gas transport properties. Mason's model neglects variations in connections between pore channels, therefore, the

contribution of the effective diffusivity to the gas transport resistance is not as direct as that of the normalized permeability.

An accurate skeleton model needs to preserve the topological properties of the original object (homotopy) [168, 169]. A homotopic skeleton depends on the thresholding algorithm [146]. Inconsistent thresholding causes loss of branches in a skeleton of a pore network thus under estimating tortuosity. In addition, under-threshold results in enlargement of the mean diameters of the wide-open pore throats [146] thus over estimating the efficiency of the gas transport through pore channels. An accurate skeleton model requires that the skeleton of a pore network is consistent with the media axis of the original object. It relies on segmentation of FIB/SEM images. Over-segmentation and under-segmentation of the edge of pores cause shift of the media axis of the skeleton in a pore-network, therefore cause inaccurate quantification of the tortuosity. A study of the gas transport efficiency through the porous cathode is compromised by two limitations of the skeletonization model (over-threshold and under-segmentation) discussed above. The major flow channels need to be accurately identified before transport efficiency is qualitatively assessed. A verification of the skeletonization model needs to be performed by a separate model. This model should reconstruct the flow field by using the radii of pore throats as well as the distribution of pore throats as inputs of the model, which were calculated from the elementary skeletonization model. The advanced model is expected to simulate skeleton of a 3-D pore-network to test the accuracy of the elementary skeletonization model. In addition, main flow channels (pore throats with wide opening) should be determined based on comparing the radii of pore throats as well as the distribution of pore throats to one another. Then the frequency of main flow channels through which gas transport can be estimated. The distribution of the main flow channels determines the gas transport efficiency within the porous cathode.

5.3.4 Conclusions

Topology of the LSM has been related to the concentration polarization. It is the first time that tortuosity is quantified by an elementary skeletonization model in 3-D for this material. It appears work well to analyze concentration polarization. The magnitude of the tortuosity falls into the range of the tortuosity for the sintered ceramics. Two models with different assumptions on the major O₂ flux show that increasing the geometric factors (effective diffusivity and normalized permeability) will reduce the gas transport resistance. The value of the effective diffusivity of the O₂-N₂ was confirmed lower than that of H₂-H₂O. In the binary diffusion dominant regime, the gas transport resistance was not monotonically increased by increasing logarithm of $\frac{\tau}{V_v}$ as predicted by Kim. The inconsistency with Kim's model is due to a different range of the tortuosity, different definition of the porosity as well as the assumption of grains in a porous media. On the other hand, in the viscous flux dominant regime, the magnitude of the normalized permeability is consistent with Koponen's normalized permeability. A direct relationship was observed between the increasing of the permeability and the decreasing of gas transport resistance. The limitation of the elementary skeletonization model was addressed. Future work on the development of the skeletonization model was suggested.

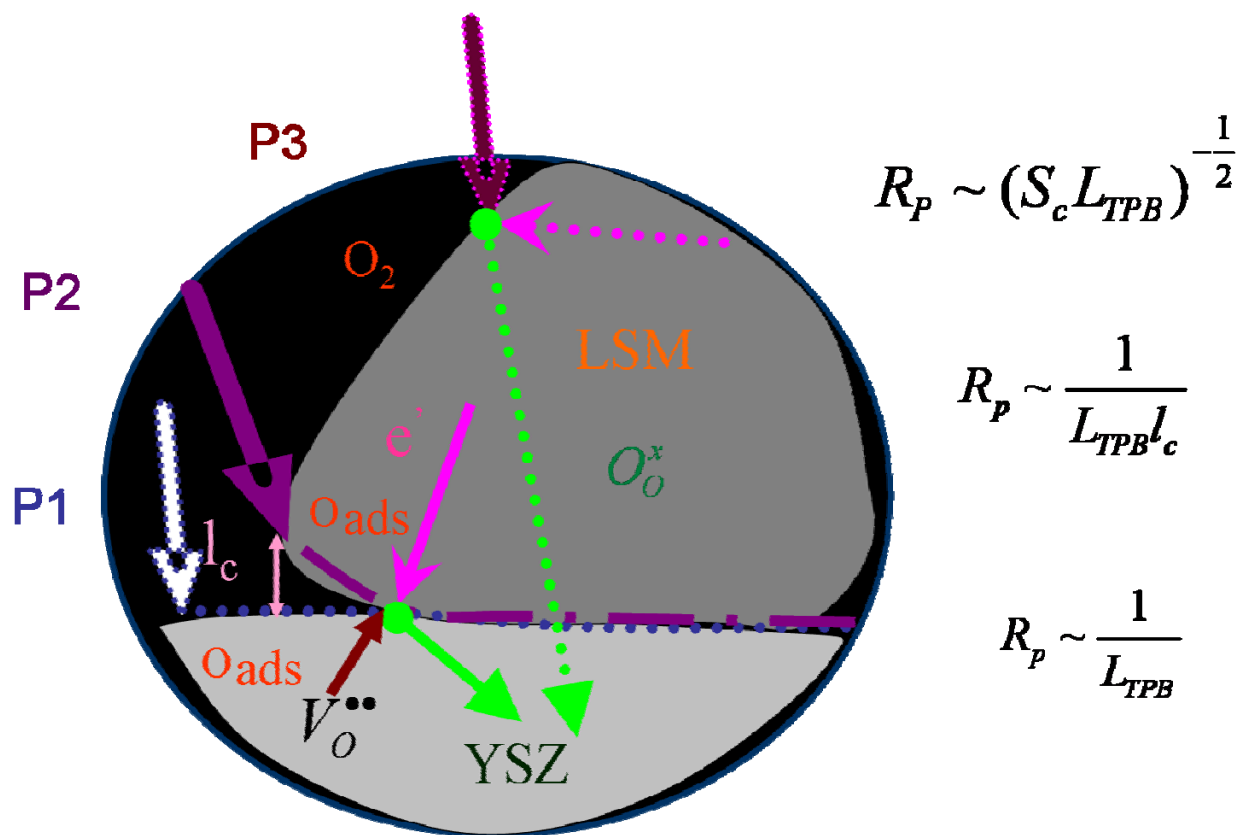


Figure 5-1. Three paths of oxygen reduction: P1 [4], P2 [109] and P3 [107, 110]

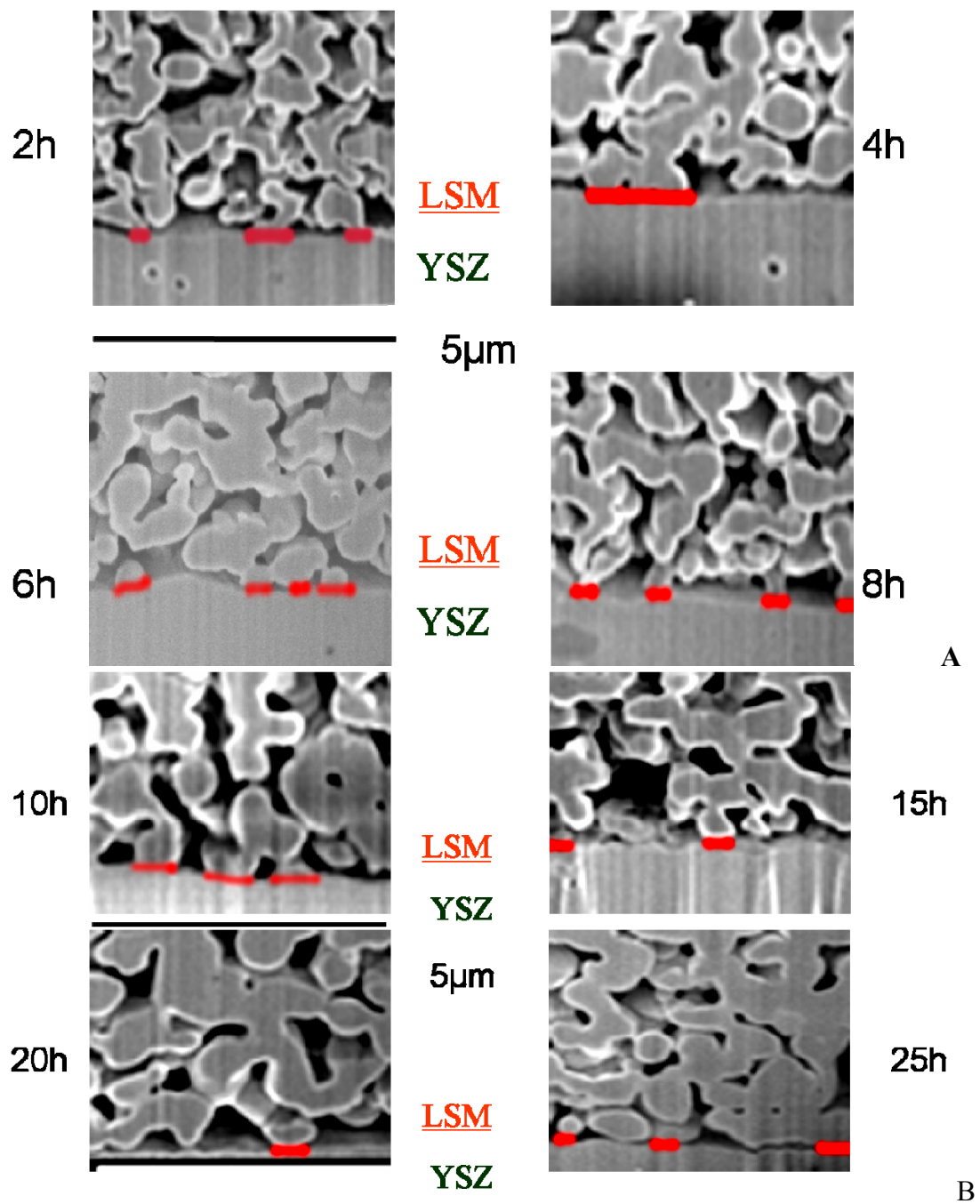


Figure 5-2. Cross-section images of the isothermal sintered samples. A) 2hrs-8hrs. B) 10hrs-25hrs

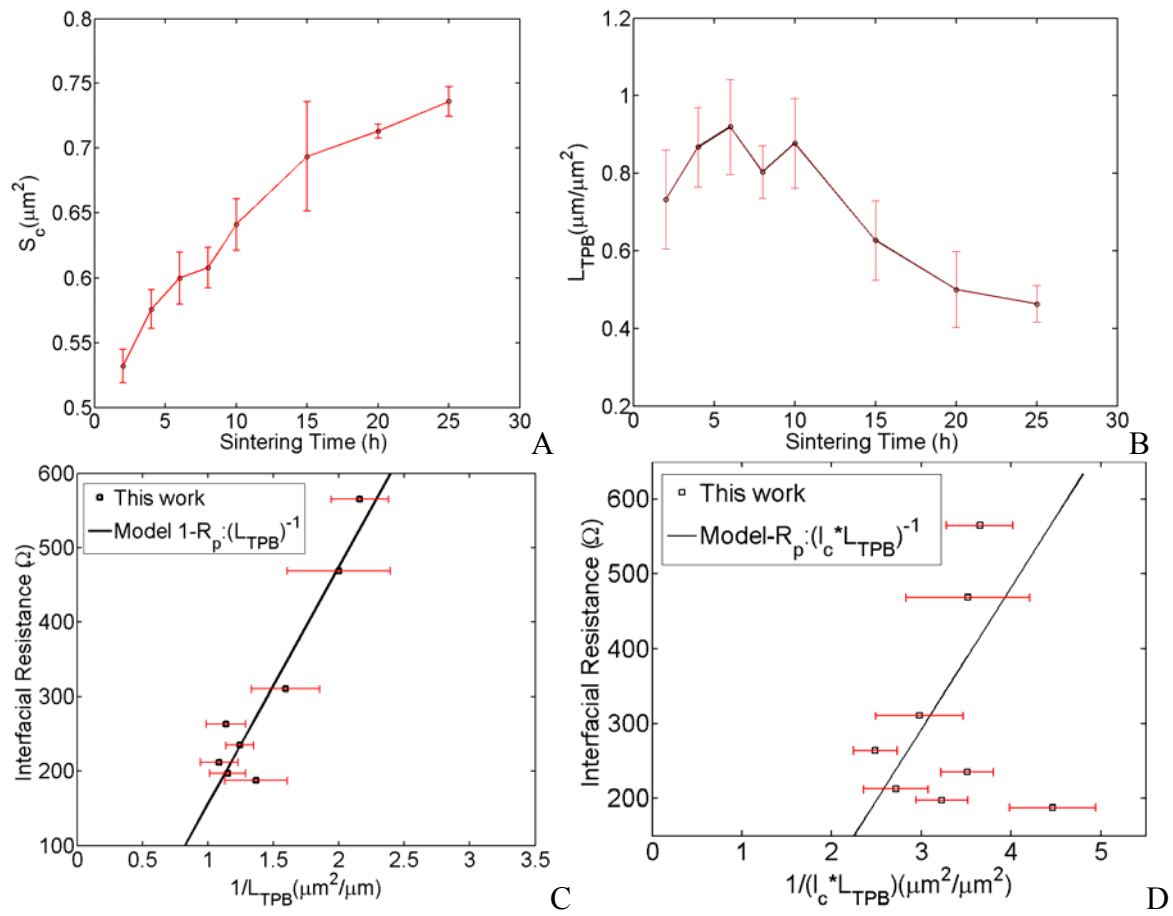


Figure 5-3. Continued

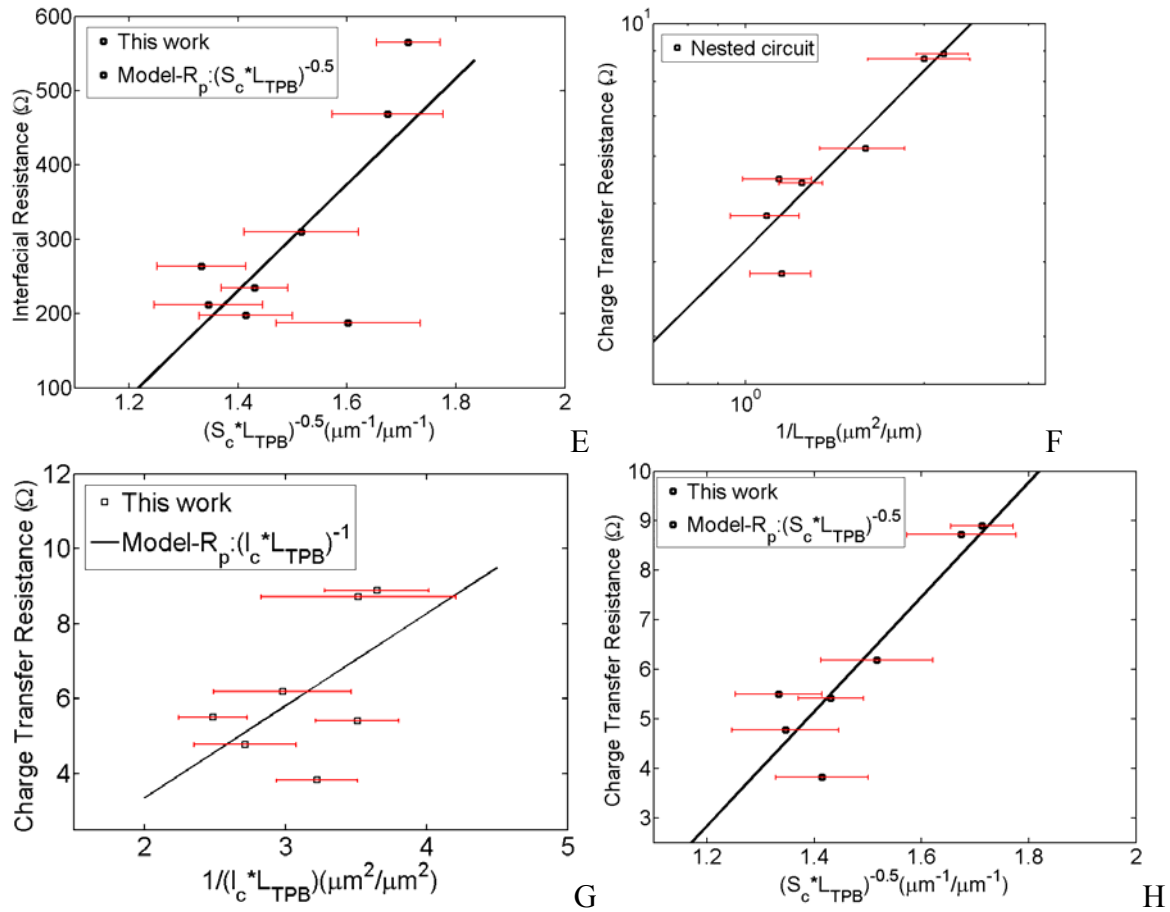


Figure 5-3. Effect of the L_{TPB} on the activation polarization. A) Contact area between the LSM and YSZ for the isothermal sintered samples. B) L_{TPB} for the isothermal sintered samples. C) Impact of the L_{TPB} on interfacial resistance. D) Effect of the collection length and L_{TPB} on interfacial resistance. E) Effect of the contact area and L_{TPB} on interfacial resistance. F) Impact of the L_{TPB} on charge transfer resistance. G) Effect of the collection length and L_{TPB} on charge transfer resistance. H) Effect of the contact area and L_{TPB} on charge transfer resistance.

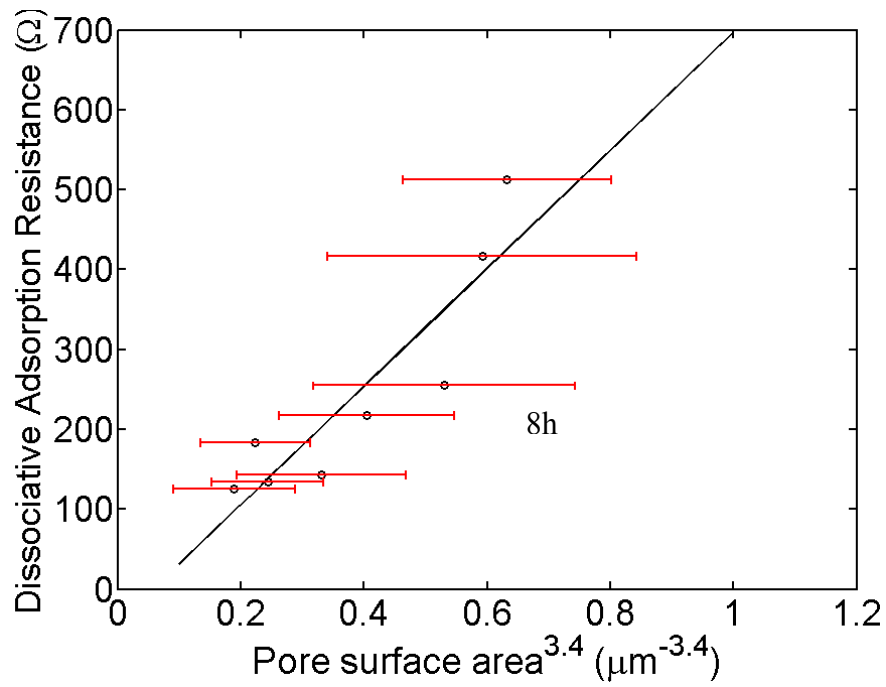


Figure 5-4. Effect of the S_V on the activation polarization of the isothermal sintered samples

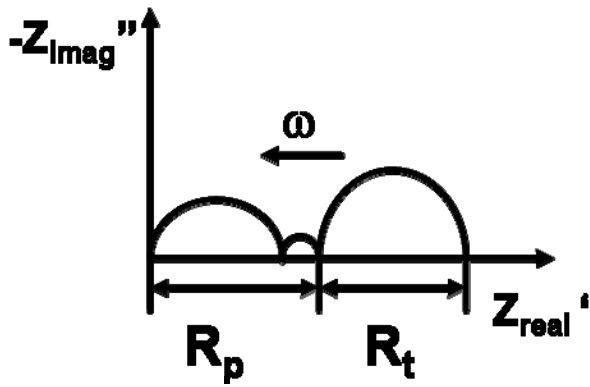


Figure 5-5. Nyquist plot of the interfacial resistance

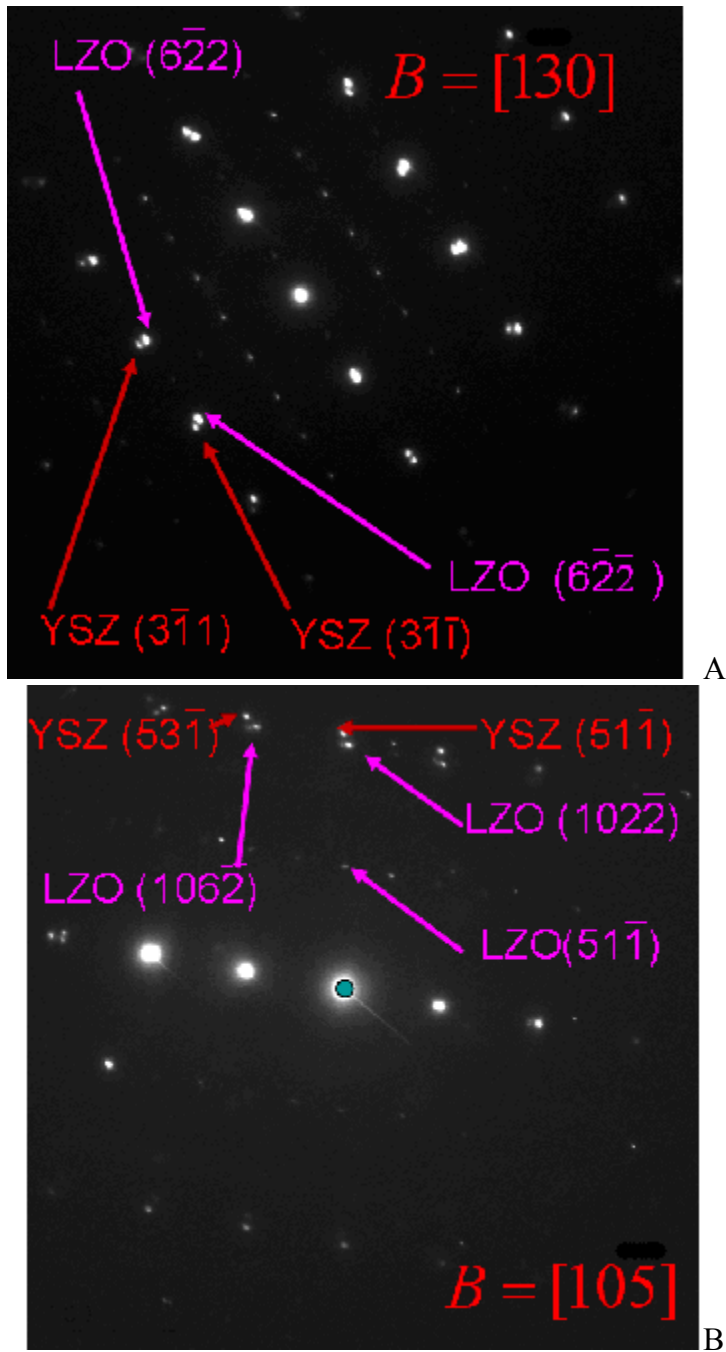


Figure 5-6. Epitaxial relationship between the LZO and the polycrystalline YSZ. A) LZO vs. YSZ with $B = [130]$. B) LZO vs. YSZ with $B = [105]$.

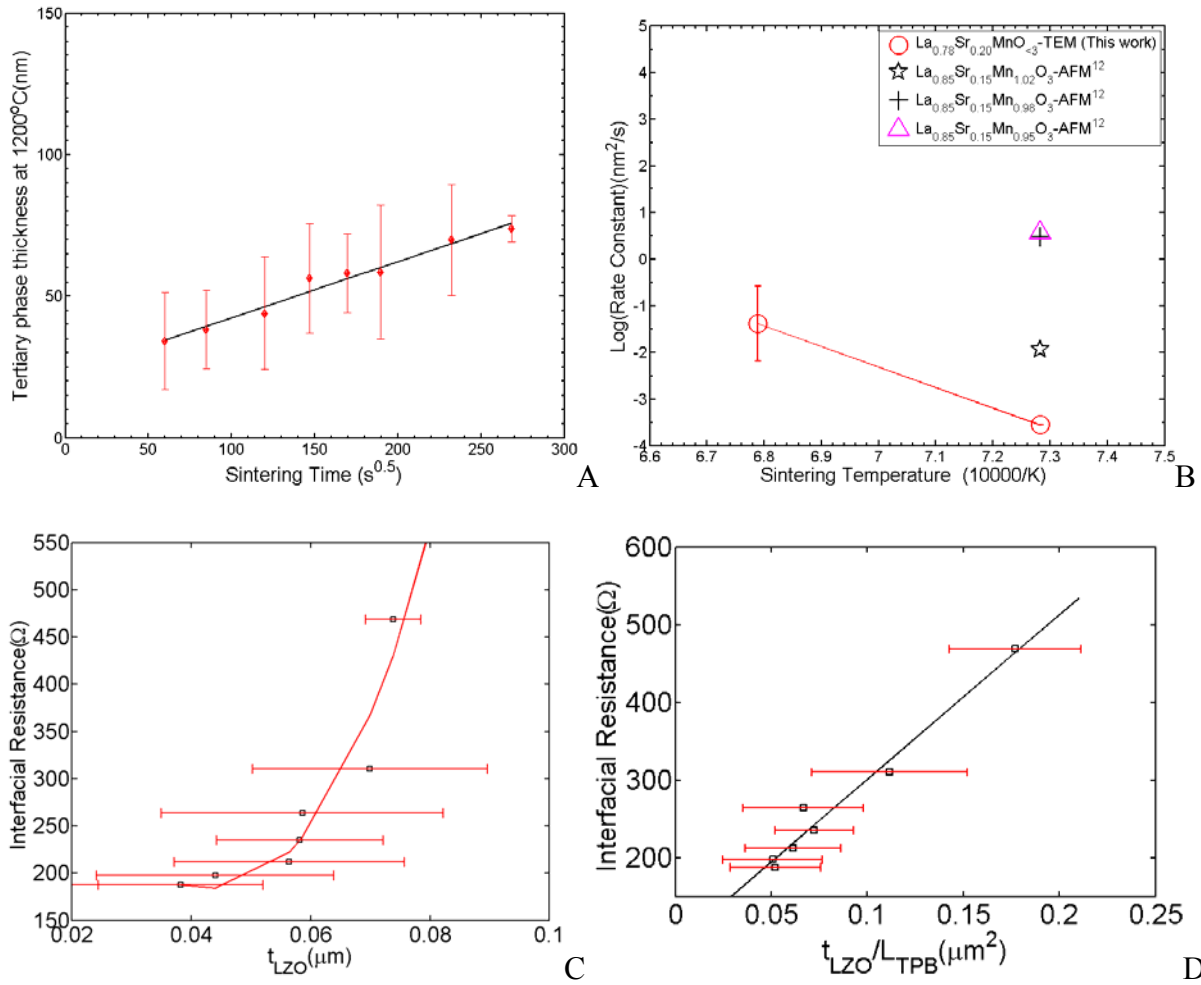


Figure 5-7. Effect of the LZO on the activation polarization. A) Thickness of the LZO for the isothermal sintered samples (t_{LZO} vs. $t^{0.5}$). B) Rate constants of LZO formation for Mn deficient LSM and Mn excess LSM. C) LZO phase contribution to the interfacial resistance. D) Cooperative contribution of LZO thickness to the Mizusaki's model. E) Cooperative contribution of LZO thickness to the Steele's model. F) Cooperative contribution of LZO thickness to the Kuzenocov's model. G) LZO phase contribution to the charge transfer resistance. H) Cooperative contributions of LZO thickness and TPB length to the charge transfer resistance. I) Cooperative contributions of LZO thickness, collection and TPB length to the charge transfer resistance. J) Cooperative contributions of LZO thickness, contact area and TPB length to the charge transfer resistance.

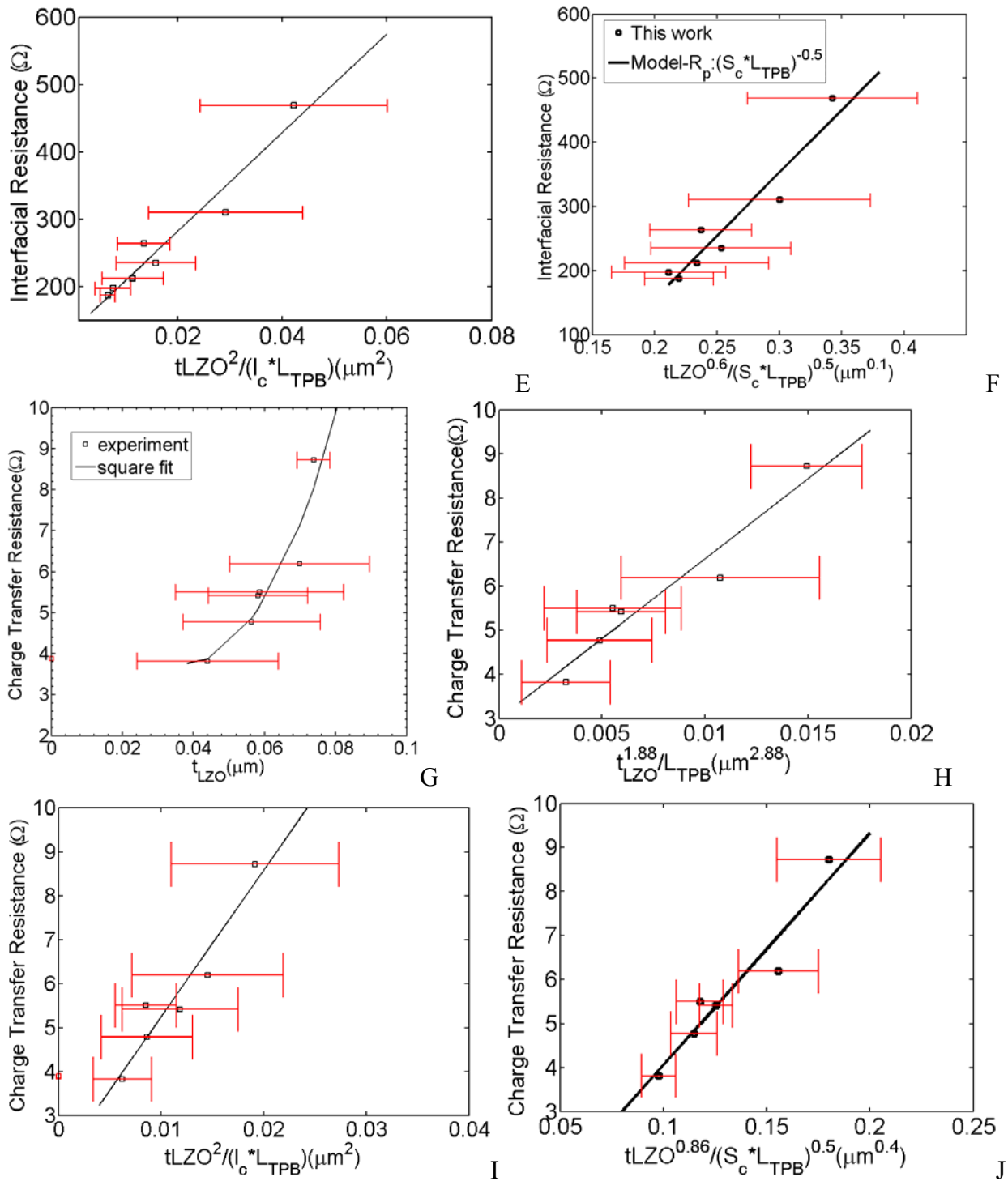


Figure 5-7. Continued

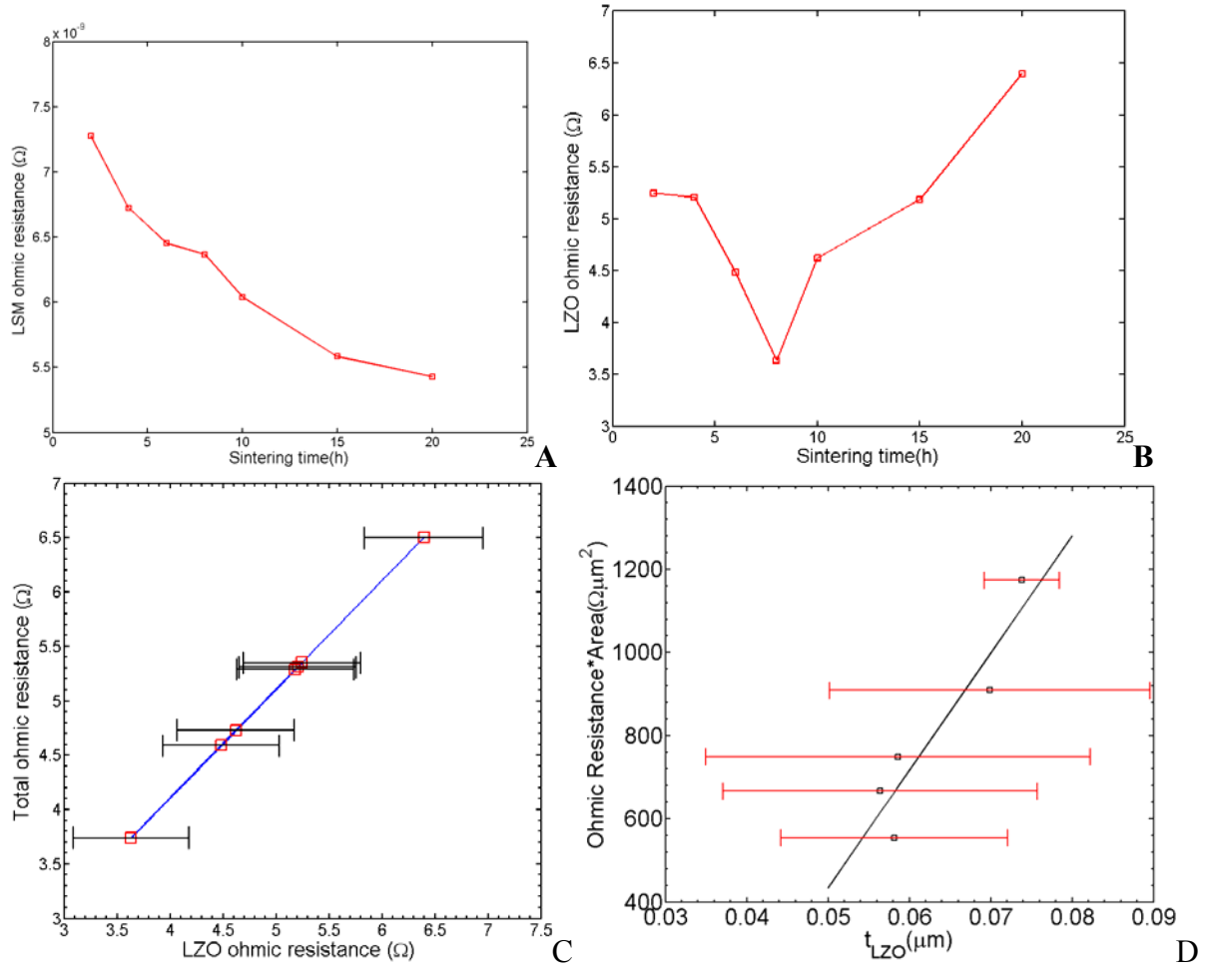


Figure 5-8. Effect of metric properties on Ohmic polarization of the isothermal sintered samples. A) LSM ohmic polarization . B) LZO ohmic polarization . C) Contribution of the LZO phase to the ohmic polarization. D) LZO electrical resistivity.

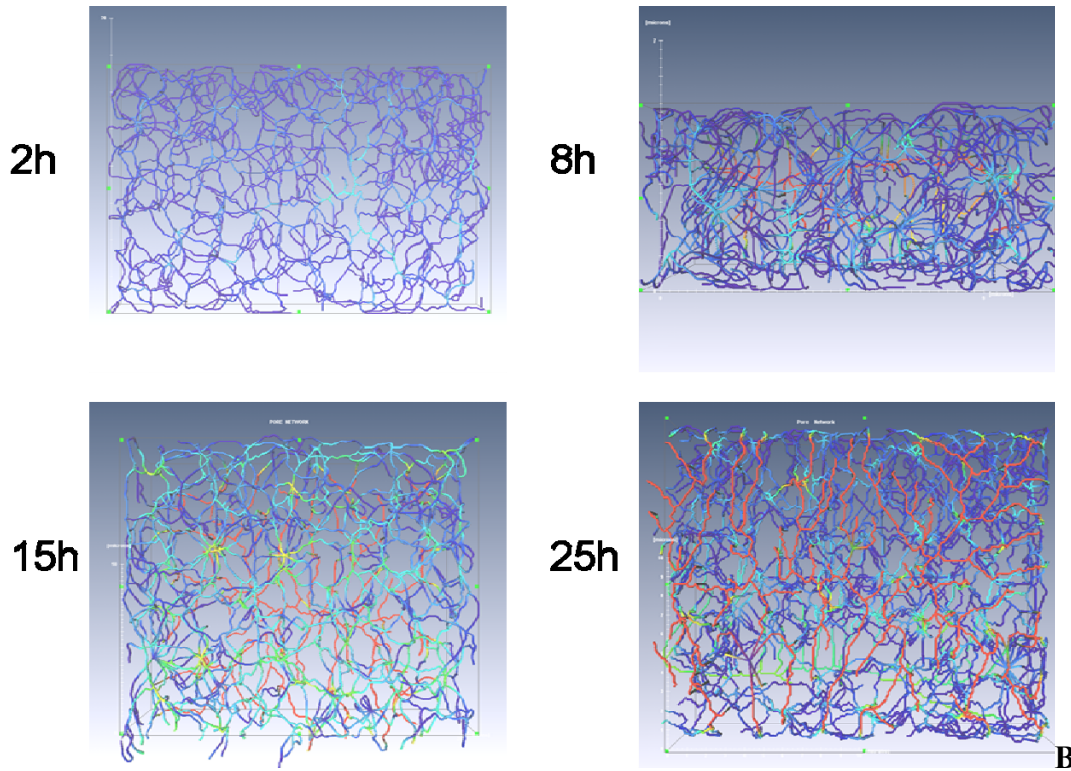
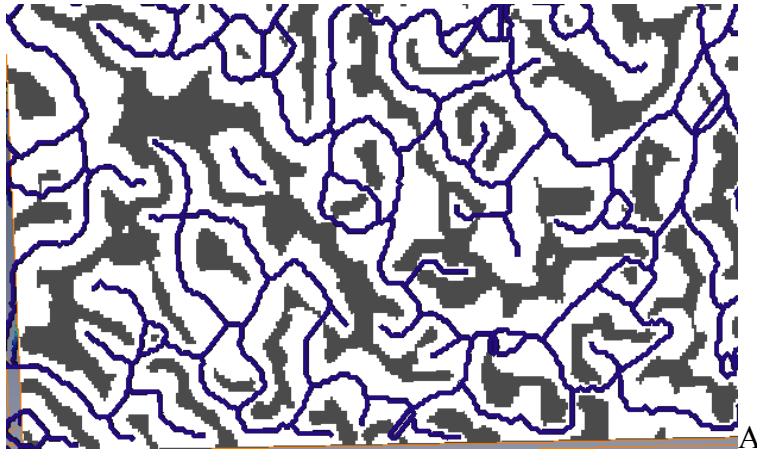


Figure 5-9. Skeleton of pore networks for the isothermal sintered samples. A) Homotopic skeleton of a 2-D pore structure, (note that line loop matches with the media axis of the 2-D pores). B) Skeleton of a 3-D pore space (note that different colors represent different radii of skeletons)

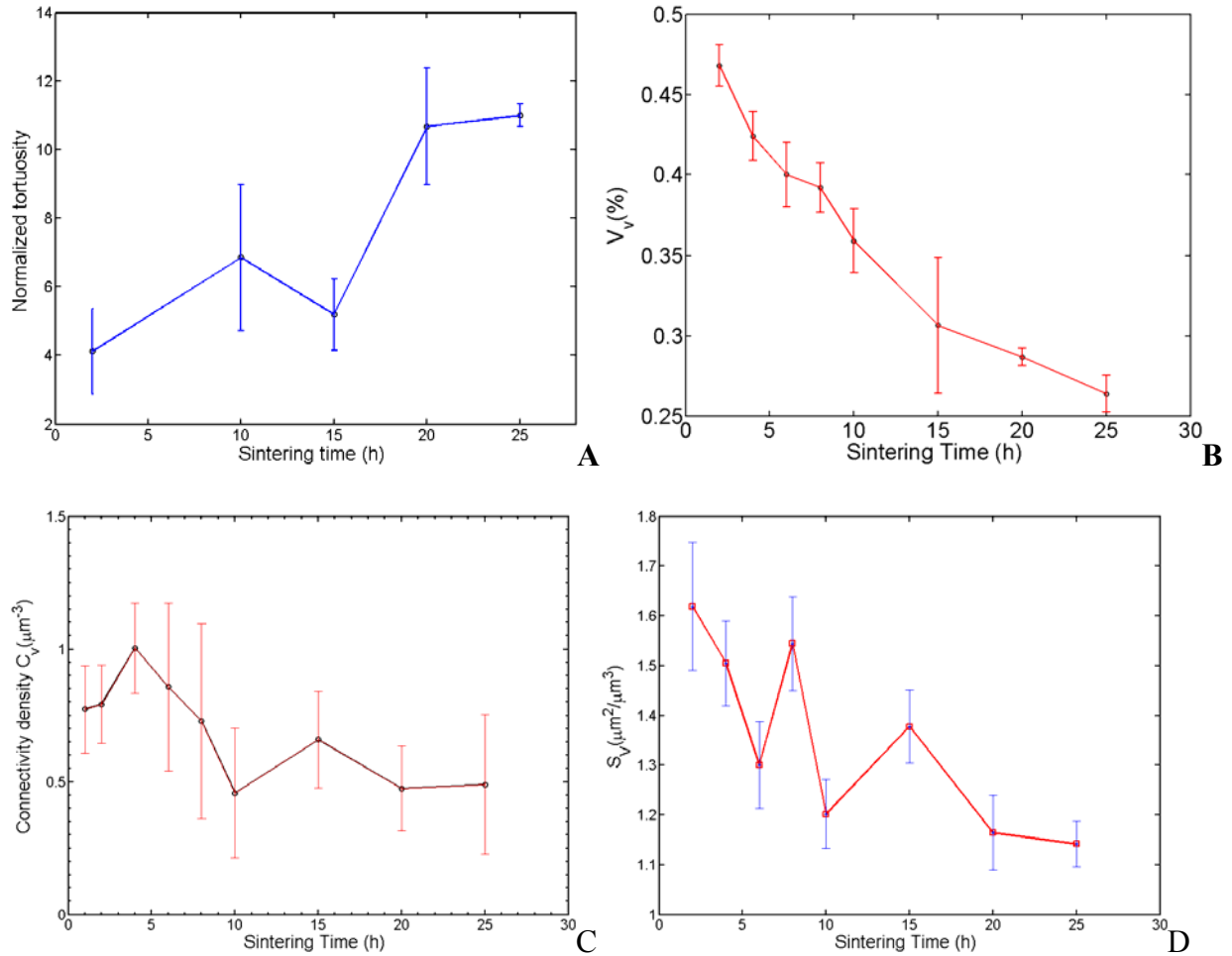


Figure 5-10. Microstructure properties for the isothermal sintered samples. A) Tortuosity. B) Porosity. C) Connectivity density. D) Pore surface area.

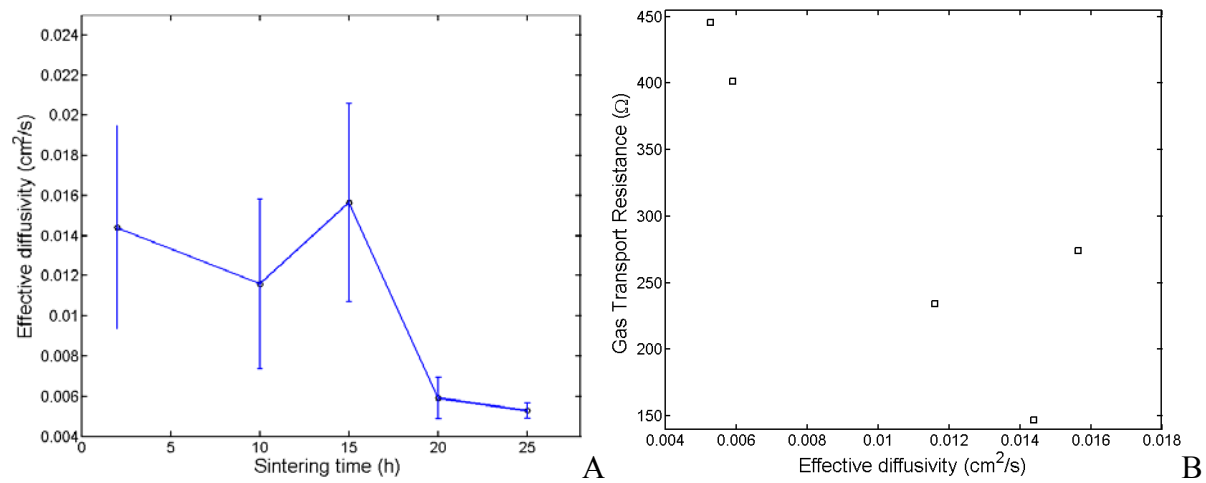


Figure 5-11. Effect of microstructure properties on concentration polarization by Kim's model. A) Effective diffusivity for the isothermal sintered samples. B) Impact of the effective diffusivity on concentration polarization [13].

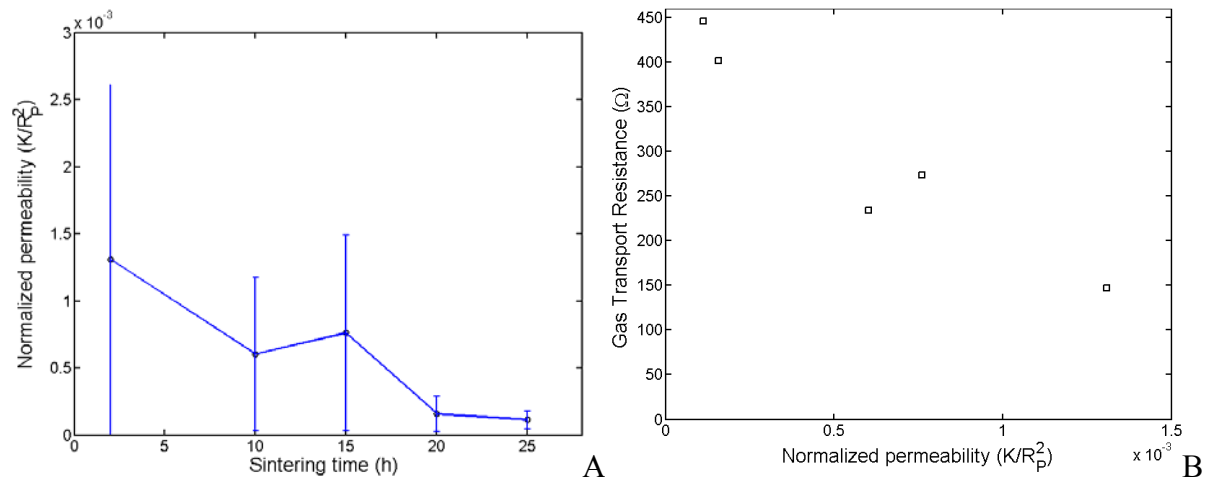


Figure 5-12. Effect of microstructure properties on concentration polarization by Koponen's model. A) Permeability for the isothermal sintered samples. B) Impact of the permeability on concentration polarization

Table 5-1. Calculation of the LZO ohmic polarization (resistance)

Time (h)	$\eta_{O,T}$ (Ω)	$\eta_{O,LSM,LZO}$ (Ω)	$\eta_{O,LSM}$ (Ω)	R_{LZO} (Ω)	$\rho_{O,LZO}$ ($\Omega\mu\text{m}$)	$\frac{1}{L_{TPB}}$ (μm)	$\frac{t_{LZO}}{L_{TPB}}$ (μm^2)
2	5.35	5.28	7e-9	5.28	0.20	1.37	0.052
4	5.31	5.24	7e-9	5.24	0.23	1.15	0.051
6	4.59	4.52	6e-9	4.52	0.25	1.09	0.061
8	3.74	3.67	6e-9	3.67	0.21	1.24	0.072
10	4.73	4.66	6e-9	4.66	0.27	1.14	0.067
15	5.29	5.22	6e-9	5.22	0.36	1.60	0.111
20	6.50	6.43	5e-9	6.43	0.47	2.00	0.148

$\eta_{O,T}$ -Total ohmic polarization; $\eta_{O,LSM,LZO}$ - Sum of ohmic polarization of LSM and LZO ; $\eta_{O,LSM}$ - LSM ohmic polarization, cross section area normalized by $S_C C_V$; R_{LZO} -LZO ohmic resistance, cross section area normalized by $S_C C_V$; $\rho_{O,LZO}$ - $\eta_{O,LZO}$ multiply by t_{LZO} ; $\eta_{O,YSZ}$ - Ohmic polarization of YSZ, 0.07 Ω

CHAPTER 6 SUMMARY AND FUTURE WORK

6.1 Summary

Understanding of the influences of the microstructure properties on kinetics of the oxygen reduction mechanism and subsequently on cathode polarization is necessary to engineer designs of the SOFCs. Before it can be fully implemented, it is crucial to develop effective FIB techniques in order to investigate these materials and to combine new techniques with other analytical methods for advanced analyses. This thesis has attempted to characterize 3D and 2D microstructure of the SOFCs and to discuss the effects of the specific geometric factors on components of the cathode polarization. A deep investigation of the contributions of a deleterious phase to the cathode performance has been performed. In this final chapter, the contributions of this research will be reviewed and areas for further study will be suggested.

6.1.1 FIB Technique Developments

Characterization of the metric and topologic properties of the cathode microstructure is an important area of study. Microstructure properties can be optimized during the fabrication processes, and the optimized microstructure properties can improve cathode performance by affecting kinetics of the oxygen reduction mechanism that occurs on the cathode side. The FIB automated serial-sectioning techniques provide opportunities for characterizing the bulk metric properties and topologic properties of the cathode microstructure on micron scale. FIB sample preparation techniques, which have been developed, also enable characterization of the interfacial metric properties of the cathode/electrolyte interface on the atomic scale. The study of the geometric properties of the cathode microstructure brings a new angle to the understanding of the dependence of the cathode polarization on the geometric properties of the cathode microstructure on both micron and atomic scales.

Although FIB/SEM enables to characterize effectively the geometric properties of the cathode, it is a site-specific characterization tool. This limitation of FIB/SEM has been overcome by combining FIB/SEM with the classical and advanced stereology. In order to offer unbiased quantification of geometric properties of the SOFC microstructure, for this reason, FIB/SEM automated serial-sectioning techniques have been developed to statistically characterize microstructure feature in 2-D combining with stereology. The homogeneity of topological properties of the cathode has been explored by the disector analysis coupled with the T-test. The optimized number of the cross-section images for 2-D microstructure property analysis, and of the plane-view images for 3-D microstructure quantification were decided. The optimized numbers ensure unbiased quantification of geometric properties of the sintered SOFC samples on the micron scale. A new method of preparing TEM cross-sectional sample of the LSM/YSZ interface by FIB and Omniprobe manipulator appears to work well for so porous microstructure of the cathode. This technique allows study of the initial stages of LZO formation by using the TEM/EDS analysis. The kinetics study of the LZO formation clarifies the delay of the LZO formation predicted in previous thermodynamic studies. In addition, this technique opens a brand-new research field: the study of contributions of the LZO phase formation to the cathode activation polarization and cathode ohmic polarization.

6.1.2 Dependence of the Activation Polarization on the Metric Properties

It is well-known that TPB length has been the most crucial metric properties, which affect the interfacial reactions between the cathode and the electrolyte. Kinetics of the interfacial reactions dominates the performance of the SOFC. However, diverse relationships between the interfacial resistance and the L_{TPB} complicate the understanding of the charge transfer reaction. Different conclusions are ascribed to the biased quantification of the TPB length, and to its dependence of the overall polarization resistance instead of the individual charge transfer

resistance. It is clear that in literatures, the LZO phase formation has been discounted by ignoring the attributions of the LZO phase to the interfacial resistance.

Based on unbiased analyses of the cathode and interfacial microstructure, a comprehensive investigation of the impact of TPB length on the charge transfer resistance was performed. Both the isochronal and the isothermal sintering studies showed that specific metric properties of the microstructure affect the kinetics of the corresponding possible rate limiting steps, thus they influences the corresponding components of the activation polarization. Decreasing of the TPB length increases the charge transfer resistance. Densification of the microstructure dramatically reduces the available TPB boundary area for the charge transfer reaction. Charge transfer resistance increases because effective active sites for charge transfer reaction are dramatically reduced. In addition, isolated pores inhibit transport of oxygen molecules or diffusion of the oxygen intermediates to reaction sites at the LSM/YSZ interface. The dissociative adsorption resistance is increased as the pore surface area is reduced. This can be explained by the fact that the growth of pores results in the decreasing of the pore surface area. Pore area determines the area exposed for dissociative adsorption of oxygen and therefore affects the cathode activation polarization.

Dramatic changes in the charge transfer resistance as well as the dissociative adsorption resistance were observed in the isochronal sintering between 1200°C and 1300°C. The isothermal sintering study of 1200°C suggests that dramatic changes in the activation polarization are caused by the LZO phase formation. Although it was not considered in previous studies, LZO phase varies the activation polarization with different extents under different sintering conditions. This explains why conclusions about TPB length vs. charge transfer resistance are different. LZO phase hinders the transport of oxygen molecules or obstructs

diffusion of the oxygen intermediates to reaction sites at the LSM/YSZ interface. In other words, LZO phase covers some distance that the reaction zone extends beyond the TPB [110], thus reducing reactive zone area, in which charge transfer occurs. LZO phase increases an energy barrier, which oxygen reactant species must overcome before they arrive at TPB sites. After LZO formation, more activation energy is needed for the charge transfer and the dissociative adsorption reactions to occur. As a result, increasing the energy barrier of the reactions increases the activation polarization. In other words, insufficient amount of the reactant species result in the reduction in the reactions rate, thus increasing reaction resistances (both charge transfer and dissociative adsorption resistances).

It should be noted that the definition of the TPB length is modified due to the LZO phase formation at the cathode/electrolyte interface, therefore TPB length is not the only geometric factor that affects the charge transfer resistance. The isothermal sintering study allows a comparison between it and three models to study how charge transfer resistance is affected by geometric factors. Different effects of L_{TPB} on the charge transfer resistance were observed between Kleitz's model and my study. The power dependence of the charge transfer resistance contradicts Kuznecov's model on the product of the L_{TPB} and S_c . Kuznecov's and Kleitz's models assume that the oxygen reduction mechanism is controlled by the bulk diffusion mechanism. The controversy between my study and the two models suggests that the bulk-diffusion model is not applicable to explain the relationship between the activation polarization and the metric properties in this material. Diverse relationships between the interfacial resistance and the L_{TPB} are ascribed to neglect the effect of the LZO phase on the charge transfer resistance in previous work. The LZO phase formation at the cathode/electrolyte interface modifies the number of the effective active sites (the ideal definition of the TPB sites) for the charge transfer

reaction. The relationship between the TPB length and the charge transfer resistance with LZO phase formation is different from the case without LZO phase formation. Therefore, previous models report different conclusions about the effect of the TPB length on the charge transfer resistance from the experimental observations in my study.

6.1.3 Tertiary Phase

It is well known that for cathode materials with Sr<30mol%, the LZO phase was observed at the LSM/YSZ interface for co-sintering at temperatures higher than 1000°C. LZO phase degrades the cathode electrochemical properties due to its lower ionic conductivity than YSZ. It is very important to control the formation and the growth of LZO phase at an initial stage to improve electrochemical properties. Previous thermodynamic studies reported that LZO formation either can be avoided by reducing La composition down to 86mol% or not. Isochronal and the isothermal sintering studies in this work answered this question: La insufficiency in the LSM avoids or retards the LZO phase formation. These studies investigated the basic diffusion mechanism of an initial stage of the LZO phase formation and analyzed structural correlation between the LZO and the YSZ phase on the atomic scale. Structural analysis of the LZO phase growth at the LSM/YSZ interface on the atomic scale was related to the microstructure evolution at the LSM/YSZ interface on the micron scale. Thus, the result that the LZO phase changes cathode activation and ohmic polarizations on the micron scale is explained by the interruption of conduction and diffusion mechanism of reactant species for the oxygen reduction on the atomic scale.

The isochronal and the isothermal sintering studies on the kinetics of the LZO phase formation showed that changing in the ratio of A-site (La,Sr) to B-site (Mn) does not prevent but only delays the LZO formation. In other words, LZO phase cannot be avoided by only

decreasing the composition of La less than 86mol%. This conclusion has been confirmed by strong evidence. Rate constants of the LZO formation in low A-site to B-site ratio of LSM were lower than those of LZO phase in high A-site to B-site ratio of LSM under the same sintering conditions. It is possible that the decrease in A-site to B-site ratio stabilizes the LSM thus retarding LSM decomposition. Mn inhibits the decomposition of the LSM. The less LSM is decomposed, the less amount of the La is supplied to reactions between the LSM and the YSZ. As a result, LZO formation is delayed. Therefore, La deficiency and Mn excess delay the LZO formation.

LZO phase polarization dominates the increasing of the activation polarization and the total ohmic polarization in the SOFC. Activation polarization (charge transfer resistance) show the same power dependence of the t_{LZO} in three oxygen reduction models. This is because the number of active sites for charge transfer reactions is reduced by increasing amount of LZO phase formed at the LSM/YSZ interface and by decreasing TPB length. In addition, LZO phase formed at the LSM/YSZ interface dramatically increases the charge transfer resistance by increasing the energy barrier for the reactions to overcome, thus the activation polarization increases. On the other hand, LZO thickness represents the effect of the LZO phase on reduction in supply of the oxygen reactant species from YSZ or LSM to the TPB. Supply of the oxygen is controlled by a surface diffusion mechanism. LZO phase reduces surface diffusion area in a close proximity to the LSM/YSZ interface. Surface diffusion of reactant species for the charge transfer reaction, especially surface diffusion of the oxygen ion/vacancy is blocked by the LZO phase.

The normalized LZO conductivity ($2 \times 10^{-6} \text{Scm}^{-1}$) calculated from the microscopic analysis is slightly lower than the LZO conductivity using electrochemical measurements. LZO

normalized resistivity represents the impact of the LZO phase on conduction mechanism of carriers. LZO reduces the rate of the electrons conducting from the LSM to the TPB. It blocks bulk diffusion of the oxygen vacancy away from the TPB to the YSZ. Because LZO electrical conductivity, $2e^{-6}\text{Scm}^{-1}$, is four orders of magnitude lower than that of YSZ, $1.3e^{-1}\text{Scm}^{-1}$, and seven orders of magnitude lower than that of LSM, 218.7Scm^{-1} at 1000°C . Resistance due to these deleterious effects contributes to increase the ohmic polarization.

6.1.4 Dependence of the Concentration Polarization on Topological Properties

The magnitude of the concentration polarization is at least 40% of the total cathode polarization. If gas transport process through the porous cathode is fast by optimizing geometric properties, then cathode polarization will be effectively controlled. Several SOFC models report that the effective diffusivity of $\text{O}_2\text{-N}_2$ (one of the gas transport properties) affects concentration polarization. However, the effective diffusivity of $\text{O}_2\text{-N}_2$ is quantified by a two-dimensional dusty-gas model. This dusty-gas model neglects changes in connections among pore channels and considers gas transport through the closed pores under sintering conditions. The inappropriate quantification of the geometric properties might cause inaccurate calculations of the effective diffusivity of $\text{O}_2\text{-N}_2$. In addition, only continuum diffusion domain is considered for the gas transport. This work calculated the geometric tortuosity using an elementary skeletonization model in 3-D FIB/SEM image analysis. This method of quantifying the geometric tortuosity of the porous cathode has never been tried before. In conjunction with two pore-network models (Mason's dusty-gas and Kopneon's lattice-gas models), the elementary skeletonization model is effective to study the fluid transport property (permeability) or gas transport property (effective diffusivity) of the oxygen. Then the cathode concentration polarization was associated with the gas transport properties of a porous cathode by applying Kim's SOFC performance model.

Two models with different assumptions on the major O₂ flux showed that the higher effective diffusivity or permeability, the faster kinetics of the gas transport is through the porous cathode, therefore the less resistance to the gas transport is. The ineffective gas transport through the porous cathode contributes to the starving of the oxygen, thus slowing down oxygen reduction on the cathode side. As a result, concentration polarization is increased by affecting kinetics of oxygen reduction. In the binary diffusion dominant regime, the gas transport resistance is not monotonically increased by increasing the logarithm of $\frac{\tau}{V_v}$. The assumption of the LSM grains as immobile particles in a porous matrix is not consistent with changes in connections among LSM grains. In addition, diffusion rate of the gas transport through the porous cathode is overestimated by introducing total porosity. On the other hand, in the viscous flux dominant regime, a direct relationship was observed between the permeability and the gas transport resistance as compared to the relationship of the effective diffusivity. It might indicate that the skeletonization and the lattice-gas models are more applicable to the study of the gas transport properties in a porous cathode with respect to the dusty-gas model.

6.2 Future Work

An initial stage of the LZO phase formation has been studied in an A-site deficient LSM. The 1/2 power dependence of the LZO thickness on the sintering time shows that LZO growth is controlled by a diffusion mechanism. The STEM-EDS analysis has been performed to study diffusion of the chemical species at the LSM/YSZ interface, thus determining where the initial LSM/YSZ is located. The STEM-EDS technique gives more accurate analysis of the diffusion than SEM-EDS. The latter collects characteristic X-rays from a larger interactive volume than the STEM-EDS. However, STEM-EDS provides semi-quantitative analysis of the diffusion mechanism at the LSM/YSZ interface. STEM-EDS could not accurately estimate the

composition of a trivial element (<1mol %). In addition, the capability of the STEM-EDS of detecting concentration change is limited by its lateral resolution. In other words, STEM-EDS is not effective to study diffusion in a region of less than 15nm. If quantitative chemical composition of materials is known, then the question that LZO phase formation is controlled by either the uniaxial diffusion of La and Mn into YSZ or interdiffusion between LSM and YSZ will be answered. In other words, location of the initial interface of the LSM/YSZ will be determined. Atomic probe tomography is an effective tool that will be used to study quantitatively the diffusion mechanism of chemical species at the LSM/YSZ interface at the early stage of the LZO formation. Because its detection limit of the chemical composition is less than 0.1mol %, and its lateral resolution is about 5Å. In addition, LZO thickness of 30-80nm fits well with the scale of the 3-D microstructure feature that atomic probe can effectively characterize [170].

It has been confirmed that LZO growth degrades cathode activation and cathode ohmic polarizations by changing reaction mechanism and conduction mechanism at the LSM/YSZ interface. This is the conclusion based on the study of the initial stage of the LZO formation (<20h). However, SOFC lifetime is longer than few tens of hours. It is important to know whether or not the LZO phase consistently degrades cathode polarization under the long-term operational condition. In other words, it is still not clear if the degradation rate of the cathode polarization is dependent or independent of the sintering time. Some research show that LZO phase disappears when atmosphere of the inside LSM/YSZ interface becomes more reductive than that of the surface along TPBs [36-38]. Improvement of the TEM sample preparation technique becomes important for a study of LZO phase under a sintering time of longer than 20h. TEM sample preparation becomes challenging because contact area between the LSM and the

YSZ dramatically decreases with the increasing sintering time. Continuous pore channels at the interface make connections between the LSM and YSZ fragile. Impregnation of epoxy in samples might reduce challenges of making a TEM sample. Epoxy will increase connections between the LSM and the YSZ. In addition, if low electron-beam energy and low current of Ga ion beam are used, then the epoxy, which is filled in pores between the LSM and YSZ layer, might protect YSZ layer from Ga ion beam milling at the epoxy/YSZ interface.

Tortuosity has been quantified based on more than one thousand of FIB/SEM plane-view images. Image processing, especially the segmentation and the image threshold steps are time consuming. Segmentation and image threshold determine the accurate quantification of geometric properties. Inaccurate segmentation and image threshold cause loss of the skeleton's reproducibility of the 3-D pore space to the original object. Over-threshold and under-segmentation were avoided by manual operation, because auto-threshold and auto-segmentation functions lose some of the original images and increase errors of the skeletonization process. However, manual threshold and segmentation steps are labor intensive. A subsidiary model which is capable of optimizing and homogenizing threshold is necessary to be developed. It can save time and provide high-quality images. An accurate quantification of the geometric properties depends on effective reduction in image artifacts.

The elementary skeletonization model has limited usage in the study of the gas transport properties. An advanced skeleton model should be developed to analyze gas transport efficiency within the porous cathode. This model will reconstruct the flow field using radii of pore throats as well as the distribution of pore throats as inputs of the model, which were calculated from the elementary skeletonization model. The advanced model will simulate skeleton of a 3-D pore-network to test the accuracy of the elementary skeletonization model. In addition, main flow

channels (pore throats with wide opening) will be determined based on comparing the radii of pore throats as well as the distribution of pore throats to one another. Then the frequency of main flow channels through which gas transport can be estimated. The distribution of the main flow channels will determine the gas transport efficiency within the porous cathode.

APPENDIX A FIB MANUAL

Part one: TEM sample preparation manual

Prepare samples:

A. make trenches (Figure 3-5 in section 3.2)

1. regular mount ,polish cross section [I= 5000pA, 45×6um(// to the cross-section)]
2. rotate 180°, deposit Pt to cover both LSM and YSZ [I=300pA, 15×2.2 (⊥interface)×1.8um (thickness of Pt)]
3. make two trenches on both front and back sides[I=5000pA, 19×22 (⊥interface) × 3um(//interface); polish the left side by bulk milling box (□), which will touch Cu-grid [1000pA, 20um×1um (⊥interface) ×4um (//interface); repeat polish with the same para but step milling box (Π); make a small notch on left corner, which will touch Cu-grid [1000pA, 9um×0.5um(⊥interface) ×z=2um (//interface)]
4. rotate 180°, Pt deposition on side [300pA 9×2um (//interface)×0.5 (thickness of Pt)]
5. undercut the sample at 9um depth (// interface) [5000pA, 3×1 um(// interface)×3 um (⊥interface)]

B. release sample (Figure 3-5 in section 3.2)

Mount ion beam perpendicular to cross-section, rotate relatively -90°, t=10° to undercut from the side (//interface but with a angle), put the undercut box on the edge of the trench box in A3 [1000pA, 25×0.8 um (⊥ interface) ×5-8um(// interface), check complete undercut [t=30-40° under E-beam], switch to E-beam from Ion-beam

C. Mounting Cu-grid (a good way to mount sample when transfer omni-sample to the Cu-grid)

1. before FIBbing Cu-grid, put screw down and touch the table, put sample on right wing with the "o" close to middle screw, the order of the right wing of the Cu-grid like "O" A-B-C (B-front away from me)
2. put Cu-grid inside FIB column: put screw inside, Cu-grid is ⊥ to ion beam, the order of left wing of the Cu-grid, which holds the sample, like C-B-A"O"-screw(inside)-right wing (empty) . Under ion beam see left C-B-A"O"right image. The sample on B finger is toward away from operator
3. take out of Cu-grid after sample preparation, attach "o" on the right side by the vacuum twizzer, lie down sample with "o" on the right side into sample holder. In order to protect from touching sample before TEM imaging and to avoid the broken sample

D. prepare Omni-Cu grid:

1. mount Cu grid // to ion beam and inward screw (on the right), image shows the order like A finger -B finger -C finger ,Screw, Empty
2. $t=52^\circ$, put the milling box 5um away from the middle of B finger, mill the side of B finger(toward A of Cu grid) [5000pA, Z=2 um (//side of B finger)~ real depth of 22um), polish side edge with clean-box. This step to polish corner of the Cu-grid, which will touch one side of the sample
3. mount Cu grid \perp to ion beam and inward screw(on the left)& "O" close to middle of B finger, image shows the order like screw-O-ABC, B front is away from the operator. It is easy to put sample attached with Omniprobe

E. final thinning: (Figure 3-5 in section 3.2)

1. touch hole side of the Cu-grid by vacuum tweezer; mount Cu grid \perp to ion beam and inward screw(on the left), it is good to see front of the B finger
2. find \perp angle 1° (close to $t=52^\circ$), mill bottom side of the sample first (\perp angle $1+1^\circ$) [1000pa, $x=1/7$ real depth]; then mill top side of the sample (\perp angle $1-1^\circ$) [1000pa, $x=1/7$ real depth]
3. mill twice bottom side of the sample first (\perp angle $1+1^\circ$) [300pa, $0.5 \times z1=1$ (real 9um), then mill twice top side of the sample (\perp angle $1-1^\circ$) [300pa, $0.5 \times z1$]; it should be noted that mill bright part first (bottom), then mill dark part (top)
4. measure thickness at \perp angle 1 ; mill bottom side first (\perp angle $1-1$) [100pa, $0.22 \times z1=2.2$ (real 9um), then mill top side (\perp angle $1+1$) [100pa, $0.22 \times z1=2.5$]; until final thick 120nm. It should be noted that in the end, milling box could not touch dark region on the top of the sample
5. tips:
 - ion-emission current is $(2-6) \times \text{area}$; ion-milling depth: $\sim 1/4-1/5$ of the real depth for milling bulk; $\sim 1/6-1/7$ of the real depth for milling edge
 - align x in inverse direction = rotate 180 as origin of +, align y at horizontal pos = rotate 90 as origin of +
 - milling box should be at bright region. because dark region means top surface of the sample
 - when sample is bent, do not mill just stop. because other cathode part will drag cathode part at the interface and finally either peel off cathode at the cathode/electrolyte interface or bend cathode behind the cathode/electrolyte interface

Part two: Omniprobe-TEM sample lift-out

A. Preparation work:

Cu-grid:

Mill the side of finger B (toward A) from top [I=5000pA, z=3um] and two other milling boxes at corner of the Cu-grid [I=5000pA, z=2um]

Trench sample (See part one A)

B. move omniprobe close to region of interest in sample

1. mount sample in a way that I-beam is \perp to cross-section of the sample at 7° tilt, heat Pt. Use SED detector for both I-beam and E-beam
2. $t=7^\circ$ with 45 degrees of the sample holder, move region of interest in sample to center of the screen and adjust eucentric under E-beam and align x under I-beam
3. start omniprobe software with PD: prober, press "VEL mode", "StageFOR" tilt angle "52"
4. pick omniprobe in first and Pt needle in with lowest mag of E-beam, try to move omniprobe center of the screen with either I-beam $\leftarrow X \rightarrow$ and $\begin{matrix} \uparrow \\ \Downarrow \end{matrix} Y$ or electron beam $\begin{matrix} \uparrow \\ \Downarrow \end{matrix} z$ -button and $\leftarrow X \rightarrow$ with high speed of 60um/s (because e-beam z and x as reference, from the e-column angle; i-beam x and y as reference, from the i-column angle)
5. move omniprobe close to region of interest (key step one) +mag, under E-beam " $\begin{matrix} z \\ \Downarrow \end{matrix}$ -button" down with 30um/s; +mag to 1000X, F11 switch to I-beam, and $\leftarrow X \rightarrow \begin{matrix} \uparrow \\ \Downarrow \end{matrix} Y$ moves right under I-beam with 1000X, and under E-beam " $\begin{matrix} z \\ \Downarrow \end{matrix}$ -button" with +2000X. now E-beam and I-beam mag-coupled. Under E-beam " $\begin{matrix} z \\ \Downarrow \end{matrix}$ -button" down with 0.5um/s, F11 switch to I-beam with $\leftarrow X \rightarrow \begin{matrix} \uparrow \\ \Downarrow \end{matrix} Y$ down with 0.5um/s; then F11 switch to E-beam, under E-beam with 2500X " $\begin{matrix} z \\ \Downarrow \end{matrix}$ -button" down with 0.5um/s; +mag 3500X and 6500X with E-beam " $\begin{matrix} z \\ \Downarrow \end{matrix}$ -button" down to try to move omniprobe as close as possible to region of interest of the sample
6. Pt needle in, reshape omniprobe tip with a milling box 100pa (0.64 \times 1.26 \times 1um)
7. touch sample (key step two): adjust focus to see both omniprobe and sample are at the same focused condition (=same height=same fwd). Switch between E-beam and I-beam by using F11 to confirm that omniprobe and sample are at the same height, with 10kx, move omniprobe to touch sample until see contrast change or alarm warning or sample movement.

In order to figure out how far omniprobe should be away from the surface under e-beam focus omniprobe tip, write down fwd1, then focus region of interest for sample, write down fwd2, fwd1-fwd2= distance between omniprobe and region of interest. When see contrast change, fwd1=fwd2. Detailed steps are as following:

- deposit Pt with Pt_tem.mtr 100pa, z=1um (remember this is important). Optimum Pt deposition time is 3mins.
- beam shift under i-beam and moves “+” close to “the part that will be milled”, mill a box to release top 6um from bulk sample [i=1000pa z=6um]
- omniprobe already attaches the sample, do not move stage, just use beam shift
- move omniprobe up to see whether the omniprobe with sample moves up, if it does, move omniprobe up and away. Omniprobe go to park, omniprobe out, Pt needle out, beams off, t=0 degree.

C. transfer sample from omniprobe to Cu-grid

1. mount Cu-grid parallel to the ion beam and screw inward (on the left of the Cu grid) $\frac{C B A}{\quad}$ in the unscrewed gap; adjust eccentric and link the beam with t=52; with 118x park; put omniprobe in, check “vel, stagefor, t=52”, 40um/s.
2. 220x t=52°, put Pt needle in, move omniprobe down; switch fl1 e-beam to i-beam in order to check position of the omniprobe (with sample) and Pt needle (to avoid omniprobe crash with Pt needle)
3. 2500x e-beam, then fl1 switch to i-beam, under i-beam to observe confocal plane in order to adjust omniprobe (attached with sample) with the same height as the top surface of the Cu-grid; fl1 check with e-beam; +5000x, repeat the same thing
4. get the same confocal plane of the omniprobe (attached with sample) and of the top flat surface of the Cu-grid (key step three): +10kx, find the difference of 2.5 turns between the focused state of the omniprobe (with sample) higher than the focused state of the top flat surface of the flat Cu-grid. (note: fine focus counterclockwise is for focused state at the higher position); fl1 switch to i-beam with z moves down 0.5um/s; check that 0.5 turns difference between the focused state of the omniprobe (with sample) higher than the focused state of the top flat surface of the flat Cu-grid; finally there is no difference in turns between the focused state of the omniprobe (with sample) higher than the focused state of the top flat surface of the flat Cu-grid
5. move omniprobe (with sample) to the top flat surface of the flat Cu-grid until the sample touches with the Cu-grid with contrast change; mill 100pa some sample materials on top/Cu-grid interface, using the redeposition to hold sample and Cu-grid; deposit Pt along contacted region between sample and contacted Cu-grid with 100pa z=2um; mill Pt from the contact region between omniprobe and sample with 100pa z=1um, (this is consistent with deposited depth of the Pt during attachment.)

6. solve the issue when Pt is deposited between Cu-grid and sample, but sample is milling away. Because sample height is higher than Cu-grid, then Pt needle is in the way, therefore, only Ga ion mills materials. (theory: during milling process, valve is closed, only Ga ion functions; during depositing process, valve is open, both Pt and Ga function), solutions are as following:

- move omniprobe far away, go to park position, then omniprobe out. (Fine focus counterclockwise is to move the confocal plane up (higher position);counterclockwise z-stage to move the stage down
- mount Cu-grid in the horizontal holder, try to perpendicular in the gap of the holder: if the angle between the perpendicular. Cu-grid top flat surface and the perpendicular sample top surface is small, Cu-grid top flat surface can be used as the reference plane to manually thin, that is, I-beam is perpendicular to Cu-grid top flat surface; if the angle between the perpendicular Cu-grid top flat surface and the perpendicular sample top surface is large, sample top flat surface can be used as the reference plane to manually thin, that is, I-beam is perpendicular to sample top surface.

Part three: FIB Auto-slice-view

A. Preparation

1. vent, put sample in, calibrate height of sample by the scale -take the scale out of FIB
2. pump ($7.5e-5$), source, beams on, close N_2 cylinder.
3. adjust eccentric height
4. low mag (1kx), find feature, focus,align stage, mouse double-click feature.(+)
5. 10° tilt, focus, z rotate + back to initial position; 0° tilt, focus, mouse double-click ,+ at initial position, 52° tilt, focus,z rotate + back to initial position; 0° tilt, focus, mouse double-click ,+ at initial position, High mag (10kx) repeat ,ion-electron beam coincidence electron beam, 52° tilt , focus, mouse double-click feature.(+=position a); low ion beam scan (100pA),focus, zero beam stage, beam shift x&y, (+ is coincided with position a under electron beam) perpendicular angle θ ,tilt θ around 52° , focus, ion beam see edge of top view; tilt ($\theta-52$), focus, electron beam see edge of top view

B. Pt deposition

Pt on, wait till $40^\circ C$, draw a rectangular box A close to the edge, Pt_tem file (x,y,z= $0.5\sim 1.5\mu m$), ion current= ($2\sim 6$) \times deposit area

C. FIB ion-beam milling

1. tilt θ , adjust brightness and contrast, focus, draw a (U) box B around box A, Si file(x,y,z= $5\sim 10\mu m$), high ion current(1K \sim 5KpA), rough milling
2. draw a (U) box C around box A, focus, Si file(x,y,z= $3\sim 8\mu m$), low ion current(300 \sim 100pA), fine milling

D. serial-sectioning

1. draw a rectangular box D close to front edge of box A, focus, Si file(x,y,z=1~3um), low current(300~100pA) first serial sectioning, observe real milling depth, adjust z to be the exact um)
2. open auto-slice-view software, beam shift correction, image save folder and directory, x,y=z in a , z total and No. slices. Ion beam current, low Image scan rate.
3. run software, beam shift X&Y, milling box at the right start position

E. copy image

rodiox CD creator, record

F. shut off

1. Pt off, beams off, open N₂ cylinder, vent
2. take sample out
3. pump, close N₂ cylinder

Part four: AutoFIB

A. in-situ

1. repeat part three A and B
2. Pt on, wait till 40°C, find feature, focus, run autoFIB
3. run script 6, continue, input width 10um, z=4um, Pt=1um, final thick 200nm, new, finish, all.
4. run script 1, “do not move stage to the stored position”, adjust focus when software could not find fiduciary mark, continue, (note: if fiduciary mark is invisible, check magnifications: undercut at low mag; other processings at high mag. When do undercut, we need ion-beam shift x and y to make drawn box at the right position of the milled trench).
5. cancel undercut, note absence of Pt, stop two cuts before finish.
6. follow step F1, take sample out

B. ex-situ lift out

1. check needle and exchange broken needle
2. unscrew top loose, mark the middle of the plastic one, vertically insert one plastic one, let the mark in the middle of the spring and screw tightly.
3. turn power on; temperature is 24.8 degree, press start, then wait until temp is decreased from 62 degree to be 24.8 degree. Unscrew loose, then take the bottom needle tip out.

4. install the plastic needle starting from the bottom part to the tip part; install it onto the needle holder.
5. exchange needle tip
6. insert the needle tip and screw the needle tip.
7. put sample stub on a sample holder and put a Cu grid on another sample holder all by vacuum twizzer
8. turn on microscope and monitor
9. low mag, move sample to center of screen and put right needle at center of screen above sample (Note that center of screen is like a reference point)
10. low down right needle more, focus on needle, repeat until the needle is really low; slightly low down the right needle, focus needle, low needle until both needle and sample are visible. (Use high magnification). Move knob to adjust right needle until it touches the sample, (wait for few seconds until attraction between the sample and the needle are strong) pick up the sample. (now sample is attached on the needle)
11. raise up the right needle a little bit
12. move sample holder with Cu grid below the needle. Focus Cu grid and find a slot around center of the Cu grid. Make the slot stay in center of screen.
13. Slightly low down the right needle, focus on the right needle until both right needle and slot are focus. Try to release sample from the right needle.
14. Use the left needle, low more down left needle at the beginning, then focus left needle, and slightly low down left needle+focus left needle until two needles are at the same height. Move knob to adjust left needle until it touches the sample, make a good adjustment until sample is well oriented. Or sample is transferred from the right needle to the left needle.
15. slightly low down the left needle until it touches the slot, then release it. Try to make sample flatly lie down in the middle of the slot in Cu grid.
16. raise one needle up at one time, make sure both needles stay at center of the screen.
17. turn off monitor and microscope
18. vacuum twizzer takes Cu grid and slide close to the TEM sample holder.

Part five: matlab script for calculation of length of branches

Code A

```
clear all;
close all;
[dummy, filename]=xlsread('datafilename.xls');
fileindex=size(filename);
for i=1:fileindex(1)
    [linelength, totallength]=lengthcalc(char(filename(i)));
    linelength=[linelength totallength];% this is to attach total
length to the end of line length

xlswrite('processeddata.xls', linelength, 'Sheet1', strcat(char(64+i), '1
'));
end
```

Code B

```
function [linelength, totallength]=lengthcalc(tempname)
tempdata=dlmread(tempname);%this is used to load all data in
datasize=size(tempdata);%this is to get how many data points in this
file
tempj=0;%tempj is used to record how many lines you have
templinelength=0;%this is used to initialize this variable
linelength=0;
totallength=0;

for tempi=1:datasize(1)-1
    if tempdata(tempi+1,1)==tempdata(tempi,1)
        temppointdistance=sqrt((tempdata(tempi+1,2)-
tempdata(tempi,2))^2+(tempdata(tempi+1,3)-
tempdata(tempi,3))^2+(tempdata(tempi+1,4)-tempdata(tempi,4))^2);
        templinelength=templinelength+temppointdistance;
    else
        tempj=tempj+1;
        linelength(tempj)=templinelength;
        totallength=totallength+templinelength;
    end
end

tempj=tempj+1;
linelength(tempj)=templinelength;
totallength=totallength+templinelength;
```

APPENDIX B
ELECTROCHEMICAL PROPERTIES AND SCANNING TRANSMISSION ELECTRON
MICROSCOPY- ENERGY-DISPERSIVE X-RAY SPECTROMETRY (STEM-EDS)
CONCENTRATION PROFILES

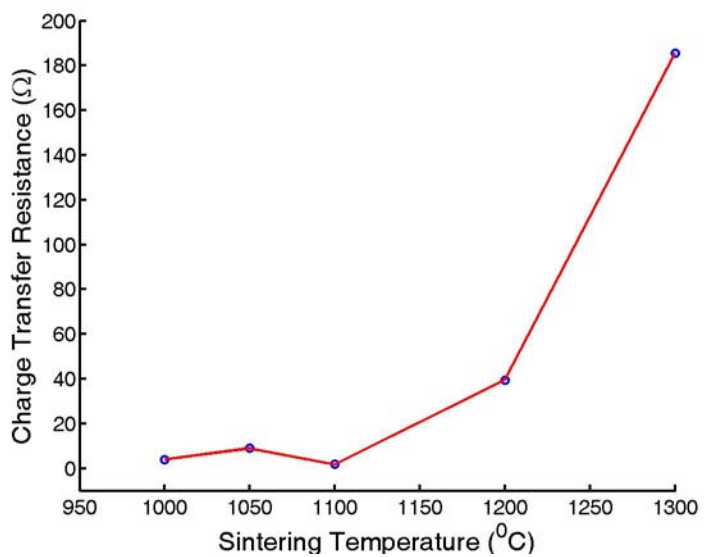


Figure B-1. Charge transfer resistance of the isochronal sintered samples

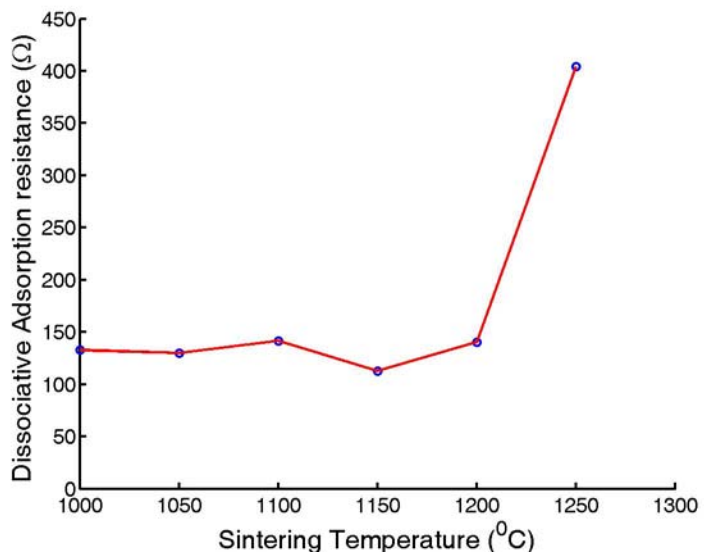


Figure B-2. Dissociative adsorption resistance of the isochronal sintered samples

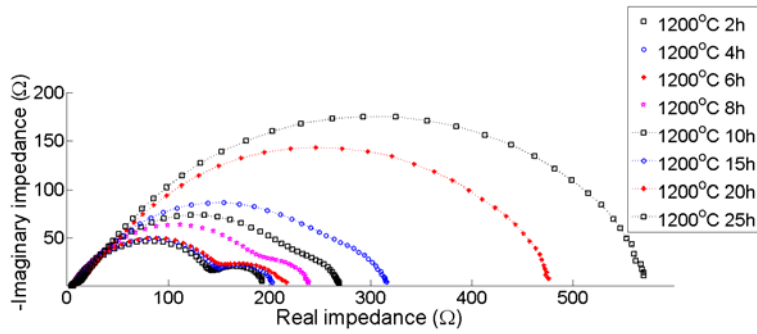


Figure B-3. Nyquist plot of the isothermal sintered sample

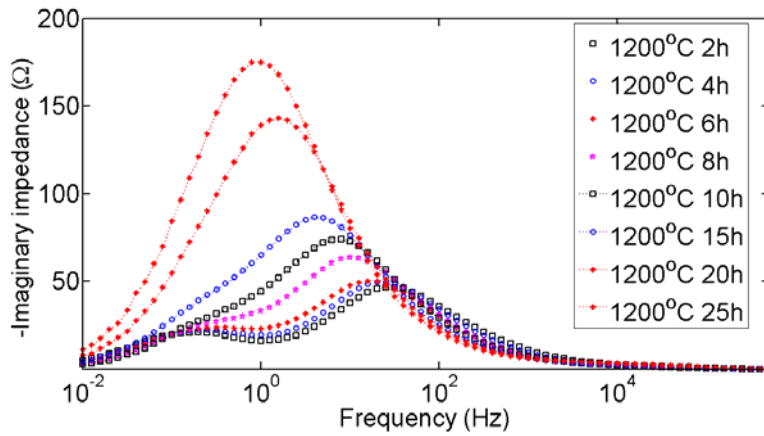


Figure B-4. Bode plot of the isothermal sintered sample

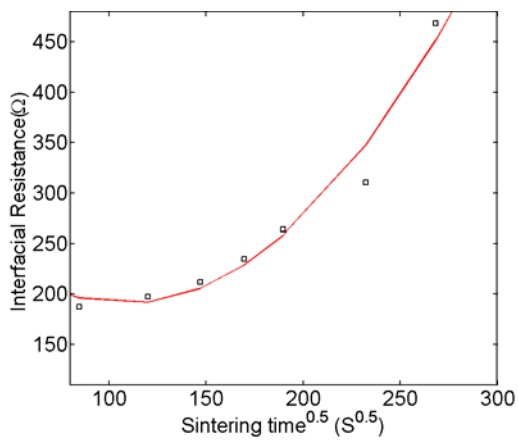


Figure B-5. Interfacial resistance of the isothermal sintered samples

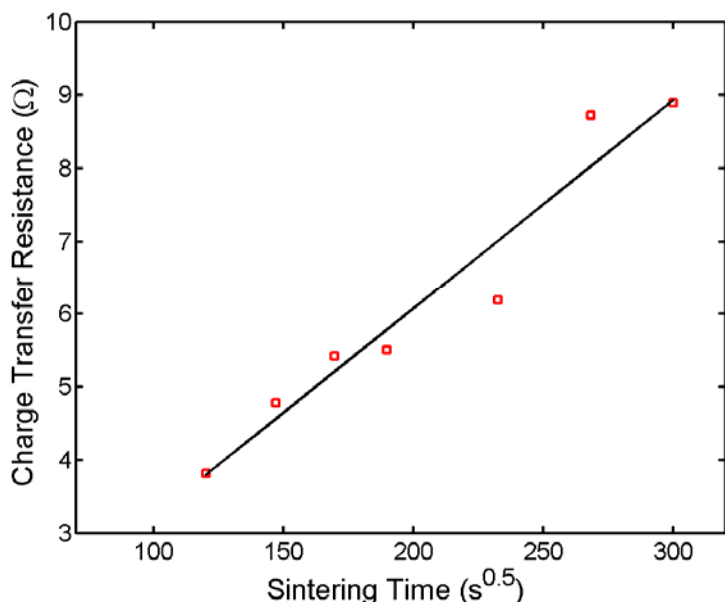


Figure B-6. Charge transfer resistance of the isothermal sintered samples

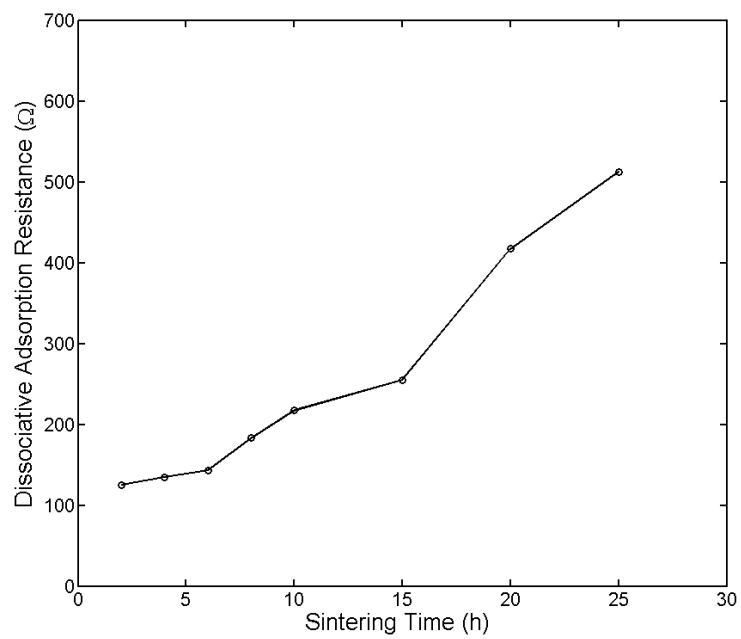


Figure B-7. Dissociative adsorption resistance of the isothermal sintered samples

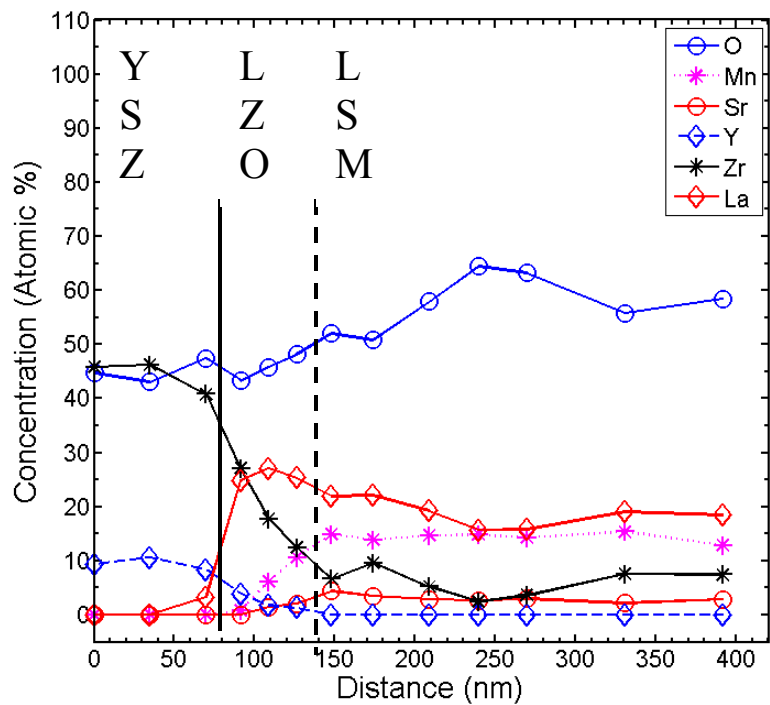


Figure B-8. STEM-EDS of 12002h

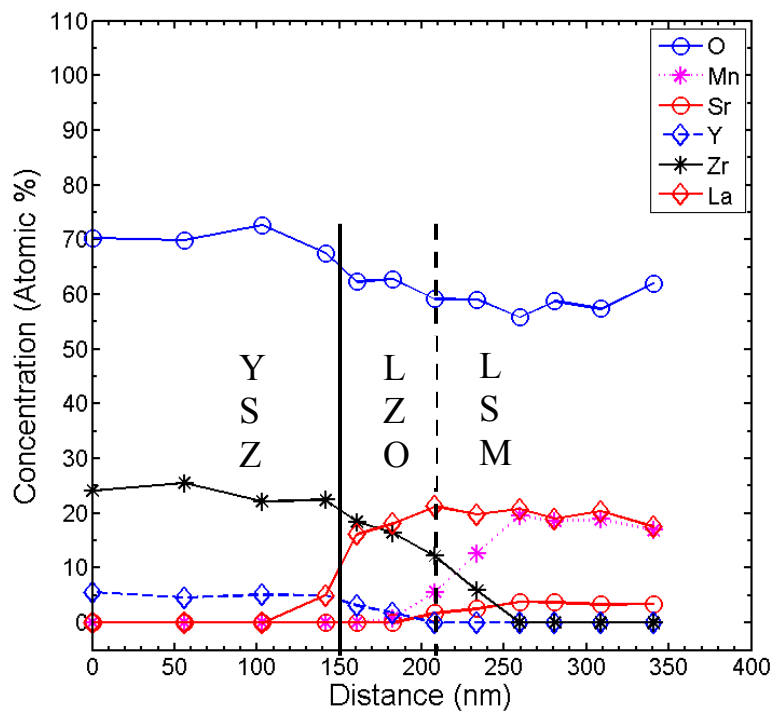


Figure B-9. STEM-EDS of 12004h

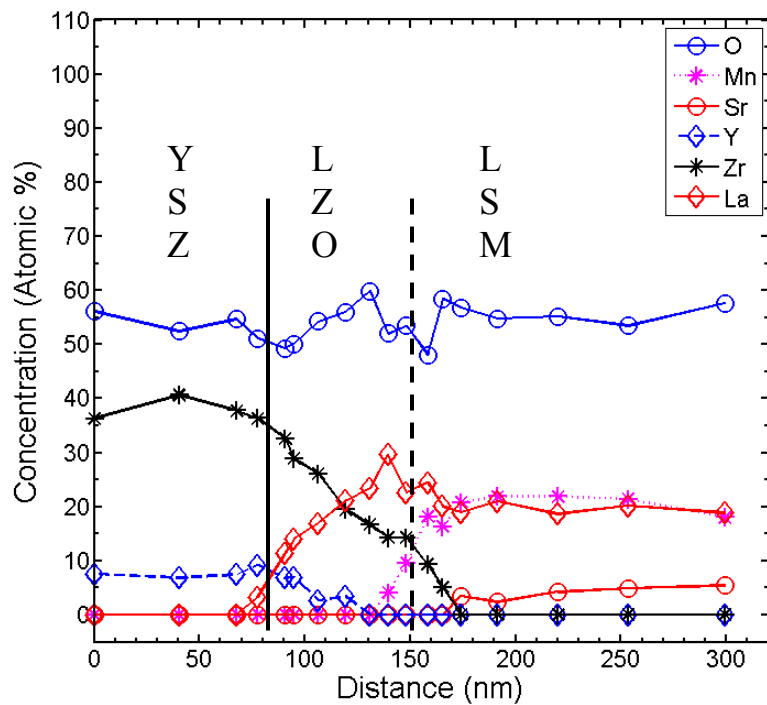


Figure B-10. STEM-EDS of 12008h

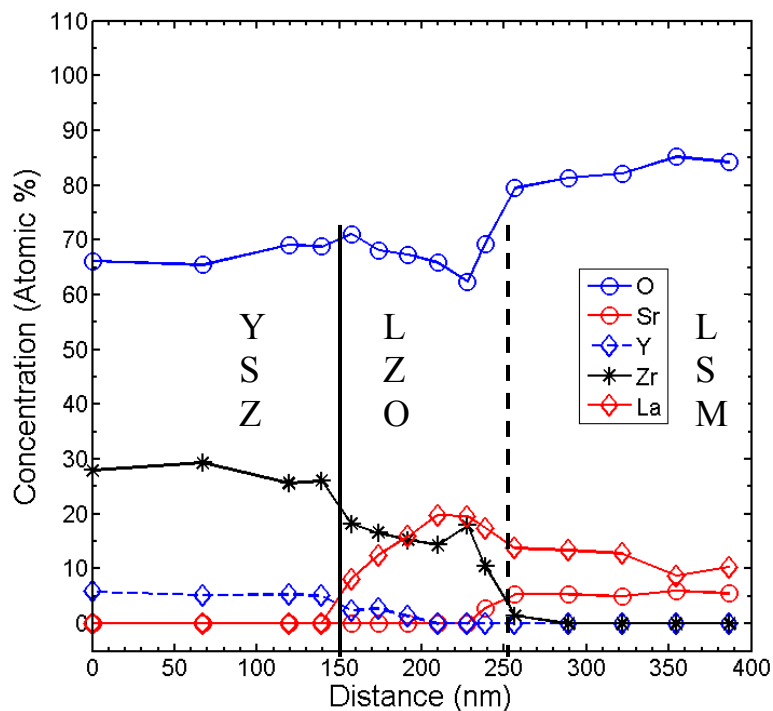


Figure B-11. STEM-EDS of 120015h (Note no Mn)

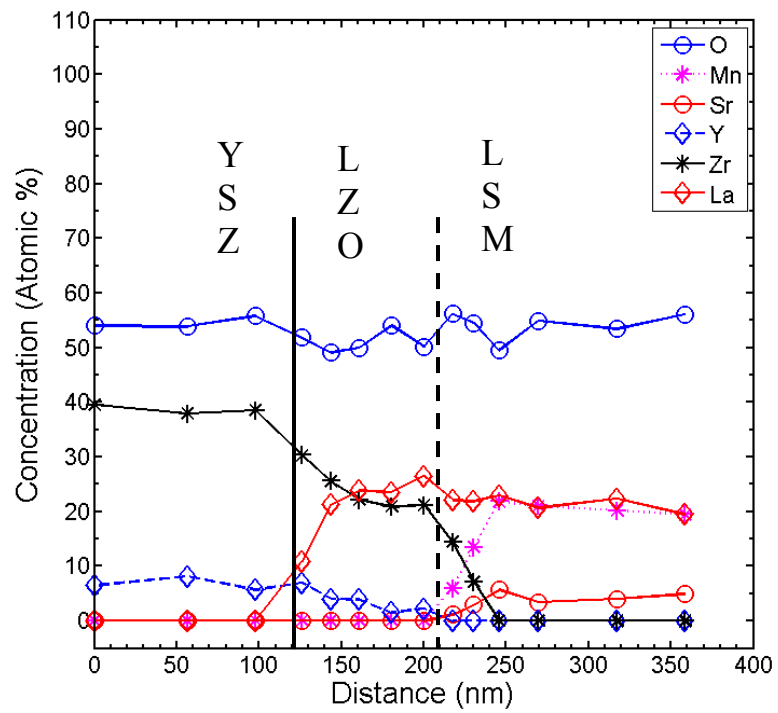


Figure B-12. STEM-EDS of 120020h

APPENDIX C
GEOMETRIC PROPERTIES OF THE ISOTHERMAL SINTERED SAMPLES

Table C-1. Geometric properties of the isothermal sintered samples

Time (h)	S_C (μm^2)	C_V	t_{LZO} (nm)	L_{TPB} (nm)	V_V (%)
2	0.34	0.79	37.46	732.03	46.8
4	0.37	1.00	43.13	867.66	42.4
6	0.38	0.86	55.29	920.11	40.00
8	0.39	0.73	57.02	803.52	39.20
10	0.41	0.46	57.46	877.54	35.90
15	0.44	0.66	68.54	627.11	30.65
20	0.46	0.47	72.39	500.17	28.68
25	0.47	0.49		416.78	26.39

LIST OF REFERENCES

- [1] G. Caruso, Annual Energy Outlook 2008, (2008)
- [2] S.C. Singhal, MRS Bull. 16 (2000) 25.
- [3] N.Q. Minh, J. Am. Ceramic. 76 (1993) 563.
- [4] J. Mizusaki, H. Tagawa, K. Tsuneyoshi and A. Sawata, J. Electrochem. Soc. 138 (1991) 1867.
- [5] A.V. Virkar, J. Chen, C. W. Tanner and J. W. Kim, Solid State Ionics 131 (2000) 189.
- [6] A. Mitterdorfer and L. J. Gauckler, Solid State Ionics 111 (1998) 185.
- [7] C. T. Yang, W. J. Wei and A. Roosen, Journal of the American Ceramic Society 87 (2004) 1110.
- [8] K. Yang, J.H. Shen, K.Y. Yang, I.M. Huang, K.Z. Fung and M.C. Wang, J. of Power Sources 63-67 (2006) 159.
- [9] E. Baur and H. Precis, Z.Elektrochem. 43 (1937) 727.
- [10] W.Nernst, Z.Elektrochem. 6 (1899) 41.
- [11] Department of Energy, The Solid State Energy Conversion Alliance Report, (2005).
- [12] Department of Energy, Fuel Cell Handbook, Seventh Edition (2004).
- [13] J.W. Kim and A. V. Virkar, Journal of The Electrochemical Society 146 (1999) 69.
- [14] A.J. Appleby and F.R. Foulkes, Fuel Cell Handbook, New York, Van. Nostrand Reinhold, 1989.
- [15] C.H. Hamann, A. Hamnett and W. Vielstic, Electrochemistry J. Wiley & Sons, New York, 1998.
- [16] J. ÓM. Bockris and A.K.N. Reddy, Modern Electrochemistry Kluwer Academic-Plenum Press, New York, 1998.
- [17] A. Scheidegger, The Physics of Flow Through Porous Media, University of Toronto press, Toronto, 1956.
- [18] A. Koponen, M. Ktaja and J. Timonen, Phy. Rev. E 54 (1996) 406.
- [19] J.H. Kuo, H.U. Anderson and D.M. Sparlin, J. Solid State Chem.87 (1990) 55.

- [20] A. Hammouche, E.L. Schouler and M. Henaoult, *Solid State Ionics* 28-30 (1988) 1205.
- [21] J.B. Goodenough, *Phys.Rev.* 100 (1955) 564.
- [22] J.F. Baumard and P. Abelard, *Advances in Ceramics, Vol.3, Science and Technology of Zirconia II*. Edited by N. Claussen, M. Rühle and A. Heuer, American Ceramic Society, Columbus, OH, 1984.
- [23] J. Mizusaki, N. Mori, H. Takai, Y. Yonemura, H. Minamiue, H. Tagawa, M. Dokiya, H. Inaba, K. Naraya, T. Sasamoto and T. Hashimoto, *Solid State Ionics* 132 (2000) 167.
- [24] K. Duncan, Y. Wang, S. Bishop, F. Ebrahimi and E.Wachsman, *J. Am. Ceram. Soc.* 89 (2006) 3162.
- [25] O.Yamamoto, *Electrochim. Acta.* 45 (2000) 2423.
- [26] S.C. Singhal and K. Kendall, *High Temperature Solid Oxide Fuel Cells: Fundamentals, Design and Applications*, Elsevier limited, Oxford, UK, 2003.
- [27] O. Yamamoto, Y. Takeda, R. Kanno and T. Kojima, in: *Proc. the International Symposium on Solid Oxide Fuel Cell*, Nagoya, Japan, (SOFC Society of Japan, Nagoya, Japan, November 13–14, 1989) p. 87.
- [28] S. B. Adler, *Chem. Rev.* 104 (2004) 4791.
- [29] J.M.Dixon, L.D.LaGrange, U.Merten, C.F.Miller and J.T.Porter, *J.Electrochem.Soc.* 110 (1963) 276.
- [30] D.W. Strickler and W.G. Carlson, *J. Amer.Ceram. Soc.* 48 (1965) 286.
- [31] J.J. Bentzen, N.H. Andersen, F.W. Poulsen and O.T. Sørensen, *Solid State Ionics* 28-30 (1988) 550.
- [32] W. Weppner, *Goldschmidt Inform*, 2 (1983) 16.
- [33] M. Filal, C. Petot, M. Mokchab, C. Chateau and J. L. Carpentier, *Solid State Ionics* 80 (1995) 27.
- [34] H. Yokokawa, *Annu. Rev. Mater. Res.* 33 (2003) 581.
- [35] T. Kawada, N. Sakai, H. Yokokawa, M. Dokiya and I. Anzai, *Solid State Ionics* 50 (1992)189.
- [36] D. M. Tricker, PhD dissertation, University of Cambridge, UK, 1993.

- [37] H. Yokokawa, T. Horita, N. Sakai, T. Kawada and M. Dokiya, in: Proc. First Eur. Solid Oxide Fuel Cell Forum, Eds. U. Bossel, Oberrohrdorf: Eur. Fuel Cell Forum 1994. p. 425.
- [38] A. Weber, R. Manner, B. Jobst, M. Schiele and H. Cerva, p. 473 in: High Temperature Electrochemistry: Ceramics and Metals, Eds. F.W. Poulsen, N. Bonanos, S. Linderoth, M. Mogensen and B. Z. Christianse, (Roskilde: RISØ National Laboratory, Denmark, 1996) p. 78.
- [39] M. J. Jorgensen and M. Mogensen, J. of the Electrochemi. Soc. 146 (1999) 2827.
- [40] M. J. Jorgensen and M. Mogensen, J. of the Electrochemi. Soc. 145 (2001) 433.
- [41] H.J. Vogel, European Journal of Soil Science 48 (1997) 365.
- [42] A. Koponen, M. Ktaja and J. Timonen, Phy. Rev. E 56(1997) 3319.
- [43] A. Koponen, M. Ktaja and J. Timonen, International J. Modern.Phy.C, 9 (1998) 1505.
- [44] R.E. Collins, Flow of Fluids through Porous Materials, Von Nostrand-Reinhold, Princeton, New Jersey, 1961.
- [45] A.E. Scheidegger, The Physics of Flow through Porous Media, 3rd Ed. Univ. Of Toronto Press, Toronto, 1974.
- [46] E. W. Washburn, Note on a Method of Determining the Distribution of Pore Sizes in a Porous Material in: Proceedings of the National Academy of Science 7 (1921) 115.
- [47] F. A. L. Dullien, Porous Media Fluid Transport and Pore Structure, 2nd Ed. Academic Press, Inc., San Diego, California, 1992.
- [48] S. Brunauer, P. H. Emmett and E. Teller, J. Am. Chem. Soc. 60 (1938) 309.
- [49] E.E. Underwood, Quantitative Stereology Addison Wesley, Reading MA, 1970.
- [50] J. A. Ruud, T. Striker, V. Midha and B. N. Ramamurthi, Ceramic Engineering and Science Proceedings. Columbus, 25 (2004) 251.
- [51] H. Song, S. Hyun, J. Moon and R. Song, Journal of Power Sources 145 (2005) 272
- [52] H. Fukunaga, M. Ihara, K. Sakaki and K. Yamada, Solid State Ionics, 86-88 (1996) 1179
- [53] J.C. Russ and R.T. DeHoff, Practical Stereology, 2nd Ed. Plenum Press, New York, 2000
- [54] N. Roberts, M. Reed and G. Nesbitt, Journal of Microscopy 187 (1997) 110.
- [55] R.T.DeHoff, J. Microsc. 131 (1983) 259

- [56] M.V. Kral and G. Spanos, *Acta Mater.* 47 (1999) 711
- [57] A.C. Lund and P.W. Voorhees, *Acta Mater.* 50 (2002) 2585.
- [58] J.E. Spowart, H.M. Mullens and B.T. Puchala, *JOM* 37 (2003) 35.
- [59] J. Wilson, *J. Micromech. Microeng* 12 (2002) 111.
- [60] B. Meyer, H.H. Hug and R. Bennewitz, *Scanning Probe Microscopy. The Lab on a Tip.* Springer, London, 2004.
- [61] L. Holzer, F. Indutnyi, P.H. Gasser, B. Munch and M. Wegmann, *J. Microscopy* 84 (2004) 216.
- [62] M.D. Uchic, L. Holzer, B.J. Inkson, E.L. Principe and P. Munroe, *MRS Bulletin*, 32 (2007) 408.
- [63] M.D. Uchic, M.A. Groeber, D.M. Dimiduk and J.P. Simmons, *Scripta Mater.* 55 (2006) 23.
- [64] J.J. Mulders, L. G. Knott and B.H. Lich, *Proc. Microsc. Microanal.* 12 (2006)1324 CD.
- [65] P.G. Kotula and M.R. Keenan, J.R. Michael, *Microsc. Microanal.* 12 (2006) 36.
- [66] J. R. Smith, A. Chen, K. L. Duncan, M. E. Orazem and E. D. Wachsman, *Electrochemical Society Transactions* 1 (2006) 243.
- [67] M.A. Groeber, *Mater. Charact.* 57 (2006) 259.
- [68] L.A. Giannuzzi and F A. Stevie, *Introduction to Focused Ion Beams: Instrumentation, Theory, Techniques and Practice*”, Spring Science+Business Media, Inc., New York, 2005.
- [69] F. Manconi, R. Markham, G. Cox, E. Kable and I. S. Fraser, *Micron* 32 (2000) 449.
- [70] D. Drobne, M. Millani, A. Zrimec, V. LeŠer and Z. M. Berden, *Journal of Microscopy* 219 (2005) 29.
- [71] D. C. Joy and C. S. Joy, *Micron* 27 (1996) 247.
- [72] J. Cazaux, *Journal of Applied Physics* 85 (1999) 1137.
- [73] K. Robertson, R. Gauvin and J. Finch, *Miner.Eng.* 118 (2005) 343.

- [74] J.I. Goldstein, D.E. Newbury, P. Echlin, D.C. Joy, A.D. Romig, C.E. Lyman and E. Lifshin, *Scanning Electron Microscopy and X-Ray Microanalysis*, Plenum Press, New York, 1992.
- [75] R. L. Gerlach and M. Utlaut, *Charged Particle Detection, Diagnostics and Imaging*, *Proceedings of SPIE*. 4510 (2001) 96.
- [76] B.J.Inkson, T. Steer, G. Möbus and G.T. Wagner, *J. Microsc.* 201 (2001) 256.
- [77] T.J.Steer , *Thin Solid Films* 413 (2002) 147.
- [78] M. W. Phaneuf, *Micron* 30 (1999) 277.
- [79] R. Krueger, *Micron* 30 (1999) 221.
- [80] V. G. M. Sivel, V. D. Brand, J. Wang, W. R., Mohdadi, H. Tichelaar, F. D. Alkemade and P. F. A. Zanbergen, *Journal of Microscopy* 214 (2004) 237.
- [81] R.T. DeHoff, *Curvature and the Topological Properties of Interconnected Phases*, *Quantitative Microscopy*, McGraw Hill Book Company, New York, 1968.
- [82] C.S. Smith and L. Guttman, *Trans. AIME* 197 (1953) 81.
- [83] S.A. Saltykov, *Stereometric Metallography*, Metallurgizdat, Moscow, 1958.
- [84] E.A. Mason and A.P. Malinauskas, *Gas Transport in Porous Media: The Dusty Gas Model*, Elsevier, Amsterdam, 1983.
- [85] E. L. Cussler, *Diffusion: Mass Transfer in Fluid Systems*, Cambridge University Press, Cambridge, 1995.
- [86] D.B.Williams and C.B. Carter, *Transmission Electron Microscopy*, 37 (1996) 371.
- [87] W.D. Callister Jr., *Materials Science and Engineering an Introduction*, John Wiley & Sons, Toronto, Canada, 1997.
- [88] A. J. Bard and L. R. Faulkner, *Electrochemical Methods Fundamentals and Applications*, 2nd Ed. John Wiley & Sons, Inc., New York, 2001.
- [89] J. Smith, Ph.D. Dissertation, University of Florida, 2007.
- [90] M.E. Orazem, *Journal of Electroanalytical Chemistry* 572 (2004) 317.
- [91] M. Orazem P. Shukla and M. Membrino, *Electrochimica Acta* 47 (2002) 2027.
- [92] H. Yokokawa, N. Sakai, T. Kawada and M. Dokiya, *Solid State Ionics* 40/41 (1990) 398.

- [93] S. K. Lau and S. C. Singhal, in: Vol.1–9 in Corrosion 85, The National Association of Corrosion Engineers (NACE) Meeting, Boston, MA, March 25–29, 1985. (National Association of Corrosion Engineers, Houston, TX, 1985) p. 345.
- [94] C. Clausen, C. Bagger, J. B. Bilde-Sorensen and A. Horsewell, in: Proceedings of the 14th Riso International Symposium on Material Science; F. W. Poulsen, J. J. Bentzen, T. Jacobseen, E. Skou and M. J. L. Ostergaard, Eds.(Riso National Laboratory: Roskilde,Denmark, 1993) p. 237.
- [95] C. Clausen, C. Bagger, J.B. Bilde-Sørensen and A. Horsewell, *Solid State Ionics* 70/71 (1994) 59.
- [96] S. P. Jiang, J. G. Love, J. P. Zhang, M. Hoang, Y. Ramprakash, A. E. Hughes and S. P. S. Badwall, *Solid State Ionics* 1 (1999) 121.
- [97] O. Yamamoto, Y. Takeda, R. Kanno and M. Noda, *Solid State Ionics* 22 (1987) 241.
- [98] F. W. Poulsen and N. Van der Puil, *Solid State Ionics* 53-56 (1992) 777.
- [99] T. Kenjo and M. Nishiya, *Solid State Ionics* 57 (1992) 295.
- [100] C. C. Chen, M. M. Nasrallah and H. U. Anderson, in: Proc. Vol. 4 Third International Symposium on Solid Oxide Fuel Cells, Eds. S. C. Singhal and H. Iwahara, (The Electrochemical Society: Pennington, NJ, 1993) p. 252.
- [101] H. Y. Lee and S. M. Oh, *Solid State Ionics* 90 (1996) 133.
- [102] R.V. Stuttgart, p. 110 in :F.N. Rhines, *Microstructology-Behaviour and Microstructure of Materials*, 1986.
- [103] H.E. Exner, *Image Anal Stereol* 23 (2004) 73.
- [104] K. R. Craig, *J. Microsc.* 95 (1972) 69.
- [105] T. Kenjo, Y. Yamakoshi and K. Wada, *J. Electrochem. Soc.* 140 (1993) 2151.
- [106] M. Kleitz, L. Dessemond, T. Kloidt and M. C. Steil, in: PV 95-1 Solid Fuel Cells II, Eds. M. Dokiya, O. Yamamoto, H. Tagawa and S. C. Singhal, (The Electrochemical Society Proceedings Series, Pennington, NJ 1995) p. 527.
- [107] M. Kuznecov, P. Otschik, P. Obenaus, K. Eichler and W. Schaffrath, *Solid State Ionics* 157 (2003) 371.
- [108] J. A. Labrincha, J. R. Frade and F. M. B. Marques, *J. Mater. Sci.* 28 (1993) 3809.
- [109] B.C.H. Steele, *Solid State Ionics* 75 (1995) 157.

- [110] S.B. Adler, J.A. Lane and B.C.H. Steele, *J. Electrochem. Soc.* 143 (1996) 3554.
- [111] M. Kleitz, L. Dessemond, H. Jimenez, F. Petitbon, R. Herbin and E. Marchand, in: *Proc. 2nd European SOFC Forum*, Eds. U. Bossel and B. Thorstensen, Pubi., Oberrohrdorf, Switzerland 1996, p. 443.
- [112] M. W. Barsoum, *Fundamentals of Ceramics, Series in Materials Science and Engineering*, McGraw-Hill, UK, 1997.
- [113] E. H. Aigeltinger and R. T. DeHoff, *Metallurgical Transactions A* 6A (1975) 1853.
- [114] N.Q. Minh, *Sci Technology Ceram*, 1995.
- [115] A.V. Berenov, *Solid State Ionics* 41 (1999) 122.
- [116] B.A. Boukamp, *Solid State Ionics* 31 (1986) 20.
- [117] M. Kuznecov, P. Otschik, N. Trofimenko and K. Eichler, *Russian Journal of Electrochemistry*, 40 (2004) 1162.
- [118] M. J. L. Ostergard, C. Clausen, C. Bagger and M. Mogensen, *Electrochimica Acta*. 40 (1995) 1971.
- [119] H. Yokokawa, N. Sakai, T. Kawada and M. Dokiya, *J. Electrochem. Soc.* 138 (1991) 2719.
- [120] M. Chen, A. N. Grundy, B. Hallstedt and L. J. Gauckler, *Computer Coupling of Phase Diagrams and Thermochemistry*, 30 (2006) 489.
- [121] H. Kaneko, H. Taimatsu, K. Wada and E. Iwamoto, In *Proc. Second International Symposium on Solid Oxide Fuel Cells*, Comm. Eds. F. Grosz, P. Zegers, S.C. Singhal and O. Yamamoto, (Eur. Communities, Bruxelles, Belgium 1991) p. 673.
- [122] H. Taimatsu, K. Wada, H. Kaneko and H. Yamamura, *J. Am. Ceram. Soc.* 75 (1992) 401.
- [123] C. Brugnoni and U. Ducati, M. Scagliotti, *Solid state Ionics* 76 (1995) 177.
- [124] J. A. M. Vanroosmalen and E. H. P. Cordfunke, *Solid State Ionics* 52 (1992) 303.
- [125] B.C.H. Steele, *Solid State Ionics* 86– 88 (1996) 1223.
- [126] A. Hammouche, E. Siebert, M. Kleitz and A. Hammou, in: *Proc. Electrochem. Soc.* 89-11 (1st. Int. Symp. Solid Oxide Fuel Cells, 1989) p. 265.
- [127] L. G. J. De Haart, R. A. Kuipers, K. J. De Vries and A.J. Burggraaf, *J. Electrochem. Soc.* 138 (1991) 1970.

- [128] T. Norby, O. J. Velle, H. L. Olsen and R. Thnold, in: Proc. Vol. 93-4, Solid Oxide Fuel Cells, Eds. S. C. Singhal and H. Iwahara, (The Electrochemical Society Proceedings Series, Pennington, NJ 1993) p. 473.
- [129] P. Fabry, M. Kleitz and C. Deportes, J. Solid State Chem. 5 (1972) 1.
- [130] M. Kleitz, L. Dessemond and T. Kloidt, in: Proc. 3rd Symposium on Solid Oxide Fuel Cells in Japan, (The Solid Oxide Fuel Cell Society of Japan, Tokyo 1994) P.35.
- [131] M.J.L. Østergaard and M. Mogensen, Electrochim. Acta 38 (1993) 2015.
- [132] M. Mogensen, S. Primdahl, J.T. Rheinlander, S. Gormsen, S. Linderoth and M. Brown, in: Proc. Vol. 95-1 Solid Oxide Fuel Cells (SOFC-IV), Eds. M. Dokiya, O. Yamamoto, H. Tagawa and S.C. Singhal, (The Electrochemical Society Proceedings Series 1995) p.657.
- [133] M. Suzuki, H. Sasaki, A. Kajimura, N. Sugijura and M. Ippommatsu, J. Electrochem. Soc. 141 (1994) 1928.
- [134] H. Sasaki, M. Suzuki, T. Sogi, A. Kajimura and E. Yagasaki, in: Proc. Vol. 95-1 Solid Oxide Fuel Cells (SOFC-IV), Eds. M. Dokiya, O. Yamamoto, H. Tagawa and S.C. Singhal, (The Electrochemical Society Proceedings Series 1995) p 187.
- [135] L. G. J. DeHaart, R. A. Kuioers, K. J. DeVries and A.J. Burggraaf, in: Proc. Vol. 89-11 (Electro& Soc. 1st. Int. Symp. Solid Oxide Fuel Cells, 1989) p. 129.
- [136] T. Inoue, K. Hoashi, K. Eguchi and H. Arai, J. Mat.Sci. 28 (1993) 1532.
- [137] M. C. Brant, T. Matencio, L. Dessemond and R. Z. Domingues, Chem. Mater. 13 (2001) 3954.
- [138] M.C. Brant, T. Matencio, L. Dessemond and R.Z. Domingues, Solid State Ionics 177 (2006) 915.
- [139] L. Dessemond, R. Muccillo, M. He'nault and M. Kleitz, Appl. Phys. A57 (1993) 57.
- [140] T. Kato, A. Momma, Y. Kaga, S. Nagata and Y. Kasuga, In Proc. Vol. 40 of the Fifth International Symposium on Solid Oxide Fuel Cells, Eds. U. Stimming, S. C. Singhal, H. Tagawa and W. Lehnert, (The Electrochemical Society: Pennington, NJ, 1997) p. 1150.
- [141] M. C. Brant and L. Dessemond, Solid State Ionics 1 (2000) 138.
- [142] A. M. Anthony, Acad. Sci. Paris 256 (1963) 5130.
- [143] A. D. Neuimin and S.F. Pal'guev, Chem. Abstr. 62 (1965)8472.

- [144] F.W. Poulsen, *Solid State Ionics* 40-41 (1990) 947.
- [145] T. Setoguchi, T. Inoue, H. Takebe, K. Eguchi, K. Morinaga and H. Arai, *Solid State Ionics* 37 (1990) 217.
- [146] C. Fouard, A.Malandain, S. Prohaska and M. Westerhoff, *IEEE Transactions on Medical Imaging*, 25 (2006) 1319.
- [147] C.L. Lin and J.D. Miller, *International Journal of Mineral Processing Solid Liquid Separation Systems*, 73 (2004) 281.
- [148] D. Silin and T. Petzek, *J. of Physica a-Statistical Mechanics and Its Applications* 371 (2006) 336.
- [149] M.B. Clennell, in: *Developments in Petrophysics*, Geological Society Special Publication Eds. M.A. Lovell, P.K. Harvey, 122 (1997) p. 299.
- [150] Y.L. Golin, V.E. Karyarin, B.S. Pospelov and V.I. Sevedkin, *Soviet Electrochemistry* 28 (1992) 87.
- [151] D. L. Johnson, J. Koplik and L. M. Schwartz, *Phys. Rev. Lett.* 57 (1986) 2564.
- [152] A. J. Katz and A. H. Thompson, *J. Geophys. Res. B* 92 (1987) 599.
- [153] D. J. Wilkinson, D. L. Johnson and L. M. Schwartz, *Phys. Rev. B* 44 (1991) 4960.
- [154] S. Kostek, L. M. Schwartz and D. L. Johnson, *Phys. Rev. B* 45 (1992) 186.
- [155] D. L. Johnson, D. L. Hemmick and H. Kojima, *J. Appl. Phys.* 76 (1994) 104.
- [156] K.H. Hellmuth, P. Klobes, K. Meyer, B. R. Kuhn, M. S. Kauppi, J. Hartikainen, K. Hartikainen and J. Timonen, *Z. Geol. Wiss.*, 23 (1995) 691.
- [157] J. Bear, *Dynamics of Fluids in Porous Media*, Dover, NewYork, 1972.
- [158] Y. A. Buyevich, *Int. J. Heat Mass Transf.* 35 (1992) 2445.
- [159] C.N. Satterfield and T.K. Sherwood, *The Role of Diffusion in Catalysis*. Addison-Wesley, Reading Mass, 1963.
- [160] P. Costamagna and K. Honegger, *J. Electrochem. Soc.* 145 (1998) 3995.
- [161] R.E. Williford, L.A. Chick, G.D. Maupin, S.P. Simner and J.W. Stevenson, *J. Electrochem. Soc.* 150 (2003) A1067.
- [162] L. Ma, *J. Fuel Cell Sci. Technol.* 2 (2005) 246.

- [163] M. F. L. Johnson and W. E. Stewart, *J. Catal.* 4 (1965) 248.
- [164] C. N. Satterfield and P. J. Cadle, *Ind. Eng. Chem. Fundam.* 7 (1968) 202.
- [165] L. A. Chick, J. W. Stevenson, K. D. Meinhardt, S. P. Simner, J. E. Jaffe and R. E. Williford, *Modeling and Performance of Anode Supported SOFC*, Fuel Cell Seminar Abstracts, Courtesy Associates, (2002) p. 619.
- [166] K.J. Witt and J. Brauns, *Journal of Geotechnical Engineering* 109 (1983) 1181.
- [167] K. Huang, *J. Electrochem. Soc.* 151 (2004) A716.
- [168] T. Lee, R.L. Kashyap and C. Chu, *Graphical Models and Image Processing*, 56 (1994) 462.
- [169] K. Palagyi and A. Kuba, *Pattern Recognition Lett.* 19 (1998) 613.
- [170] T. F. Kelly, T. T. Gribb, J. D. Olson, R. L. Martens, J. D. Shepard, S. A. Wiener, T. C. Kunicki, R. M. Ulfig, D. R. Lenz, E. M. Strennen, E. Oltman, J. H. Bunton and D. R. Strait, *Microsc. Microanal.* 10 (2004) 373.
- [171] J.R. Macdonald, *Impedance Spectroscopy*, John Wiley and Sons, New York, NY, 1987

BIOGRAPHICAL SKETCH

Aijie Chen was born to Meichun Song and Zhaoming Chen in Laiwu, Shandong, P.R. China. During her childhood, her father instilled in her a strong sense of integrity, self confidence and perseverance. In 1991 she attended the Northeastern University in Shenyang, Liaoning, P.R.China to earn her Bachelor of Engineering, where her focus of study was metal forming engineering. After she graduated in 1995, she joined Laiwu Steel & Iron Corp., the largest steel and iron company in Shandong province in P.R.China as a research engineer. In 2002, she moved onto graduate school at the Michigan Technological University, Houghton, Michigan, where her focus of study was materials science and engineering, conducting research of the effect of the ion implantation processing on optical waveguide device under Dr. Peter D. Moran. In October 2003, she welcomed birth of her son in Houghton, Michigan. After graduating with a Master of Engineering in material science, she proceeded to the University of Florida in Gainesville, Florida, where she has been working toward her doctoral degree in materials science and engineering since August 2004. Her PhD work commenced in the field of electronic materials under Prof. Kevin S. Jones in the areas of classical stereology, 2-D, and 3-D microstructure characterization for advanced solid oxide fuel cell. During her graduate study, she interned at Caterpillar Inc., where she worked in new product development, studying the diesel particulate filter of the heavy-duty diesel engine. Subsequently, she worked in advanced materials technology, analyzing the microstructure evolution of the gas turbine after heat-treatment. Upon receipt of the Doctor of Philosophy in 2008, she will join Caterpillar Inc. in Peoria, Illinois.